I

# Preparation of Ultra-thin $CuIn_{1-x}Ga_xSe_2$ Solar Cells and Their Light Absorption Enhancement

vorgelegt von
**Guanchao Yin**
**aus Hubei, China**

von der Fakultät III - Prozesswissenschaften
der Technischen Universität Berlin
zur Erlangung des akademischen Grades

Doktor der Ingenieurwissenschaften
-Dr.rer.nat.

genehmigte Dissertation

angefertigt am Helmholtz-Zentrum Berlin für Materialien und Energie, Nanooptical Concepts for PV

Promotionsausschuss:
Vorsitzender: Prof. Dr. John Banhart
Berichter: Prof. Dr. Walter Reimers
Berichter: Prof. Dr. Martina Schmid
Tag der wissenschaftlichen Aussprache: 23.03.2015
Berlin, 2015

# Contents

# Abbreviations and symbols

| | |
|---|---|
| $\alpha$ | polarisability |
| $\eta$ | conversion efficiency |
| $\lambda$ | wavelength |
| $\Phi$ | incident photon flux |
| $K$ | Boltzmann constant |
| $\theta$ | phase shift of light propagating |
| $\sigma$ | interface roughness |
| $\varepsilon$ | dielectric function |
| | |
| A | diode quality factor |
| *Abs* | absorption |
| AFM | atomic force microscopy |
| ALD | atom layer deposition |
| AM 1.5 | reference solar spectral irradiance under air mass 1.5 |
| AZO | Al doped ZnO (Al: ZnO) |
| $C_{abs}$ | absorption cross section |
| $C_{sca}$ | scattering cross section |
| $C_{ext}$ | extinction cross section |
| CB | conduction band |
| CBD | Chemical Bath Method |
| Cu | copper |
| CIGSe | $CuIn_{1-x}Ga_xSe_2$ |
| CISe | $CuInSe_2$ |
| CGSe | $CuGaSe_2$ |
| *d* | diameter |
| DC | direct current |
| E | electric field |
| $E_{g,min}$ | minimum bandgap |
| *EQE* | external quantum efficiency |
| FDTD | finite difference time domain |
| *FF* | fill factor |
| Ga | gallium |
| GDOES | glow charge optical emission spectrometry |
| In | indium |
| *IQE* | internal quantum efficiency |
| ITO | Sn doped $In_2O_3$ |
| $J_{sc}$ | short circuit current density |
| $J_m$ | current density corresponding to the maximum power |

| | |
|---|---|
| *J-V* | current density-voltage |
| LB | langmuir-blodgett |
| LLS | laser light scattering |
| MTM | modified transfer-matrix |
| N | complex refractive index |
| *n* | refractive index |
| $P_m$ | maximum power |
| $P_{in}$ | incident power |
| RMS | root mean square |
| PML | perfectly matching layer |
| q | elementary electric charge |
| *r* | reflection Fresnel coefficient |
| *R* | reflection |
| SCIL | substrate conformal imprint lithography |
| SCR | space charge region |
| SEM | scanning electron microscopy |
| Se | Selenium |
| T | transmission |
| t | transmission Fresnel coefficient |
| $T_s$ | substrate temperature |
| TCO | transparent conductive oxide |
| TM | transfer-matrix |
| UV-Vis | ultraviolet–visible spectroscopy |
| V | voltage |
| $V_{oc}$ | open-circuit voltage |
| $V_m$ | voltage corresponding to the maximum power |
| VB | valence band |
| XPS | X-ray photoelectron spectroscopy |
| XRD | X-Ray diffraction |
| XRF | X-Ray fluorescence |

# Abstract

$CuIn_{1-x}Ga_xSe_2$ (CIGSe) solar cells are the promising thin-film candidates to compete with the dominant crystalline Si solar cells in the photovoltaic market. One of the major concerns in mass production is the consumption of the rare element Indium and the resultant high manufacturing cost. To achieve the goal of reduced consumption of Indium, one approach is to reduce the thickness of CIGSe absorbers from typical 2-3 μm to below 500 nm. However, the ultra-thin (CIGSe thickness less than 500 nm thick) CIGSe solar cells have failed to maintain their high performance compared to their thick counterparts. Back recombination and incomplete absorption are assumed to be the main reasons for this reduced performance. Therefore, the work in this thesis centers on improving the performance of the ultra-thin CIGSe solar cells by restraining back recombination and improving light absorption.

A reduction in back recombination is achieved using a high back Ga/[Ga+In] ([Ga]/[III]) grading. To create a high back [Ga]/[III] grading, a low substrate temperature (440 °C) is employed for the CIGSe absorber deposition instead of the typical high temperatures above 500 °C. It is discovered that the low substrate temperature 440 °C can reduce the inter-diffusion of Ga-In and thus create a higher back [Ga]/[III] grading compared to the high substrate temperature of 610 °C. This higher back [Ga]/[III] grading is evidenced to both electrically and optically contribute to the efficiency enhancement (an increase of 17.8%) in contrast to the lower back [Ga]/[III] grading at 610 °C for the solar cells with a 460-nm-thick CIGSe layer.

To overcome the incomplete absorption arising from the CIGSe thickness reduction, the implementation of light-trapping structures is indispensable. The effectiveness of these structures is simulated prior to the implementation in order to reduce the experiment effort. Towards this, optical constants of the layers in the solar cells are firstly required. For obtaining accurate optical constants ($n$, $k$) or complex refractive index $n+ik$, Transfer-Matrix (TM) method is applied to calculate the optical constants of the individual layer with a focus on CIGSe layers since they determine the optoelectronic properties of solar cells to a great extent. The influence of surface roughness and substrate temperature are particularly investigated. In this work, the TM method is modified to include scalar scattering theory for considering the scattering arising from

surface roughness. It is shown that the modified Transfer-Matrix method improves the accuracy of *n* values in the short wavelength range. Regarding the effect of substrate temperature on the optical constants, it is shown that the temperature has little influence in CGSe. For CIGSe ($x = 0.4$), the refractive index *n* for the sample at low temperature (440 °C) stayed relatively unchanged, although the grain size was reduced and the [Ga]/[III] profile was altered compared to that at high temperature (610 °C). In contrast, the extinction coefficient (*k*) values at 440 °C show higher absorption at long wavelengths due to a lower minimum bandgap ($E_{g,min}$) originating from the reduced inter-diffusion of Ga-In. Finally, using TM method, a database of optical constants of CIGSe and other layers in the solar cells in the experiments is established and ready for the optical simulations.

To enhance the absorption of ultra-thin CIGSe solar cells, metallic Ag nanoparticles under Sn:$In_2O_3$ (ITO) back contact, closely-packed $SiO_2$ sphere arrays on the surface and $SiO_2$ nanostructures at the interface of Mo/CIGSe, are investigated as the light-trapping structures. It is found that the ITO layer failed to block the diffusion of Ag during CIGSe deposition even at the low substrate temperature (440 °C). A 50-nm-thick Atomic layer deposited (ALD) prepared $Al_2O_3$ film is used to passivate the thermal diffusion of Ag nanoparticles. Theoretical optical simulations prove the concept that the Ag nanoparticles are able to greatly enhance the effective absorption in the solar cells. Regarding the closely-packed $SiO_2$ sphere arrays on the surface, it is theoretically demonstrated that large spheres dominate the light absorption in terms of whispering gallery modes and small spheres by forming an effective anti-reflection layer. Due to the anti-reflection effect being more broadband than whispering gallery modes, the maximum absorption enhancement is achieved for the small sphere at a diameter size of 110 nm. Experimentally, the solar cells with a 460-nm-thick absorber gain a photocurrent density enhancement of 2.17 mA/cm$^2$ after coating a 120-nm-diameter $SiO_2$ sphere array, which agrees quite well with the theoretical simulations. $SiO_2$ nanostructures (205 nm in radius, 210 nm in height and 513 nm in pitch) at the interface of CIGSe/Mo are able to scatter the unabsorbed light back into the CIGSe layer via Mie resonances. Simulations confirm that this leads to a significant absorption improvement in the CIGSe layer by reducing the parasitic absorption in Mo, which is considered to be the main parasitic absorption source in ultra-thin CIGSe solar cells. Experiments are in accordance with the simulations, the efficiency increase from 11.0% to 12.4% is mainly

due to the photocurrent enhancement from 28.6 mA/cm$^2$ to 30.6 mA/cm$^2$ after incorporating $SiO_2$ nanostructures for the solar cells with a CIGSe thickness of 470 nm. Further with the 120-nm-diameter $SiO_2$ sphere array on the surface, *R* is restraint and the photocurrent density is further improved to 31.6 mA/cm$^2$ and efficiency to 13.1%. This is the first time that the photocurrent current density is reported to exceed 30 mA/cm$^2$ for ultra-thin CIGSe solar cells.

# Kurzfassung

$CuIn_{1-x}Ga_xSe_2$ (CIGSe)-Solarzellen stammen aus dem Bereich der Dünnschichttechnologie und sind eine vielversprechende Alternative zu den herkömmlichen kristallinen Si Solarzellen. Einer der größten Bedenken bezüglich der Massenproduktion von CIGSe-Solarzellen ist die Verwendung des seltenen Elements Indium und der daraus resultierenden hohen Herstellungskosten. Um diese Kosten zu senken verfolgt man den Ansatz, die Dicke der CIGSe-Absorber von 2-3 um auf unter 500 nm zu reduzieren, jedoch haben diese ultra dünnen CIGSe-Solarzellen eine viel geringere Effizienz. Es wird angenommen, dass Rekombination und unvollständige Absorption die geringere Effizienz zu verantworten haben. Daher, konzentriert sich diese Arbeit im Wesentlichen darauf diese zwei Effekte zu minimieren.

Eine Reduktion der Rekombination wird durch einen höheren Ga/[Ga+In] ([Ga]/[III]) Gradient an der Rückseite der Solarzelle erreicht. Um diesen [Ga]/[III]-Gradienten herzustellen, wird eine niedrige Substrattemperatur (440°C) anstatt einer sonst höheren Temperatur (über 500°C) für die CIGSe-Absorber Abscheidung verwendet. Es wurde herausgefunden, dass eine niedrigere Substrattemperatur die Interdiffusion von Ga-In reduziert und dies erzeugt ein höheren [Ga]/[III]-Gradienten verglichen mit einer hohen Substrattemperatur (610 °C). Außerdem wurde bewiesen, dass dieser hohe [Ga]/[III]-Gradient bei einen 460 nm dicken CIGSe Absorber sowohl elektrisch als auch optisch zu einer Verbesserung der Effizienz (um 17.8%) beiträgt verglichen mit einem geringeren [Ga]/[III]-Gradienten bei 610°C.

Um die unvollständige Absorption, die durch die reduzierte CIGSe-Schichtdicke entsteht, zu überwinden, wird der Einbau von Strukturen, die das Licht einfangen, unentbehrlich. Die Effektivität dieser Strukturen wurde vor dem Einbau simuliert, um den experimentellen Aufwand zu reduzieren. Hierzu werden zunächst die optischen Konstanten von jeder Schicht benötigt. Um genaue optische Konstanten (*n, k*) oder den komplexen Brechungsindex $n+ik$ zu erhalten, wurde die Transfer-Matrix Methode benutzt. Die Transfer-Matrix Methode berechnet die optischen Konstanten von jeder einzelnen Schicht mit einem Fokus auf CIGSe-Schichten, da diese weitgehend die optoelektronischen Eigenschaften der Solarzelle bestimmen. Insbesondere der Einfluss der Oberflächenrauheit und der Substrattemperatur wurden untersucht. In dieser Arbeit

wird die TM-Methode modifiziert, um die skalare Streutheorie, welche die Streuung der Oberflächenrauhigkeit berücksichtigt, miteinzubeziehen. Es wird gezeigt, dass diese modifizierte Transfer-Matrix Methode die Genauigkeit der berechneten *n* Werte im Bereich kurzer Wellenlängen verbessert. Bezüglich der Wirkung der Substrattemperatur auf die optischen Konstanten, wird gezeigt, dass die Temperatur nur einen geringen Einfluss auf CGSe hat. Für CIGSe ($x = 0.4$) bleibt der Brechungsindex *n* für die Probe bei geringer Temperatur (440°C) relative unverändert, obwohl die Korngröße verringert wird, während das [Ga]/[III] Profil im Vergleich zu dem Profil bei hohen Temperaturen (610°C) verändert wurde. Im Gegensatz dazu zeigt der Extinktionskoeffizient bei 440°C eine höhere Absorption bei langen Wellenlängen wegen einer geringeren Bandlücke $E_{g,min}$ , die aufgrund der reduzierten Interdiffusion von Ga-In entsteht. Unter Benutzung der Transfer-Matrix Methode wurde eine Datenbank mit optischen Konstanten von CIGSe und anderen Schichten in der Solarzelle, die in den Versuchen benutzt wurden, eingerichtet. Diese ist wird für optische Simulationen verwendet.

Um die Absorption der ultradünnen CIGSe-Solarzellen zu verbessern, werden Ag-Nanopartikel unter einem Sn:$In_2O_3$ (ITO) Rückkontakt, dichtgepackte $SiO_2$-Kugel-Arrays auf der Oberfläche und $SiO_2$-Nanostrukturen an der Schnittstelle Mo/CIGSe verwendet. Bei der Untersuchung des Licht-Einfangs der Strukturen wurde herausgefunden, dass die ITO–Schicht die Diffusion der Ag-Partikel während der CIGSe-Abscheidung auch bei geringen Temperaturen (440 °C) nicht verhindert. Eine 50 nm dicke $Al_2O_3$ Schicht, die mit Atomlagenabscheidung (engl. atomic layer deposition (ALD)) hergestellt wurde, wurde verwendet, um die thermische Diffusion von Ag-Nanopartikeln zu verhindern. Theoretische optische Simulationen beweisen das Konzept, dass die Ag-Nanopartikel dazu in der Lage sind die effektive Absorption in der Solarzelle zu verbessern. Hinsichtlich der dichtgepackten $SiO_2$-Arrays auf der Oberfläche, hat sich gezeigt, dass große Kugeln die Lichtabsorption bezüglich der Flüstermodi (engl. wispering gallery modes) dominieren und kleine Kugeln eine Antireflektionsschicht bilden. Da die Antireflektionswirkung breitbandiger als die Flüstermodi sind, wird die maximale Absorptionsverstärkung für kleine Kugeln bei einem Durchmesser von 110 nm erreicht. Experimentell ließ sich nachweisen, dass in einer Solarzelle mit einem 460 nm dicken Absorber die Photostromdichte um 2.17 mA/cm² steigt, bei Beschichtung mit 120 nm Durchmesser $SiO_2$-kugeln. Dies stimmt sehr gut mit optischen Simulationen überein. $SiO_2$-Nanostrukturen (205 nm Radius, 210

nm Höhe und 513 nm Abstand) an der Grenzfläche CIGSe/Mo sind in der Lage das nicht absorbierte Licht über Mie Resonanzen zurück in die CIGSe Schicht zu streuen. Simulationen bestätigen, dass dies zu einer signifikanten Verbesserung der Absorption in der CIGSe-Schicht führt. Die parasitäre Absorption der Mo-Schicht, die Hauptquelle für parasitäre Absorption in ultradünnen CIGSe Absorbern, wird erheblich reduziert. Experimentell konnt in Übereinstimmung mit den Simulationen die Effizienz von 11% auf 12.4% erhöht werden. Dies ist hauptsächlich auf die Photostromverbesserung von 28.6 mA/cm² auf 30.6 mA/cm² nach dem Einbringen der $SiO_2$-Nanostrukturen in die 470 nm dicke CIGSe-Schicht zurück zu führen. Durch das weitere Aufbringen von $SiO_2$-Kugeln auf der Oberfläche wird die Reflexion R Verringert und die Photostromdichte wird weiter auf 31.6 mA/cm² und die Effizienz auf 13.1% verbessert. Somit wird zum ersten Mal berichtet, dass die Photostromdichte 30 mA/cm² für ultradünne CIGSe Solarzellen überschritten wurde.

# Chapter 1

# Introduction

In the past few years, significant progress has been achieved for $CuIn_{1-x}Ga_xSe_2$ (CIGSe) solar cells. The gain of 20.3 % [1] in efficiency was reached at low substrate temperature and 21.7 % [2] at high substrate temperature, which breaks the previous record of 20.4% [3] of multi-crystalline solar cells. These achievements further demonstrate the potential of high efficiencies for CIGSe solar cells and will greatly push the development towards mass production. One of the main concerning factors from the initial development period of CIGSe solar cells is the high material cost associated with the CIGSe compound [4]. The CIGSe, being the absorber, plays a key role in solar cells. It is the compound of copper (Cu), indium (In), gallium (Ga), selenium (Se). Among these four elements, In is a strategic resource due to its rarity in earth and the price is constantly high on the market [4-6]. Additionally, the production capacity of Ga is restrained owing to milling difficulty [6].

One direction for reducing the material consumption and the resulting material cost is to lower the thickness of CIGSe absorbers [7-9]. The typical thickness of CIGSe layers is around 2-3 μm [8]. The ultra-thin CIGSe solar cells (absorber thickness less than 0.5 μm) however fail to maintain the high efficiencies, the dominant reason behind this poor performance is the substantial drop of short circuit current density ($J_{sc}$) [8, 9, 10]. Fig.1.1 plots the external quantum efficiencies (EQE) of solar cells with a 2 μm and a 460 nm thick CIGS layer. Compared to the 2-μm-thick-absorber solar cell, the main loss for the 460-nm-thick-absorber solar cell lies in the wavelength range from 600 nm to the infrared. This loss is caused by two main factors: back recombination and incomplete absorption [7, 9-11].

For CIGSe solar cells, the minority carriers (electrons) can diffuse towards the rear interface of CIGSe/back contact and recombine with holes due to the high interface defect density. This is referred as back recombination [9-11]. The recombination is especially stronger for ultra-thin solar cells because the CIGSe/back contact interface is within the diffusion length of electrons [10]. It can not only reduce $J_{sc}$, but also

deteriorate open-circuit voltage ($V_{oc}$) and fill factor ($FF$). In this work, the first aim is thus the reduction of back recombination for producing the highly efficient ultra-thin CIGSe solar cells in my work. Otherwise, even the absorption is improved, the generated carriers will recombine at CIGSe/back contact and don't effectively contribute to the current.

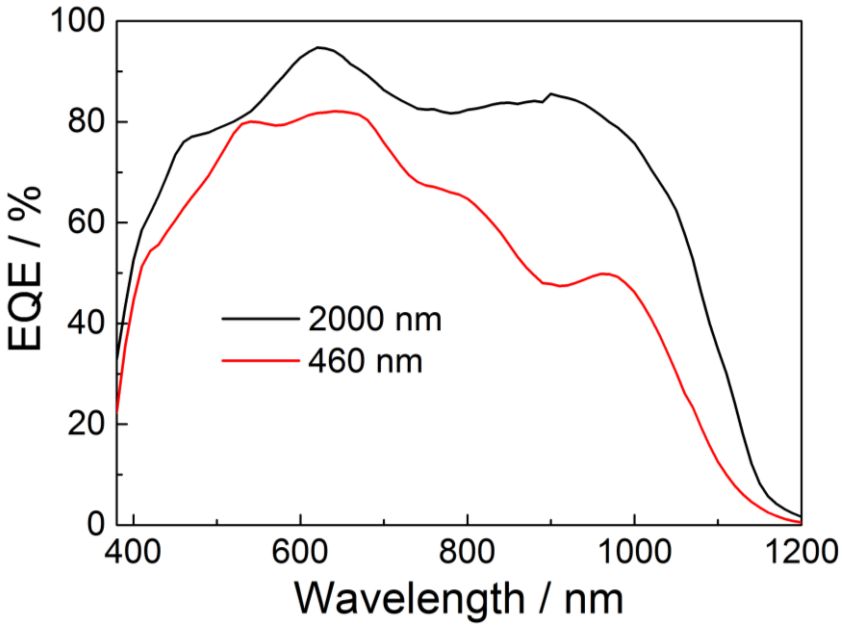


Fig.1.1 Comparison of EQE curves of solar cells with a 2000-nm-thick and a 460-nm-thick absorber

The second factor which is limiting the performance of ultra-thin CIGSe solar cells is the incomplete light absorption. To overcome this, the implementation of light-trapping structures is required. However, due to the complexity of light propagation through the solar cell with light-trapping structures, theoretical optical simulations are necessarily needed to predict the optical responses of the whole solar cell and thus provide the guidance on how to select effective light-trapping technologies and the optimum structure geometry. The simulations require optical constants or complex refractive index (refractive index $n$, extinction coefficient $k$) of each material as the basic input parameters. However, the optical constants of each material are experiment-dependent, which gives rise to the poor applicability of the available data in literature for the practical simulations of solar cells in this work. Thus, the work on light absorption improvement in this thesis is divided into 2 distinct sections:

1: Determination of the practical and accurate optical constants for each layer in the experimental CIGSe solar cells

2: Investigation of the integration of light-trapping structures into the ultra-thin solar cells both experimentally and theoretically

In contrast to conventional light-trapping structures, for instance interface texturing [12, 13] and back reflecting [13-15], numerous innovative light-trapping approaches [16-23] have shown the potential to better improve the light absorption in Si-based, GaAs and organic solar cells. These schemes include plasmonic nanostrcutures of metallic nanoparticles [16-19], photonic crystals [20, 21] and diffractive structures [23] of dielectric particles. However, only a few have been reported on CIGSe solar cells and were limited to theoretical investigations [24, 25]. Compared to Si-based, GaAs and organic solar cells, CIGSe cells differ a lot from the basic material properties to the solar cell structures. The question then arises: are those light-tapping approaches working well on Si-based and GaAs solar cells suitable as well for CIGSe solar cells? The first concerning point is the stable integration of light-trapping structures into solar cells. This requires that the incorporation does not deteriorate the electrical properties of bare solar cells and the materials of light-trapping structures can also survive the solar cell preparation. Further, optimizations of the light-trapping structures, covering the selection of materials, structure geometries and integration locations in the solar cells, is not investigated systematically. Therefore, in this thesis, the investigations will include the incorporation of innovative light-trapping schemes into the ultra-thin CIGSe solar cells. I will confine my investigations to the plasmonic Ag nanoparticles underneath the transparent back contact, the close-packed $SiO_2$ nanosphere arrays on the top of cells and the dielectric $SiO_2$ nanostructures at the rear interface of CIGSe/back contact.

According to the description mentioned above, the whole thesis is structured as follows:

Chapter 2 starts with the basic introduction of the working principles of p-n junction based solar cells. Subsequently, CIGSe solar cells will be overviewed, covering the preparation, physical properties of each layer in the whole cell device. The characterization methods related to the structures, compositions, optical and electrical properties of layers and/or devices will be briefly mentioned as well. Finally, I will describe the preparation of the ultra-thin CIGSe solar cells at low substrate temperature, intending to create a higher Ga/[III] grading towards the back contact and to reduce the

back recombination. The solar cells prepared at low substrate temperature will be analyzed compared to those at high substrate temperature.

Chapter 3 is related to the determination of the optical constants of each layer in the cell device from the experimental samples, with a special focus on CIGSe layers. The working principles of Transfer-Matrix method proposed for the experimental extraction of the optical constants is described in great detail. An example of how to extract the optical constants will be illustrated. To obtain more accurate optical constants of the CIGSe layers, surface roughness, substrate temperature will be taken into account. In the end, a database of optical constants of each layer will be established for the optical simulations.

Chapter 4 takes the Transfer-Matrix method inversely and calculates the optical responses of the ultra-thin CIGSe solar cells. By comparing to the optical responses of thick solar cells, the optical loss of ultra-thin solar cells will be identified. Furthermore, anti-reflection and large-angular scattering effects from the top of ultra-thin cells are evaluated theoretically. Accordingly, implications for light-trapping schemes will be given.

Chapter 5 goes into the field of light trapping using plasmonic Ag nanoparticles underneath transparent back contact. The thermal stability of Ag nanoparticles under CIGSe deposition will be first identified. The optical properties and electrical performances of solar cells after incorporating Ag nanoparticles will be then evaluated.

Chapter 6 investigates the closely packed $SiO_2$ nanosphere arrays on the surface of solar cells both theoretically and experimentally. 3-D theoretical simulations will be initially performed dependent on sphere diameters and the light-trapping mechanisms will be analyzed. Further, experimental verifications will be implemented and compared to the theoretical simulations.

Chapter 7 investigates the light-trapping effect of $SiO_2$ nanostructures at the interface of CIGSe/Mo. The optical influences of the $SiO_2$ nanoparticles will be also evaluated both theoretically and experimentally.

Chapter 8 will conclude the whole work in this thesis.

# Chapter 2

# Ultra-thin $CuIn_{1-x}Ga_xSe_2$ solar cells at low substrate temperature

This chapter starts with the introduction of the basic working principles of solar cells based on p-n junction; the $CuIn_{1-x}Ga_xSe_2$ (CIGSe) solar cell structure and how to prepare each layer are then elaborated; subsequently, the characterizations in the whole thesis are listed centrally; finally, the solar cells prepared at low temperature are investigated in detail.

## 2.1 Solar cells based on p-n junction [26, 27]

The core part of solar cells based on p-n junction is essentially composed of a p-type and a n-typed semiconductor layer, which form a junction and a resulting internal electric field within the junction. Under illumination, the photo-generated carriers are driven and separated by the internal electric field: electrons go toward the n-typed layer and holes toward the p-typed. When the external circuit is linked with a load, the separated carriers form current and the light is thus transformed to the energy in the form of electricity. Fig.2.1 gives the schematic illustration of a p-n junction.

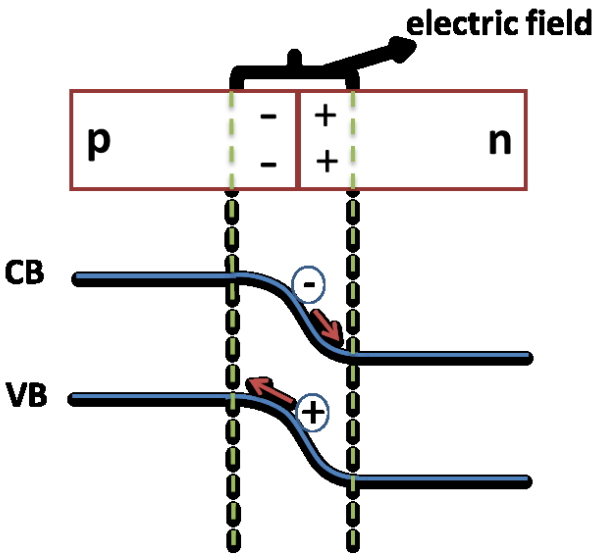


Fig.2.1 Schematic of a p-n junction

For a p-n junction under illumination, the external net-current density can be expressed as:

$$J(v) = J_0 \left[\exp\left(\frac{qv}{AKT}\right) - 1\right] - J_{ph} \quad 2\text{-}1$$

Where, $J_0$ is the saturation-current density, $J_{ph}$ photon generated current density, $k$ the Boltzmann constant, $T$ the temperature, $V$ here the voltage drop on the external load, $q$ the elementary electric charge, $A$ the diode quality factor of the p-n junction.

***Current density-voltage (J-V)***

J-V measurement is the most important characterization to describe the performance of solar cells under illumination. There are three main parameters in the J-V curve. They are short-circuit current density, $J_{sc}$; open-circuit voltage, $V_{oc}$; fill factor, $FF$. These parameters are derived from the illuminated J-V curve. The conversion efficiency, $\eta$, is determined from these parameters.

Short-circuit current density ($J_{sc}$)

The short-circuit current density, $J_{sc}$, is the current density that flows through an external circuit when the solar cell is short circuited. $J_{sc}$ depends on the absorption of solar cells and collection efficiency of carriers. In this case, $J_{sc}$ is equal to $J_{ph}$.

Open-circuit voltage ($V_{oc}$)

The open-circuit voltage, $V_{oc}$, corresponds to the voltage where the external circuit is opened and the net current density $J(v)$ is zero. Therefore, it is derived from Eq. (2-1):

$$V_{oc} = \frac{AKT}{q}\ln\left(\frac{J_{ph}}{J_0} + 1\right) \quad 2\text{-}2$$

The equation signifies that $V_{oc}$ depends on $J_{ph}$ and $J_0$. While, $J_{ph}$ typically has a slight variation, the key effect is the saturation current density $J_0$, which can vary by several orders of magnitude.

Fill factor ($FF$)

The fill factor is defined as:

$$FF = \frac{J_m * V_m}{V_{oc} * J_{sc}} \quad 2\text{-}3$$

Where $J_m$ , $V_m$ are the corresponding current density and voltage when the maximum power $P_m$ is reached.

Conversion efficiency ($\eta$)

The conversion efficiency is the ratio of the output maximum power to the incident power. For the incident power, $P_{in}$ (=1000 W/m$^2$), is a standard in the name of AM 1.5 for measuring the conversion efficiency of solar cells.

$$\eta = \frac{P_m}{P_{in}} = \frac{J_m V_m}{P_{in}} = \frac{J_{sc} V_{oc} FF}{P_{in}} \quad 2\text{-}4$$

***Quantum efficiency (QE)***

Quantum efficiency characterizes the electrical response to the incident light. There are two types of quantum efficiencies for solar cells:

- External Quantum Efficiency (*EQE*)

$$EQE(\lambda) = \frac{\text{the number of collected charge carriers by the solar cell}}{\text{the number of incident photons}} \quad 2\text{-}5$$

The unity 1 means all the incident photons are absorbed and the corresponding photo-generated carriers are completely collected.

- Internal Quantum Efficiency (*IQE*)

$$IQE(\lambda) = \frac{\text{the number of collected charge carriers by the solar cell}}{\text{the number of absorbed photons}} \quad 2\text{-}6$$

For this case, *R* and *T* of solar cells are excluded, so *IQE* value is always larger than *EQE* value.

$$IQE(\lambda) = \frac{EQE(\lambda)}{(1-R-T)} \quad 2\text{-}7$$

It should be noted that $J_{sc}$ can be integrated from *EQE* values:

$$J_{sc} = \int_{\lambda 1}^{\lambda 2} qEQE(\lambda)\Phi(\lambda)d\lambda \quad 2\text{-}8$$

Where λ is the wavelength, $\Phi(\lambda)$ the incident photon flux

## 2.2 CIGSe thin film solar cells

Fig.2.2 shows a typical structure of CIGSe solar cell devices, which is also used in my work. It is composed of front contact/AZO(Al:ZnO)/ZnO/CdS/CIGSe/back contact/glass substrate from top to bottom. The basic information and preparation

details of each layer in my work will be elaborated subsequently following the fabrication sequence.

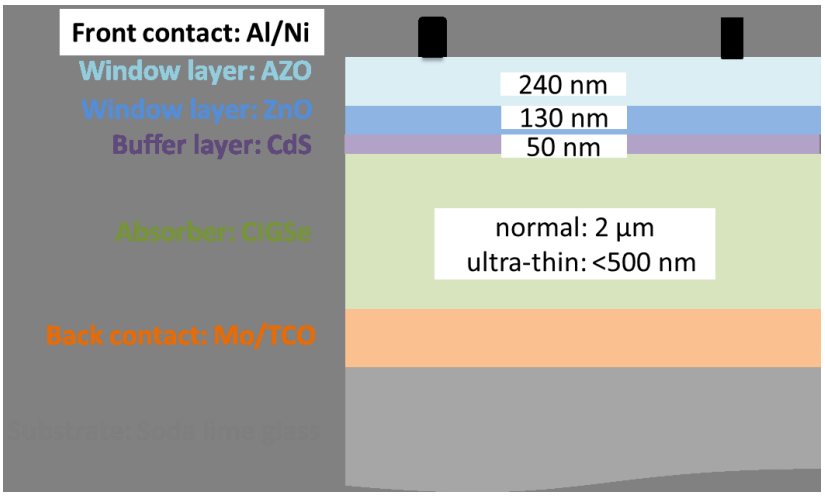


Fig.2.2 The layer structure of typical CIGSe solar cell devices (The thickness values match the practical samples in this work if no further specifications)

***Glass substrate and back contact***

The glass substrate serves as a supporting material and is mostly soda-lime glass. It provides Na source, which can diffuse through back contact to the CIGSe absorber during deposition [28]. The Mo material is the most commonly used back contact. Mo, being the back contact, fulfills several other specifications except good conductivity [29]: 1) thermally (bearing the growth temperature of CIGSe) as well as chemically stable (inert to the Se atmosphere during CIGSe deposition); 2) formation of ohmic back contact with CIGSe to favour the collection of photo-generated holes. Apart from Mo, transparent conductive oxide (TCO) layers are also used for alternative back contact [30]. The Sn doped $In_2O_3$ (ITO) layer is also employed as transparent back contact in my work.

*Preparation*: The Mo back contact used here is commercially purchased from company, which is prepared by magnetron sputtering with a thickness of 800 nm. It has a sheet resistance of 8 Ω/□. The ITO layers are fabricated in a base pressure of $10^{-5}$ Pa at room temperature by magnetron sputtering. The $In_2O_3/SnO_2$ compositions of the targets are 90:10 wt%, respectively. The deposition rate is around1.1 nm/s and the final thickness is approx. 200 nm.

***CIGSe layer***

CIGSe is the p-typed absorber. It has a chalcopyrite structure and its absorption coefficient can reach $10^5$ $cm^{-1}$. The bandgap ranges 1.0-1.67 eV depending on Ga/[III] [31]. For the typical solar cells, Ga/[III] ratio is usually around 0.3 for high solar cell performance, which corresponds to a bandgap of 1.2 eV. Besides, Cu/[III] ratio is slightly lower (0.8-0.9) with respect to stoichiometry, which is favourable for the formation of p-n junction with the CdS layer. Na doping plays a key role in improving the effective doping of CIGSe and the performance of solar cells [28]. This is why Na-containing soda-lime glass substrates are most used or extra Na is added.

The typical thickness of a CIGSe layer is around 2-3 µm, which can absorb most of the incident light. When the absorber thickness is below 500nm, this will inevitably lead to incomplete absorption of light.

The deposition methods of CIGSe layers can be in principle classified to sequential deposition [32, 33] and co-evaporation process [34]. What applied in this work is the so called 3-stage co-evaporation process [34]. This method has been widely applied in the lab and offers big crystalline grains and favorable electric properties of solar cells.

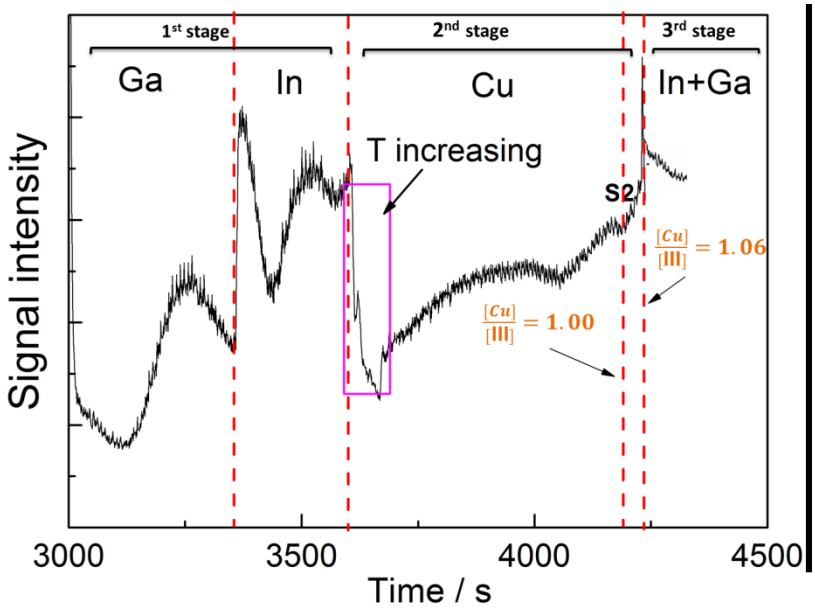


Fig.2.3 An exemplary Laser light scattering (LLS) pattern of a 3-stage process at $T_S$ =440 °C

*Preparation:* The 3-stage co-evaporation starts with the deposition of Ga-Se and In-Se precursors at a lower temperature (1st stage), then Cu-Se and In-Ga-Se precursors are evaporated at the substrate temperature $T_S$ during the 2nd and 3rd stage, respectively. $T_S$

is higher than that in the 1st stage and is defined as substrate temperature. After reaching [Cu]/[III] of 1.0-1.15 at the end of the 2nd stage, the process transitions to the 3rd stage and terminates at a [Cu]/[III] ratio of around 0.8-0.9. Laser light scattering [35] (LLS) is used for the in-situ control of the process. The composition ratios mentioned above are the estimated values from LLS signal.

For all the absorbers in this work, the substrate temperature is 410 °C in the 1st stage and ramps to $T_S$ in the beginning of the 2nd stage. [Cu]/[III] is 1.06 and 0.86 at the end of the 2nd and 3rd stage, respectively. By varying the deposition time of Ga-Se and In-Se, the overall [Ga]/[III] ratio can be adjusted. Fig.2.3 shows a LLS pattern of a 3-stage process at $T_S$ = 440 °C, corresponding to a 460-nm-thick CIGSe layer with [Cu]/[III] of 0.4.

***CdS buffer layer***

CdS is the n-typed material with a bandgap of 2.4 eV, which forms the p-n junction with CIGSe. Because CdS can minimize the interface recombination between CIGSe and ZnO/AZO, this layer is normally referred as buffer layer. Though several non-toxic alternative materials [36] like Zn(O,S), $In_2S_3$ are tested, CdS gains the dominant application due to the favorable electrical properties of CIGSe/CdS junction. The CdS layer normally has a thickness of 50 nm and is prepared by Chemical Bath Method (CBD).

*Preparation:* The CBD process is performed in a solution with 1.1 M ammonia, 0.14 M Thiourea and 0.002 M Cadmium Acetate at 60 °C for 10 minutes.

***Window layers (ZnO/AZO)***

ZnO/AZO are both heavily n doped ($n^+$) and can form $n^+/n$ junction with CdS, which can further help the collection of carriers. They have a bandgap of 3.2/3.6 eV, which enables the penetration of most incident light to the CIGSe absorber. The AZO layer is highly conductive and serves as the front electrode. ZnO is generally believed to be able to prevent the shunting probability of solar cells [29].

*Preparation:* The ZnO layer is deposited by RF magnetron sputtering at a substrate temperature of 150 °C at a vacuum of $8.0*10^{-3}$ Pa. The final thickness is 130 nm with a sheet resistance of 30 Ω/□. The AZO layer is deposited by DC magnetron sputtering in

the same chamber also at a substrate temperature of 150 °C. The thickness is 240 nm with a sheet resistance of 5 Ω/□. The $Al_2O_3$/ZnO ratio of the target is 2:98 in wt%.

***Front contact (Ni/Al)***

The front contact grid is made of Ni/Al and deposited for the better collection of carriers. *Ni* works as a barrier layer for blocking the diffusion of Al into the AZO layer.

*Preparation:* The Ni/Al front contact grid is e-beam evaporated through a shadow mask. Ni deposition is prior to Al. It has a thicknesses of 10/1500 nm.

***Solar cell preparation***

The solar cell completion is done as described above sequentially from glass to front contact grid, Mo or ITO back contact are used. After the front contact deposition, 0.5 $cm^2$ solar cells were mechanically scribed including the area of the front contact grid.

Two points should be cleared here: 1) Amongst all the layers in the solar cell, the CIGSe layer is grown at the highest substrate temperature. When I mention preparation temperature of solar cells, it means the substrate temperature ($T_s$) of CIGSe growth; 2)Across the whole thesis, the method of preparing each layer is the same as described above if no specific notification.

## 2.3 Characterization methods in CIGSe solar cells

The characterization methods in the whole work can be sub-divided into structural, optical and electrical characterization.

Structural characterizations mainly cover the phase, morphology, element composition, element depth distribution and diffusion measurements. For identifying the influence of substrate temperature on CIGSe phases, X-Ray Diffraction (XRD) was applied to characterize the preferential (112) diffraction of CIGSe in chapter 2. Scanning Electron Microscopy (SEM) measurement was carried out for the surfaces, cross sections of thin layers in solar cells and light-trapping structures in the whole thesis. The thicknesses of thin layers could be evaluated from the cross sections. Compared to SEM, Atomic Force Microscopy (AFM) can present the surface morphology as well. Additionally, the real height of surface irregularities can be evaluated. This was used to determine the surface roughness, which was required for the accurate extraction of optical constants in chapter 3. The properties of CIGSe layers are very sensitive to the overall element compositions

and element depth distribution. X-Ray Fluorescence (XRF) was applied for the determination of overall element compositions. For further determination of the depth distribution of elements in CIGSe absorbers, Glow Discharge Optical Emission Spectrometry (GDOES) [37] was employed. To investigate the thermal stability of Ag nanoparticles during CIGSe deposition, X-ray photoelectron spectroscopy (XPS) measurement was used in chapter 5.

Optical Characterization only specifies the reflection/transmission (*R/T*) measurement under normal incidence in this work. It was mainly used in chapter 3 for the extraction of optical constants, which needs *R/T* as the input parameters.

For electrical characterization (*J-V, EQE*), current density- voltage *(J-V)* was for the overall performance evaluation of solar cells. The external quantum efficiency (*EQE*) was to characterize the electrical response of solar cells to incident light with spectral resolution. This is especially useful to identify in which wavelength range and how much light-trapping structures affect.

The basic instrument information and measurement conditions of all characterization methods are summarized:

***Structure characterization:***

SEM: In my work, the morphologies are mainly imaged using back scattering electrons by a field emission SEM (Gemini LEO 1530). The acceleration voltage varies in the range of 5-10 KeV. To record representative images, different spots are chosen for cross-checking.

AFM: To evaluate the surface roughness of deposited layers in my work, AFM (BE001207-G from Triple-O) is taken for scanning the surface with contacting model. To guarantee the surface roughness is representative, the scanning area is maximized to 4*4 μm and the measurement are carried out at two different spots.

XRD: The XRD instrument equips a Bruker D8 X-ray diffractometer with Cu target. X-ray wavelength is 1.5418 Å. 2θ ranges from 26 to 28° with a step 0.02° for the (112) diffraction peak of CIGSe absorbers.

XRF: The working principle of XRF is to collect the emission (including energy and intensity) of characteristic X-rays from a material that has been excited by bombarding

with high-energy X-rays. This measurement is carried out by a wavelength dispersive XRF instrument (ZSX Primus III+ from Rigaku). It can enable to quantitatively evaluate the element compositions of CIGSe absorbers by comparing the characteristic X-ray signals to the reference samples. Via the help of compound density and measured composition ratio, the thickness of CIGSe layers can also be determined.

GDOES: A GDOES measurement needs to place the sample as cathode (copper as anode). By discharging between cathode and anode, atoms on the surface of investigated samples are ejected in an excited state. The excited atoms will emit characteristic X-ray photons after relaxing back to the fundamental energy level. By collecting the X-ray photons, it allows to quantify surface element composition of the material. This working principle is similar to XRF. With an in-situ etching accessory, the bulk element information can be analyzed. In this work, GDOES is used to determine the [Ga]/[III] depth profile of CIGSe absorbers in chapter 2. The measurement is performed by a spectrometer (GDA 650 from Spectruma) with 2.5 mm anode and Ar discharge gas.

XPS: XPS is to analyze the kinetic energy and the amount of electrons escaping from a material surface by irradiating X-ray. It can be used to characterize the surface elements and their chemical states. By illuminating ITO substrate surface, whether the Ag nanoparticles underneath ITO penetrate through it or not can be confirmed after CIGSe deposition in chapter 5. The measurement is done on a VG Clam IV analyzer using Mg Kα X-ray (1253.6 eV) as the excitation energy from a SPECS XR 50 source.

***Optical characterization:***

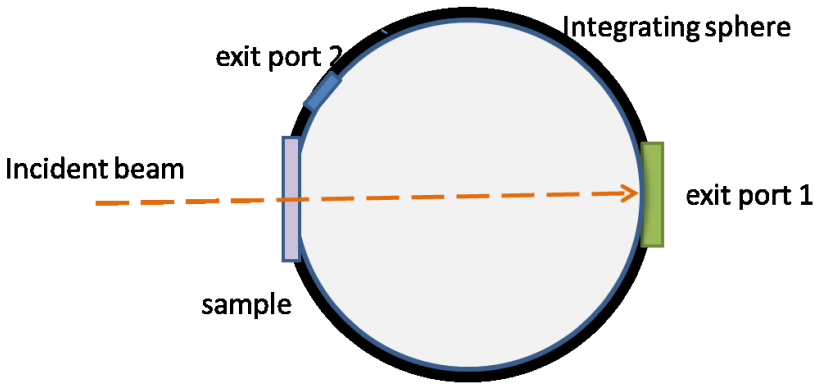


a) T

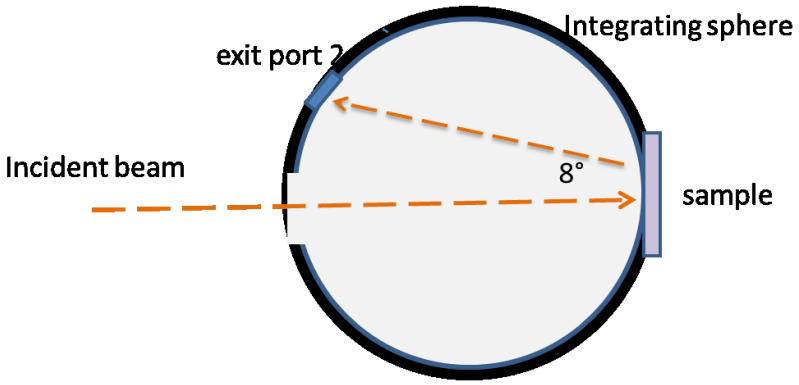


b) R

Fig.2.4 Measuremet setup of UV-Vis for a) T and b) R

*R/T* of samples under normal incidence are characterized by UV-Vis spectrometer with an integrating sphere (Lambda 950, PerkinElmer), which enables to evaluate both total *R/T* ($R_{tot}$ / $T_{tot}$) and diffused *R/T* ($R_{dif}$ / $T_{dif}$). The corresponding specular parts ($R_{spe}$/$T_{spe}$) can then be deduced from the differences of the total parts and the diffused. For R measurement, the sample is tilted by 8° from normal incidence to avoid the light escaping from beam-incident port. Fig.2.4 shows R/T measurement setup in the UV-Vis spectrometer. Exit port 1 and 2 should be taken off for diffused *T/R* ($R_{dif}$/$T_{dif}$) measurement, respectively. It is mentioned that the *R/T* signify the $R_{tot}$/$T_{tot}$ if it is not specified in the whole thesis.

To guarantee the accuracy of measurement, the illumination beam on the sample is set the maximum (1.5*0.7 cm) and the wavelength interval 4 nm. Besides, the blank measurements (without samples) are done for 100% *R/T* check after baseline calibration. The scanning wavelength ranges from 300-2000 nm.

***Electrical characterization:***

*J-V*: The current density- voltage *(J-V)* characteristics of solar cells are measured by a home-made sun simulator with both a Xenon and a Halogen lamp under standard test condition (AM 1.5, 100 mW/cm$^2$, 25 °C). The AM 1.5 condition is calibrated by a certified crystalline Si solar cell from the Fraunhofer Institute for Solar Energy Systems (ISE).

*EQE:* The external quantum efficiency (*EQE*) is for determining the electrical response of solar cells to the incident light in spectral resolution. The *EQE* measurement is

carried out with a two-source illumination system of a Xenon and a Halogen Lamp, using a calibrated Si and Ge diode as references in my work.

## 2.4 Enhanced performance of ultra-thin solar cells at low temperature

Ultra-thin CIGSe solar cells with absorber thickness below 0.5 μm have experimentally shown considerably poor performances mainly in terms of substantial drop of $J_{sc}$. Between the two main factors behind, the incomplete absorption is inevitable due to the absorber thickness reduction without light-trapping technologies. For the back recombination, it not only decreases $J_{sc}$ and but also deteriorates $FF$ and $V_{oc}$ of solar cells. To obtain highly efficient ultra-thin solar cells, we should both reduce the back recombination and enhance the absorption. The first step is to reduce the back recombination, otherwise the enhanced absorption will be discounted by the back recombination. Therefore, in this section, my work is mainly related to reducing the back recombination and obtaining efficient ultra-thin solar cells for the further implementation of light-trapping technologies.

The 3-stage co-evaporation deposition process can normally result in a double-graded [Ga]/[III] profile with a higher [Ga]/[III] ratio towards both the back and surface of the absorber, and a typical notch point with the lowest [Ga]/[III] ratio closer to the upper surface [35]. It has been extensively investigated that the graded [Ga]/[III] towards the back contact (the back Ga grading) in CIGSe absorbers can serve as an electron back repeller and thus reduce the back recombination [10]. The bandgap of CIGSe phases is proportional to the [Ga]/[III] ratio in terms of increasing the conduction band (CB). Fig.2.5 illustrates a typical band diagram of CIGSe solar cell. The front CB grading is offset due to the band bending at the p-n interface. The resulting CB grading is obvious and can form an additional potential $\Delta\psi$ for electrons to overcome for diffusing to the back interface. Therefore, the higher back Ga grading is desired for reducing the back recombination.

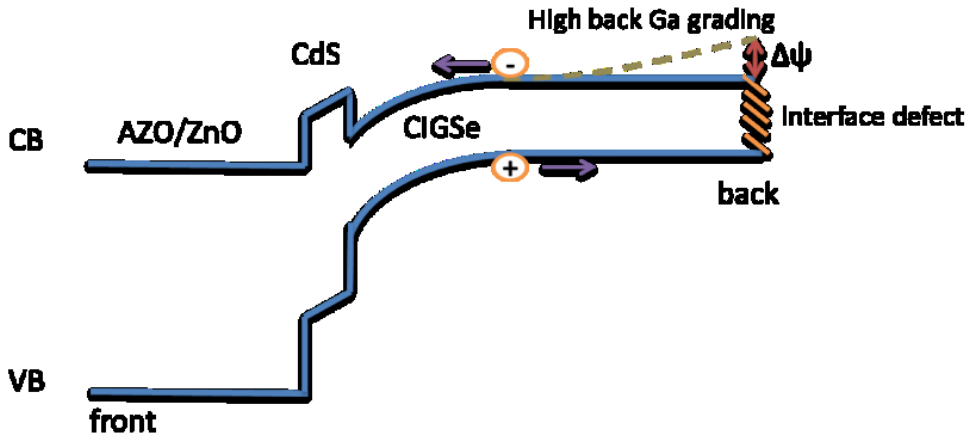


Fig.2.5 Band diagram of the CIGSe solar cell where the dotted line represents a higher back Ga grading

In the 3-stage process, lowering substrate temperature ($T_s$) was verified to be able to reduce the inter-diffusion of Ga-In [38] and therefore provides the possibility to create a higher back Ga grading by tuning the deposition sequence of Ga-Se precursor prior to In-Se. Another benefit of the low substrate temperature is the realization of the preparation of CIGSe solar cells on flexible polymer substrates [38, 39] and thus offering a potential to further reduce the manufacturing cost.

However, high-quality CIGSe absorbers are normally deposited above 500 °C. Kaufmann [38] lowered the substrate temperature for solar cells with an approximate 2-μm thick absorber. The $\eta$ deteriorated severely due to the large drop of $V_{oc}$ and $FF$ even with the increase of $J_{sc}$ at lower deposition temperature. This is attributed to the poor quality of CIGSe absorbers deposited at low substrate temperature and a higher bulk recombination. Whereas, the space charge region (SCR) [40, 41] normally is 300-500 nm thick and is comparable to the thickness of ultra-thin absorbers. This indicates that photo-generated carriers are mostly located within the SCR, carrier collection efficiency is less influenced in the case of decreased lifetime of carriers resulting from a poor CIGSe quality. For the identification of this, solar cells deposited at both high ($T_s = 610$ °C) and low ($T_s = 440$ °C) substrate temperatures are investigated. To potentially create a high back Ga grading, the Ga-Se precursor was evaporated prior to In-Se. Fig.2.2 presents the LLS signal diagram of the whole evaporation process, which corresponds to the temperature $T_s$ at 440 °C. The overall [Ga]/[III] and [Cu]/[III] ratio in both temperature cases are 0.4±0.01 and 0.86±0.01, respectively. The thickness is 460±5nm.

## 2.4.1 Morphology and [Ga]/[III] depth profile

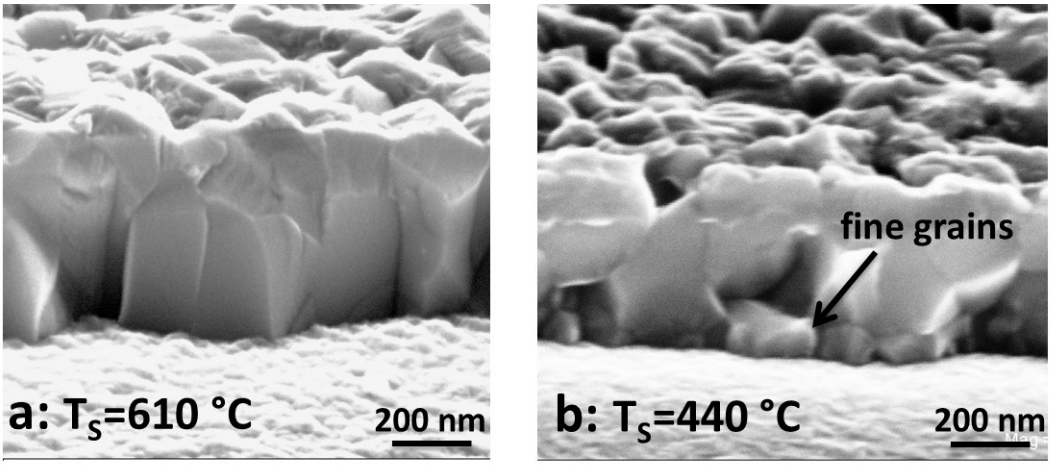


Fig.2.6. Cross sections of the CIGSe layers on Mo substrate at substrate temperatures of a) $T_S$ = 610 °C, b) $T_S$ = 440 °C

During the 3-stage process deposition, the maximum substrate temperature $T_S$ predominates the growth and morphology of the absorbers, which is also reflected in Fig.2.6. At $T_S$ = 610 °C, the layer is quite compact with closely-packed grains extending through the entire thickness. At $T_S$ = 440 °C, we can observe smaller grains, especially near the Mo back contact. This is a sign for a poor quality absorber at low temperature. Fig.2.7 a) shows the preferential (112) XRD diffraction peaks of the absorbers at both temperatures. The absorber deposited at $T_S$ = 610 °C exhibits a single and sharp (112) peak. When $T_S$ drops to 440 °C, the peak evolves into a broad double-peak with the sub-peaks locating at each side of the single peak corresponding to $T_S$ = 610 °C. Because of a larger atomic radius of In than Ga, as the [Ga]/[III] ratio increases, the peak position is evolving from CISe with the lowest 2 theta value to CGSe with the highest. Since the two absorbers have the same overall [Ga]/[III] ratio , the double-peak at $T_S$ = 440 °C indicates a reduced inter-diffusion of Ga-In. Plus the fact of the intentional deposition of Ga-Se precursor before In-Se during the 1$^{st}$ stage of the 3-stage deposition, the higher [Ga]/[III] CIGSe phases near the back Mo contact are expected. GDOES results of the [Ga]/[III] depth profiles across the absorbers in Fig.2.7 b) further confirmed the XRD estimation. At $T_S$ = 610 °C the absorber shows a relatively flat [Ga]/[III] depth distribution, while at $T_S$ = 440 °C the [Ga]/[III] distribution has a distinct grading towards both surface and back side, particularly towards the back side. Because of the linear dependence of the bandgap of CIGSe phases on the [Ga]/[III] ratio varying from

1.01 (CISe) to 1.67 eV (CGSe), it can be deduced that $E_{g,min}$ for the absorber at $T_S$ = 440 °C is lower than that at $T_S$ = 610 °C as seen from Fig.2.7 b). Conclusively, the high back Ga grading is created by the deposition of Ga-Se before In-Se in the 1st stage at $T_S$ = 440 °C.

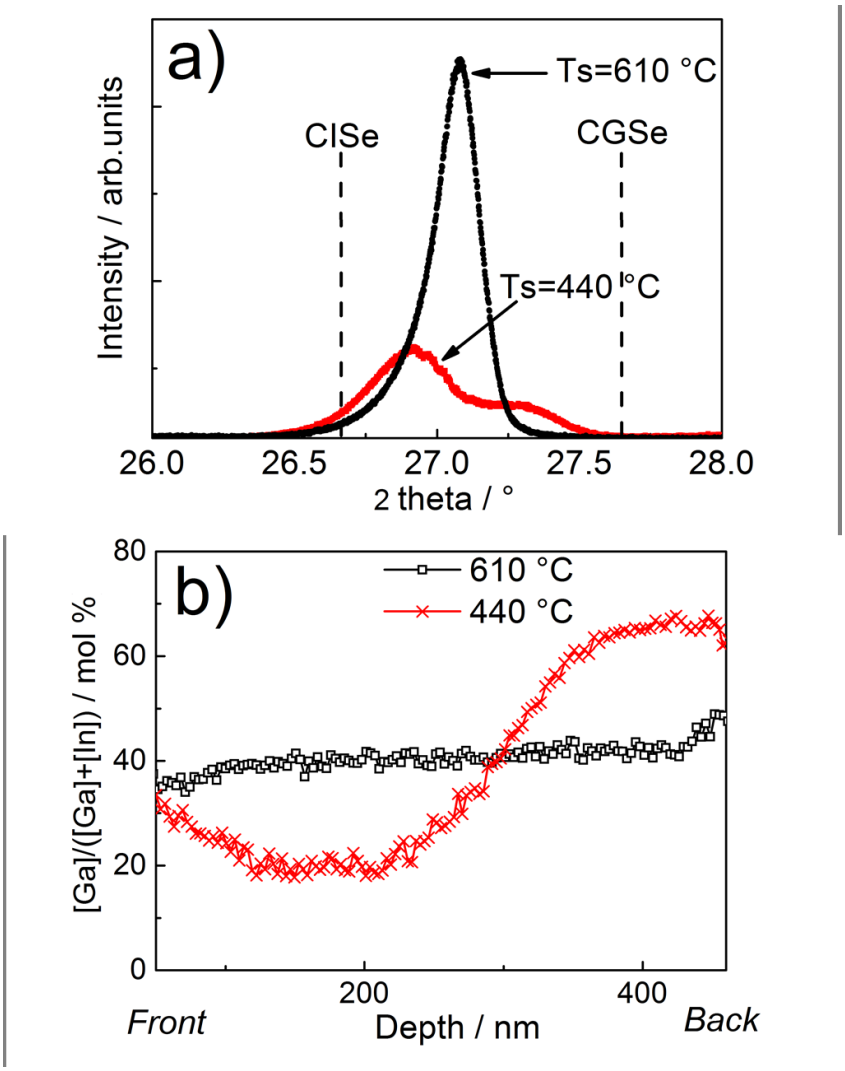


Fig.2.7 a) (112) XRD diffraction peaks and b) the corresponding [Ga]/[III] depth profiles evaluated by GDOES at both temperatures

## 2.4.2 Device performance

Fig.2.8 compares the *J-V* performances of the solar cells at two different substrate temperatures. As the temperature is lowered to $T_S$ = 440 °C, $V_{oc}$ decreases moderately by 5.3%, which can be mainly interpreted due to the lower $E_{g,min}$ at low temperature, but the substantial increase of $J_{sc}$ and maintained *FF* contribute to the considerable net enhancement (relatively 17.8%) in efficiency. Generally a poorer quality of absorbers is

expected at lower substrate temperature and this can result in a large drop of $V_{oc}$ and $FF$. However, the maintained $FF$ and only relatively moderate drop of $V_{oc}$ of the solar cells at low substrate temperature imply a weak influence of the poor absorber quality. Apart from the reason mentioned above that ultra-thin solar cells are more tolerant towards the quality of absorbers, the higher back Ga grading is another one. This reduces the back recombination and enhances the carrier collection efficiency for the solar cells at $T_S$ = 440 °C. The improved carrier collection not only enhances $J_{sc}$, but also improves $FF$ and $V_{oc}$.

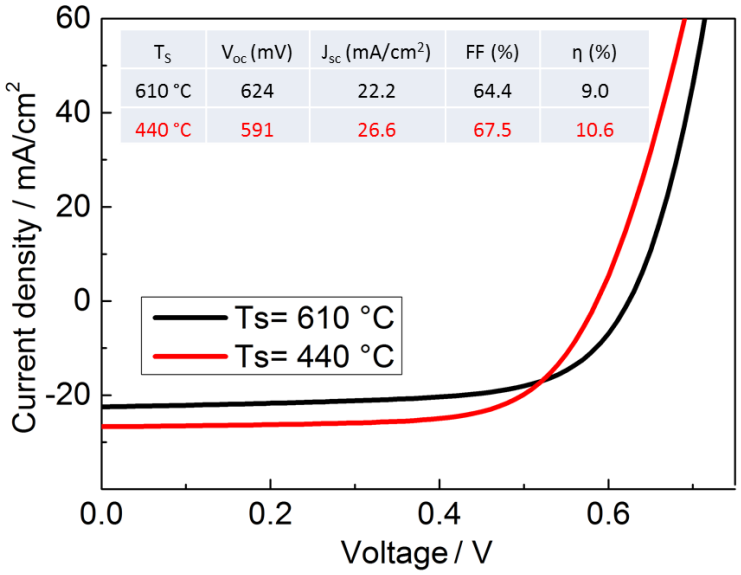


| $T_S$ | $V_{oc}$ (mV) | $J_{sc}$ (mA/cm$^2$) | FF (%) | η (%) |
|---|---|---|---|---|
| 610 °C | 624 | 22.2 | 64.4 | 9.0 |
| 440 °C | 591 | 26.6 | 67.5 | 10.6 |

Fig.2.8 $J$-$V$ device performances under standard AM 1.5 illumination (average results from 6 solar cells at each substrate temperature), the inset table is the $J$-$V$ parameters extracted from the corresponding curves.

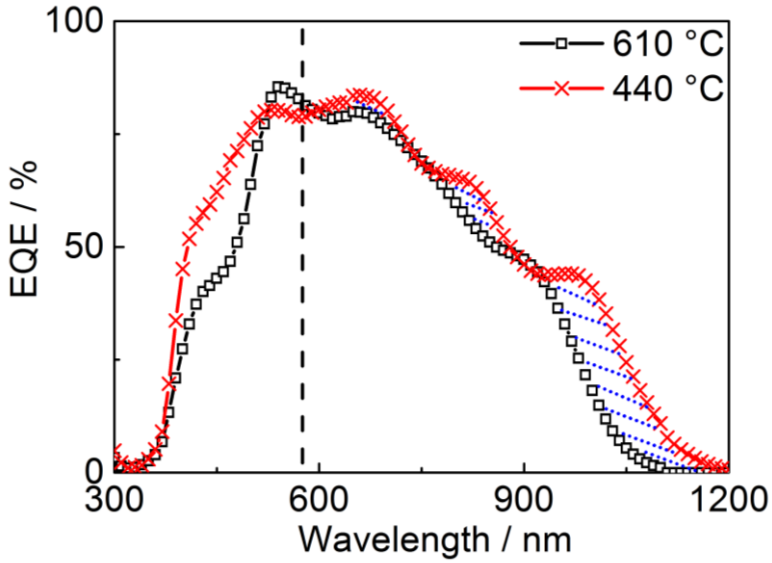

Fig.2.9 External quantum efficiency (*EQE*) of solar cells with absorbers deposited at $T_S$ = 610 °C and $T_S$ = 440 °C

Fig.2.9 displays the *EQE* curves of the solar cells at two different temperatures $T_S$. There is an overall improvement for the solar cells at $T_S$ = 440 °C with respect to those at $T_S$ = 610 °C. The improvement is agreeable with the increase of $J_{sc}$ shown in Fig.2.8. In the wavelength range below 580 nm, the enhancement is possibly due to the variation of the thickness of CdS. The enhancement above the wavelength of 600 nm is attributed to the high back Ga grading for the solar cell deposited at $T_S$ = 440 °C. It accounts for 67% of the overall enhancement in $J_{sc}$. It should be stressed here that the improvement above the wavelength of 600 nm is not only due to the electrical benefit of the back Ga grading in terms of reducing back recombination. Furthermore, a lower $E_{g,min}$ for the absorber at $T_S$ = 440 °C indicates a broader absorption spectrum. This can also be reflected by the corresponding *EQE*, which shows a broader collection wavelength range. To quantitatively prove this, the extinction coefficient *k* of each absorber on glass substrate was calculated and are illustrated in Fig.2.10. α is derived by equation $\alpha = 4\pi k/\lambda$ ($k$ is the extinction coefficient, $\lambda$ is the wavelength). The evaluation of $k$ will be detailed in the extraction of optical constants in the chapter 3. It can be observed that the absorber deposited at $T_S$ = 440 °C exhibits absorption ability not only in a broader spectrum range than that at $T_S$ = 610 °C, but also higher beyond 930 nm. This indicates that the [Ga]/[III] depth profile can also influence the absorption coefficient α, even though the overall [Ga]/[III] ratio is the same. This disobeys the normal assumption that the overall [Ga]/[III] ratio determines the absorption coefficient α in literature [29, 42].

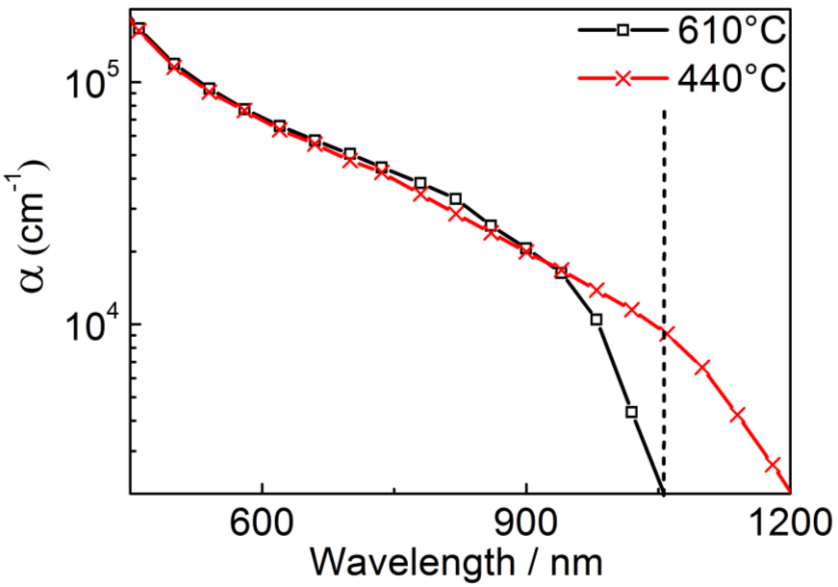


Fig.2.10 Calculated absorption coefficient α of reference samples on glass substrate at varied substrate temperatures of $T_S$ = 610 °C and $T_S$ = 440 °C. The evaluation details are introduced in Chapter 3.

## 2.4.3 Conclusion and outlook

Ultra-thin CIGSe absorbers were fabricated by 3-stage co-evaporation process at two substrate temperatures of 440 °C and 610 °C. It was discovered that the low substrate temperature could preserve the intentional deposition sequence of Ga-Se prior to In-Se and create a higher back Ga grading than the high temperature. The ultra-thin solar cells benefit from the higher back Ga grading in the form of greatly improved short circuit current density $J_{sc}$ and the efficiency $\eta$ is thus enhanced. Apart from the reduced back recombination, it is evidenced that a higher Ga grading can further enhance $J_{sc}$ by improving the absorption ability in the long wavelength range.

Even $J_{SC}$ is largely improved to 26.6 mA/cm$^2$ in my ultra-thin solar cells prepared at temperature of 440 °C, $J_{SC}$ is still far below that of a typical CIGSe solar cell with 2-µm thick absorber (around 35 mA/cm$^2$). To realize further increase of $J_{SC}$ and highly efficient ultra-thin solar cells, implementation of light trapping technologies is therefore essential. Integrating plasmonic metallic and dielectric nanostructures into solar cells is of high interest for the potential to effectively increase the propagation path of light and $J_{SC}$. Unlike the amorphous silicon solar cells, which can be prepared at low substrate temperature, the CIGSe absorber is normally deposited above 500°C for well-performed solar cells. The materials of light-trapping structures may thermally destabilize at such a

high temperature. For example, this high temperature is enough to trigger the diffusion of Ag and Au nanoparticles, so the integration of metallic nanoparticles is not feasible without any passivation layers before the CIGSe deposition. However, a low substrate temperature may help maintain the stability and properties of light-trapping materials. Further, better bare ultra-thin solar cells are obtained at low temperature as proved above. Therefore, the low substrate temperature is highly recommended to realize highly efficient ultra-thin CIGSe solar cells. In the chapters 4-7 related to the incorporation of light-trapping structures into solar cells, the solar cells are prepared at low substrate temperature.

# Chapter 3

# Optical constants for $CuIn_{1-x}Ga_xSe_2$ solar cells

As concluded in the last chapter, a low deposition temperature can improve the short circuit current density ($J_{sc}$) for ultra-thin CIGSe solar cells, but $J_{sc}$ is still far below the reported value from the typical thick solar cells. To further enhance $J_{sc}$ and achieve highly efficient ultra-thin solar cells, light trapping is necessarily required. Due to the complexity of light propagating, theoretical optical simulation is indispensable for guiding how to select the optimum light-trapping structures and understanding how the light-trapping structures work. Optical constants (refractive index $n$, extinction coefficient $k$) or complex refractive index ($n + ik$) are the basic parameters to describe how light propagates through materials. The optical constants of each layer in the solar cell are necessary for optical simulations and quantitative calculation of optical properties of the whole device, e.g. absorbance (*Abs*), reflectance ($R$) and transmittance ($T$). Optical constants of each layer in CIGSe solar cells have been already extensively studied in the past [29, 42-45]. However, great discrepancies are found among the optical constants available in the literature, which can lead to the poor applicability of literature data in optical simulations for specific samples. Fig.3.1 (a) presents an example of optical constants of CISe (x = 0) from literature [29] and [45]. It is well known that the experimental parameters can affect the growth and resulting properties (including optical constants) of thin films. This has been proven to be strongly pronounced for the ternary or quaternary CIGSe compounds [46]. Although the error in the extraction of optical constants always exists, it is assumed that the dominant cause for discrepancies of optical constants arises from physical differences in the investigated samples, rather than experimental uncertainties.

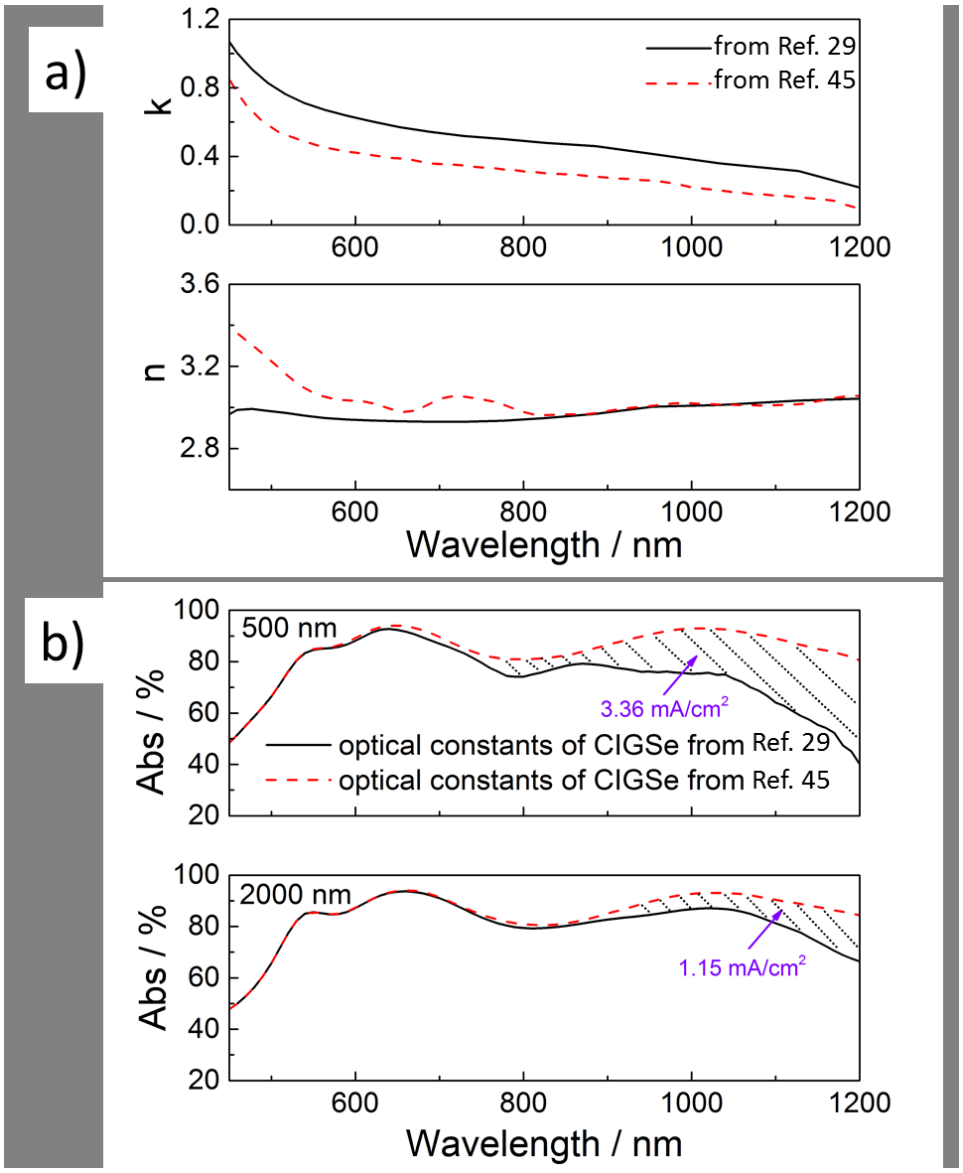


Fig.3.1 a) Comparison of two sets of optical constants of CISe compounds from literature, b) the corresponding simulated *Abs* of the CISe layer in the device structure of AZO/ZnO/CdS/CISe/Mo for both thicknesses of 500 and 2000nm. The corresponding thicknesses of rest layers are the same as in Fig.2.1 and the optical constants are shown in section 3.3.

Amongst the layers of the device, the CIGSe absorber determines the optoelectronic properties of a solar cell device to a great extent, accurate optical constants of this layer are hence more critical for precise device simulations. To illustrate the impact from the discrepancies of optical constants of an absorber layer on the optical properties of the entire device, two sets of optical constants of CISe in Fig.3.1 (a) are applied for the simulation in the device structure of AZO/ZnO/CdS/CISe/Mo. The corresponding *Abs* of the CISe layer for both thicknesses of 2000 and 500 nm is calculated and shown in

Fig.3.1 (b). The calculation is based on Transfer-Matrix method, which will be introduced in the following. We can clearly observe that the *Abs* difference is much larger for the device with a 500-nm-thick CISe layer than that with a 2000 nm. With the consumption of complete conversion of absorbed photons to current under standard AM 1.5 illumination irradiation, the corresponding deviation of $J_{sc}$ can reach 1.15 mA/cm$^2$ for the 2000-nm-thick CISe layer and 3.36 mA/cm$^2$ for the case of 500 nm. This indicates the necessity of accurate and realistic optical constants for device simulations, especially for the ultra-thin CIGSe solar cells.

In this chapter, I will extract the optical constants of each layer in the CIGSe solar cell prepared in my work, with special emphasis on the CIGSe absorber layer. To extract the practical optical constants, we need firstly to choose a proper determination method, secondly to prepare the required thin-film samples and finally to characterize the samples optically and do the determination.

## 3.1 Determination of optical constants

To determine the optical constants, the priority is to choose an appropriate method. The optical constants of solids can be in principle obtained by either polarimetric or photometric methods [47]. The polarimetric method evaluates the optical constants by comparing the polarization change (amplitude ratio and phase difference) of the incident and the reflected (or transmitted) beam with oblique incidence. While the photometric method focuses on the intensity measurement of *R/T*. One further advantage of the latter method is that the optical measurement can be carried out at normal incidence. It can exclude the influence of the polarization of light and can be conveniently accessed in the lab. Therefore, the photometric method is preferred in this work.

Optical constants can only be determined based on optical measurements instead of being measured directly. The next step is to extract the optical constants by matching the simulated optical responses to the measured. Generally two approaches are implemented. One is applying the physical dispersion models to describe the spectral responses of the investigated materials [48]. The optical constants can be determined by optimizing the parameters in the physical modes until the difference between the simulated optical responses and the measured is minimized over the WHOLE interested spectrum. The disadvantage of this approach is that the existing physical modes cannot

always describe the optical responses of materials accurately due to the complexity of materials themselves. Plus you should know the properties of the material very well. These two points limits the extraction of optical constants. Additionally, the determination process is really time-consuming because of many parameters needing to be optimized in the physical modes. In contrast to the extraction approach based on the physical dispersion models, there is a model-free approach (also called point-to-point way by Orgassa [29]), which can extract the optical constants in terms of minimizing the difference of the simulated optical responses and the measured for each SINGLE wavelength. The advantage of this model is that the related physical information of the investigated materials is not necessarily needed. However, the drawback is that non-physical evaluation can occur in certain narrow wavelength range arising from experimental errors. Considering the complexity of ternary and quaternary CIGSe compounds, the model-free approach is overall favoured. As to the non-physical evaluation in certain wavelength range, this can be interpolated by the physical meaningful values in the neighboring wavelengths due to the continuous dispersion property of optical constants. This was well explained in Ref [29] and an example will be also shown in the following.

Concerning the motivation to obtain the optical constants matching the corresponding materials in the solar cell as closely as possible, Transfer-Matrix method [49-53] is applied. The reasons are as follows: 1) Transfer-Matrix method can be sorted to the photometric method under normal incidence; 2) The optical property (*R/T*) characterization under normal incidence can be easily implemented in my experiments; 3) Transfer-Matrix method allows for the model-free extraction approach.

### 3.1.1 Transfer-Matrix (TM) method

***Working principles***

The TM method is a 1D simulation model for light propagation inside a layer stack structure taking multiple reflections into account. It has been investigated in detail to calculate *R/T* for a layer stack structure. In the following, we will describe how the TM method works.

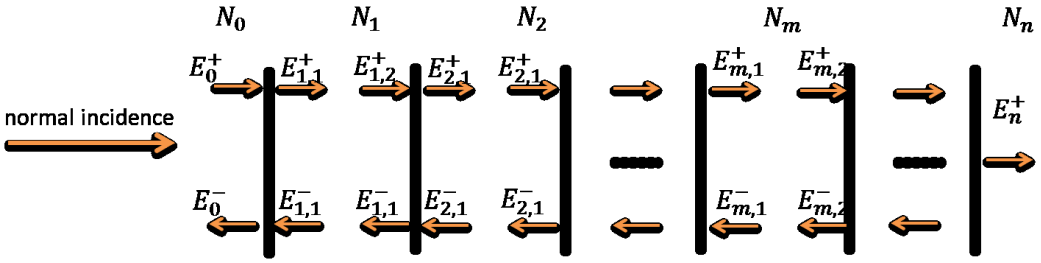


Fig.3.2 Schematic of the electric field in the layer stacked structure under normal incidence. The sign + and – as to the subscript of electric field amplitude ($E$) indicates the forward and backward component.

Fig.3.2 illustrates the electric field distribution at each interface in the layer stack structure. At each interface, one part of the incident light will be transmitted to the adjacent medium and the other part reflected. Thereby the electric field of the electromagnetic wave in each medium is divided into two parts: the forward part ($E^+$) and the backward ($E^-$). The electric field amplitudes $E^+$ and $E^-$ in each layer and subsequently $T_{cal}$ and $R_{cal}$ can be connected by the TM method. To make the subscripts of symbol $E$ more clear, $E_{m,1}$, taking as an example, presents the electric field at the left side within the m$^{th}$ layer. Similarly, $E_{m,2}$is for the right side.

The electric fields at both sides of an interface are defined by:

$$\begin{pmatrix} E_{m,2}^+ \\ E_{m,2}^- \end{pmatrix} = \mathrm{M}_{\mathrm{m,m+1}} \begin{pmatrix} E_{m+1,1}^+ \\ E_{m+1,1}^- \end{pmatrix} \quad 3\text{-}1$$

$$\text{where } \mathrm{M}_{\mathrm{m,m+1}} = \frac{1}{t_{m,m+1}} \begin{pmatrix} 1 & r_{m,m+1} \\ r_{m,m+1} & 1 \end{pmatrix} \quad 3\text{-}2$$

$t_{m,m+1}$, $r_{m,m+1}$ are the transmission and reflection Fresnel coefficient, respectively, and they are a function of complex refractive indexes $N = n + \mathrm{i}k$ or optical constants ($n$, $k$) of the media forming the interface.

$$t_{m,m+1} = \frac{2N_m}{N_m - N_{m+1}} \quad 3\text{-}3$$

$$r_{m,m+1} = \frac{N_m - N_{m+1}}{N_m + N_{m+1}} \quad 3\text{-}4$$

The electric fields at the left and right side of the $m$th layer are related by:

$$\begin{pmatrix} E_{m,1}^+ \\ E_{m,1}^- \end{pmatrix} = D_m \begin{pmatrix} E_{m,2}^+ \\ E_{m,2}^- \end{pmatrix} \quad 3\text{-}5$$

$$\text{where } D_m = \begin{pmatrix} e^{-i\theta_m} & 0 \\ 0 & e^{i\theta_m} \end{pmatrix} \quad 3\text{-}6$$

$\theta_m$ is the phase shift of light propagating through the $m$th layer ,and is given by

$\theta_m = 2\pi N_m d_m / \lambda$ . $N_m$ and $d_m$ are the complex refractive index and the thickness of the $m$th layer, respectively. In principle, we could apply the matrix transformations deduced above to connect the electric field amplitudes from the incident medium to outgoing medium:

$$\begin{pmatrix} E_1^+ \\ E_1^- \end{pmatrix} = M_{0,1}\, D_1\, M_{1,2}\, D_2\, M_{2,3} \ldots \ldots \begin{pmatrix} E_n^+ \\ 0 \end{pmatrix} \qquad 3\text{-}7$$

After squaring the electric field, we can in principle obtain the relationship of the incident ($I_{in}$), the reflected ($I_r$) and the transmitted ($I_t$) light intensity. It should be more detailed that light reflected from two interfaces is not phase coherent when light propagates through a thick film (eg. glass substrate), the phase relation does not need to be considered. Whereas light propagating through a thin film is phase coherent. In order to deal with coherent propagation within thin films and incoherent propagation through thick substrates together, Harbecke [49] proposed to decompose the layer structure into thin and thick sub-layer structures, each sub-structure forms its own transfer matrix $P^{coh}$ or $P^{inc}$. The relation equation of electric field (3-7) can be abbreviated as:

$$\begin{pmatrix} E_1^+ \\ E_1^- \end{pmatrix} = P_1^{coh} P_1^{inc} P_2^{coh} P_2^{inc} P_3^{inc} \ldots \begin{pmatrix} E_n^+ \\ 0 \end{pmatrix} \qquad 3\text{-}8$$

Then square each transfer matrix separately and connect each other by multiplication. Finally, the relationship of the incident ($I_{in}$), the reflected ($I_r$) and the transmitted ($I_t$) light intensity can be given as follows:

$$\begin{pmatrix} I_{in} \\ I_r \end{pmatrix} = \begin{pmatrix} S_{11} & S_{12} \\ S_{21} & S_{22} \end{pmatrix} \begin{pmatrix} I_t \\ 0 \end{pmatrix} \qquad 3\text{-}9$$

So it is easy to derive the analytical expressions of $T_{cal}$ and $R_{cal}$:

$$R_{cal} = \frac{S_{21}}{S_{11}} \qquad 3\text{-}10$$

$$T_{cal} = \frac{1}{S_{11}} \qquad 3\text{-}11$$

From the equations acquired above, the analytical expressions of $R_{cal}$ and $T_{cal}$ are a function of optical constants via Fresnel coefficient and thickness of each layer. Vice versa, we can calculate the optical constants of an arbitrary layer by comparing the analytical expressions ($R_{cal}$ / $T_{cal}$) to the measured data ($R_{mea}$ / $T_{mea}$) if the optical constants and thickness of other layers are known.

To simplify the calculation, each layer in the solar cell is deposited on glass substrate for my experimental sample and the exemplary structure is shown in Fig.3.3.

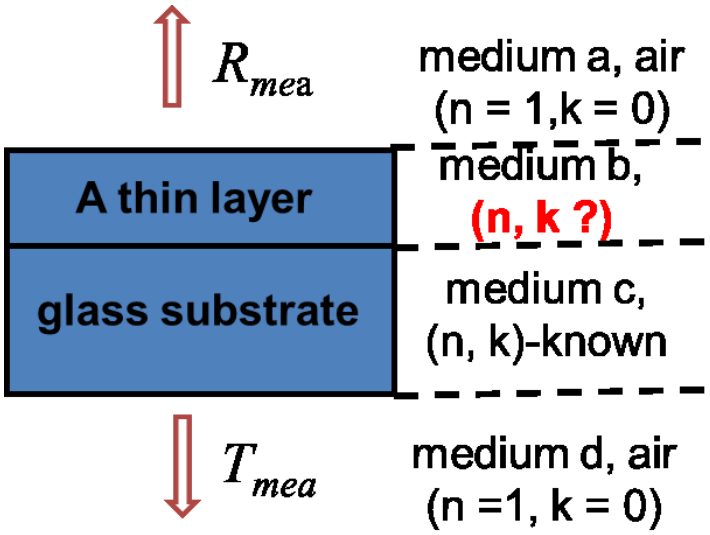


Fig.3.3 The layer stack structure of the experimental sample for determination of optical constants

The structure is composed of 4 media: air (a) / a thin layer (b) / an optically thick layer (c) / air (d) and is under normal incidence of light from the thin layer side. The thicknesses of the film (medium b) and the substrate (medium c) can be measured, the optical constants of the substrate ($n_c$,$k_c$) and of air are known. $R_{mea}$ and $T_{mea}$ can be characterized by UV-Vis spectrometer. Then two implicit equations (Eq. 3-12), (3-13)) can be determined by TM method with two variables of optical constants of medium b ($n_b$,$k_b$) for each wavelength:

$$R_{cal}\left(n_b(\lambda), k_b(\lambda)\right) - R_{mea}(\lambda) = 0 \qquad 3\text{-}12$$

$$T_{cal}\left(n_b(\lambda), k_b(\lambda)\right) - T_{mea}(\lambda) = 0 \qquad 3\text{-}13$$

Here, $\lambda$ is the wavelength.

## 3.1.2 Computation of optical constants

Each single layer in the solar cell was prepared on glass substrate (microscopy slide, No. 2211861 from Marienfeld GmbH) according to the recipe described in section 2.3. Both $R_{tot}/T_{tot}$ and $R_{dif}/T_{dif}$ measurements were carried out in the wavelength range of 300-2000 nm with incident light towards the thin layer side.

For CIGSe, to establish an optical constant database of $CuIn_{1-x}Ga_xSe_2$ covering the whole [Ga]/[III] range, samples for x = 0 (CISe), x = 0.19, x = 0.33, x = 0.48, x = 0.53, x = 0.77, x = 0.92, x = 1.00 (CGSe), were prepared by varying Ga, In deposition time in the first stage. $T_s$ was set 610 °C. The thickness varies from 400-500 nm.

***Thickness determination***

Regarding the identification of thickness, the glass substrate is an incoherent and a non-absorbing layer, its thickness accuracy does not matter. However, the calculated optical constants are very sensitive to the thickness of the thin layer. To accurately identify the thickness of the thin layer, three ways are cross checked. Apart from the cross sections of SEM, the thicknesses of CIGSe layers can be evaluated by XRF as mentioned before. In addition, the TM method enables to confirm the thickness by minimizing the solution discontinuities in the non-absorbing wavelength range. It was mentioned in Ref [54] and will be repeatedly explained below. This is also the reason that samples are characterized optically in the non-absorbing wavelength range beyond 1300 nm.

A program named RefDex [55] based on TM method is developed and intended for the calculation of optical constants as well as inversely for *R/T* calculation of a flat layer-stack structure. In the following, I will first show how to determine the optical constants in the example of a CGSe ($x = 1$) sample.

***Multiplicity of solutions and solution branch gaps***

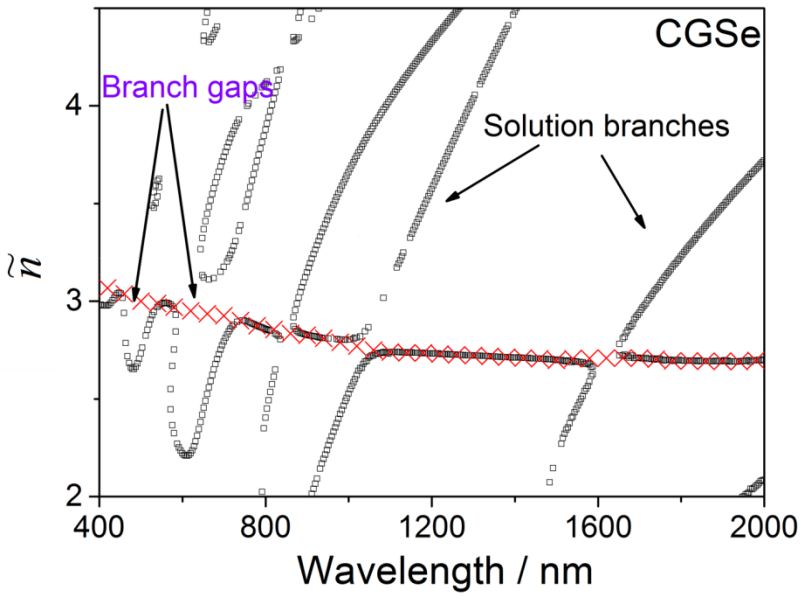


Fig.3.4 Multiple solutions of refractive index for a CGSe sample on glass substrate. The green-dotted line corresponds to the physically meaningfully values

Fig.3.4 presents the curve of computed refractive index ($n$) values of CGSe, multiple $n$ solutions (expressed in the symbol of $\tilde{n}$) are observed. To begin with, I should stress that the existence of multiple solutions, which originate from the nature of the complex implicit equations (Eqs.(12) and (13)), is the main disadvantage of TM method [29, 56]. The multiplicity of solutions for $n$ is more complicated with respect to that of the extinction coefficient ($k$), only $n$ is thereby shown here.

Another feature can be observed: the multiplicity of solutions forms solution branches. Theoretically, the adjacent solution branches should coincide tangentially and form a continuous dispersion curve, which corresponds to the physically meaningful values [54]. However, the adjacent solution branches fail to be in good tangency and discontinuities (called branch gaps) appear especially in the short wavelength range. This signifies that no physically meaningful value can be found at the branch gaps. Any uncertainties, such as interface roughness, voids within the film, thickness inhomogeneity, a thin oxide layer on the surface, the thickness determination error, imperfect monochromaticity of measured incident light etc., can also reduce the applicability of TM method and lead to branch gaps as well [57, 58]. Anyway, TM method in the long wavelength range becomes more tolerant to these uncertainties, which indicates the branch gaps in the long wavelength range can be relatively smaller

or even disappear. Since the influence of these experimental uncertainties except the thickness error is inevitable for a specific sample, therefore the branch gaps should be small in the long wavelength range if the input thickness value is accurate. We can use this criterion to finely tune the input thickness value until the brand gaps are minimized.

***Extraction of physically meaningful values***

The next critical point is how to extract the physically meaningful refractive indexes from the multiple solutions and to deal with the wavelength range of branch gaps. Orgassa [29] recommended using the existing literature data to confine the selection range. For CGSe, only the solution braches lying around $n$ = 3 are physically meaningful. At this range, we can observe a relatively continuous line with branch gaps indicated by the green dotted line. This corresponds to the physically meaningfully refractive indexes for the sample CGSe. For branch gaps, many data points are extracted from the physically meaningful branch and forms a spline function, which can interpolate data points at solution branches (for more details about the selecting criteria and related, see Ref. [29]).

***Wavelength application range of TM method***

TM method can only be applied for the calculation of optical constants during the wavelength range where $T > 0$. In the opaque wavelength range (below 400 nm for the CGSe sample in Fig.3.4), TM method would assume that T just reaches zero when the incident light penetrates the film, which is not the practical case that T is already zero within the film. However, the propagating length of light in the simulation is assumed to be the thickness of a film and the calculated $k$ values will be therefore reduced. The interested spectrum range for CIGSe solar cells is around 300-1200 nm. The wavelengths in the range of 300-500 nm will be mostly absorbed by the window and buffer layers, so the inaccuracy of the optical constants of CIGSe layers in the range of 300-500 nm will influence little for the complete solar cell simulation. As to the transparent wavelength range (1300-2000 nm), it is also investigated for my samples. Two reasons contribute to this: firstly $R+T = 100\%$ can be used to confirm the accuracy of optical characterization, further as mentioned above, solution branch gaps in this range can help to judge the accuracy of the input thickness of a thin layer.

## 3.2 Optical constants of CIGSe layers

As stated above, the CIGSe layer determines the optoelectronic properties of solar cells to a great extent, so the accuracy of the optical constants of CIGSe is highly critical for the device simulation and should be emphasized.

### 3.2.1 Influence of surface roughness

The interface roughness disobeys the flat-interface assumption of TM method and thus reduces its applicability to CIGSe samples. This is because TM method could not treat the partially coherent propagation of light (scattered part), which usually results from interface roughness. In the case of CIGSe samples in this work, there are 3 interfaces: Air/glass, glass/CIGSe, CIGSe/air. Since the glass substrate is quite flat and the CIGSe layer is compact, the roughness mainly stems from the interface of CIGSe/air. The surface roughness is an inherent property and can negatively influence the accuracy of calculations. TM method is expected to suit the smoothened samples much better and the branch gaps should be narrower. However, the smoothing process takes efforts and has the risk of damaging the samples. J Szczyrbowski [57] proposed the scalar scattering theory to consider the influence of surface roughness on *R/T* at a single interface and to establish the relationship between specular part ($R_{spe}/T_{spe}$) on the rough surface and the total ($R_s/T_s$) on the smooth surface. Eqs. 3-14 and 3-15 give this relationship:

$$R_{spe} = R_s exp\left[(\frac{4\pi\sigma}{\lambda})^2\right] \quad 3\text{-}14$$

$$T_{spe} = T_s exp\left[(\frac{4\pi\sigma}{\lambda})^2 (n_m - n_{m+1})^2\right] \quad 3\text{-}15$$

Here, σ is the surface roughness in terms of root mean square (RMS) value.

With the consideration of multiple reflections at interface, Fresnel coefficients are modified to establish the relationship and are as follows:

$$r'_{m,m+1} = r_{m,m+1} exp\left[-2\left(\frac{2\pi\sigma}{\lambda}\right)^2 {n_m}^2\right] \quad 3\text{-}16$$

$$r'_{m+1,m} = r_{m+1,m} exp\left[-2\left(\frac{2\pi\sigma}{\lambda}\right)^2 {n_{m+1}}^2\right] \quad 3\text{-}17$$

$$t'_{m,m+1} = t_{m,m+1} exp\left[-\left(\frac{2\pi\sigma}{\lambda}\right)^2 (n_m - n_{m+1})^2/2\right] \quad 3\text{-}18$$

$$t'_{m+1,m} = t_{m+1,m} exp\left[-\left(\frac{2\pi\sigma}{\lambda}\right)^2 (n_m - n_{m+1})^2/2\right] \quad 3\text{-}19$$

Where $r'_{m,m+1}$, $r'_{m+1,m}$ $t'_{m,m+1}$ $t'_{m+1,m}$ denote the corresponding modified Fresnel coefficients. They are used to replace Fresnel coefficients in Eqs. 3-12, 3-13.

In principle, this can be inversely applied for the calculation of optical constants of samples with interface roughness. This method is defined as modified Transfer-Matrix method in this work (abbreviated as TMT method). Subsequently, the Eqs. 3-12, 3-13 evolve to:

$$R'_{cal}\big(n_b(\lambda), k_b(\lambda)\big) - R_{spe}(\lambda) = 0 \qquad 3\text{-}20$$

$$T'_{cal}\big(n_b(\lambda), k_b(\lambda)\big) - T_{spe}(\lambda) = 0 \qquad 3\text{-}21$$

$T'_{cal}$, $R'_{cal}$ are the analytical expressions of $R$ and $T$ after introducing the modified Fresnel coefficients in Eqs. 3-12 and 3-13.

One critical assumption for the scalar scattering theory is $\sigma/\lambda \ll 1$ [57-59]. For the investigated CIGSe samples, the surface roughness is normally not beyond 20 nm in RMS. This indicates that $\sigma/\lambda$ is very small in the interested wavelength range. In the following, I will investigate how the MTM method influences the calculated optical constants.

To confirm whether the TMT method can improve the calculation accuracy, the smoothed samples are needed as references. Aqueous Bromine solution was proved to be able to reduce the surface roughness of CISe and CGSe [60] . In this work, Bromine was diluted in water with a concentration of 0.02 mol/L. The whole smoothening process was performed at room temperature: the samples were submerged in Bromine solution for 4 min and then rinsed with distilled water and pure ethanol, finally dried with $N_2$ for further measurements. To avoid the influence of the [Ga]/[III] variation due to the smoothing processes, CGSe and CISe instead of CIGSe are selected as exemplary samples. Fig.3.5 compares the top view of CGSe and CISe before and after smoothening. Images taken by both SEM and AFM show that the surfaces of CGSe and CISe were smoothened after the etching with Bromine solution. The surface roughness (RMS) σ was reduced from 9 nm to 3 nm for CGSe and from 20 nm to 10 nm for CISe. These smoothened samples will be used as references and to verify that the MTM method can improve the accuracy of computation of optical constants in the following.

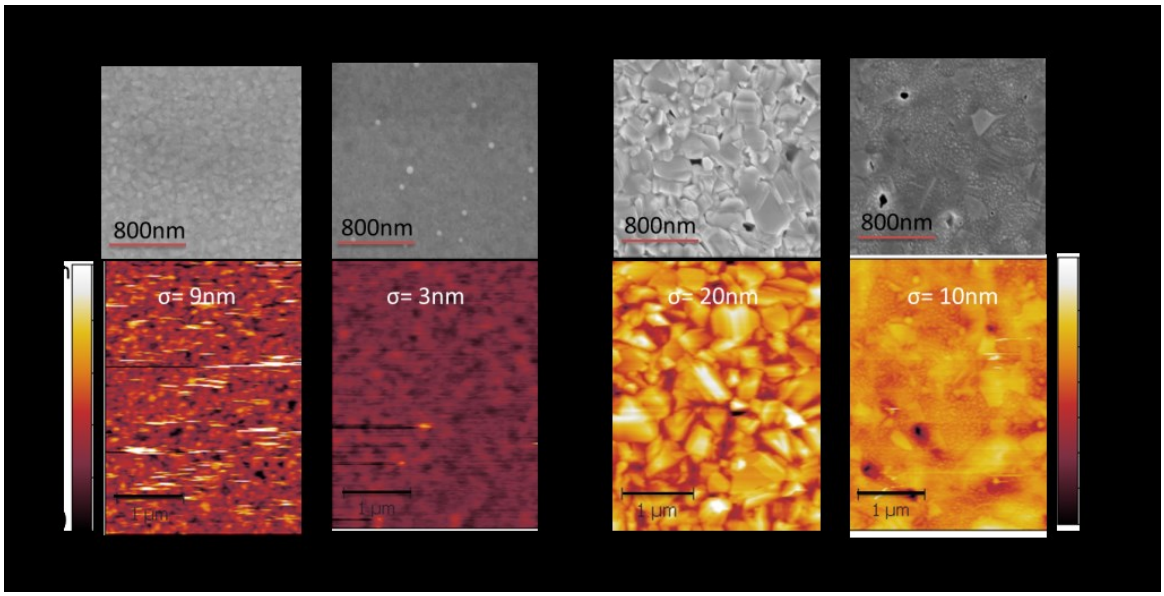


Fig.3.5: Top views of samples CGSe and CISe before and after smoothening

In Fig.3.6 (a) and (b), we can see that $R_{tot}$ of both CGSe and CISe increases pronouncedly in the short wavelength range after smoothening, especially for CISe where the absolute reduction of surface roughness is bigger. At the same time, $R_{dif}$ of CISe drops sharply after smoothening, but is still relatively large. For the sample CGSe, $R_{dif}$ is negligible compared to that of CISe due to the relatively smaller surface roughness. $R_{dif}$ stems from the surface roughness. After smoothening, the surface roughness was reduced, the scattering of light is then weakened, which is in accordance with the drop of $R_{dif}$ of CISe.

Fig.3.6 (c), (d) show the curves of multiple solutions of CGSe and CISe. It can be observed, taking the multiple $n$ solution curves of $\tilde{n}_{TM}^{Rou}$, calculated with the standard TM method for the two samples before smoothening, as examples, the branch gaps tend to widen with the wavelength decreasing. This is mainly due to the stronger scattering of light as the wavelength is decreasing, which can be confirmed from Fig.3.5. Stronger scattering indicates poorer applicability of the TM method to the experimental measured R/T. The calculated optical constants then deviate more from inherent values, branch gaps are thus bigger. This can also be verified by bigger branch gaps of $\tilde{n}_{TM}^{Rou}$ for CISe than that for CGSe due to the rougher surface and stronger scattering of CISe.

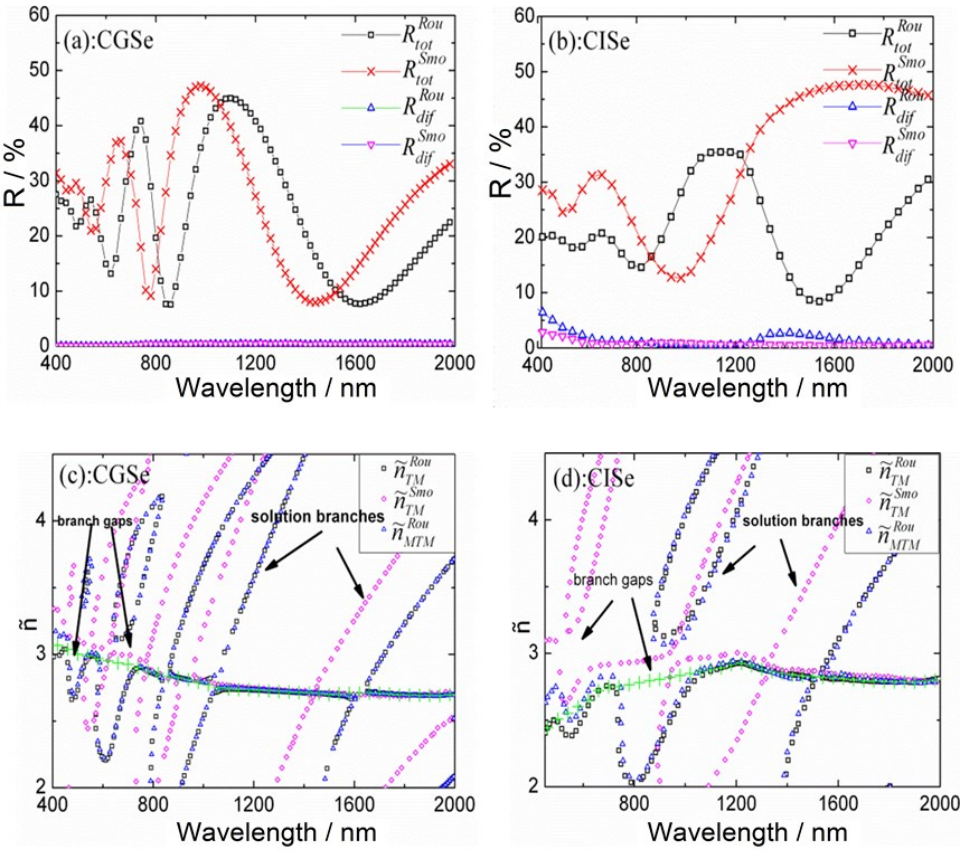


Fig.3.6: Total ($R_{tot}$) and diffuse ($R_{dif}$) reflectance of samples a) CGSe and b) CISe, multiple solutions ($\tilde{n}$) of refractive index of c) CGSe and d) CISe both before and after smoothening. Superscripts "Rou" and "Smo" correspond to that the measurement ($R$) or the calculation ($\tilde{n}$) is done for the samples before smoothening and after smoothening, respectively. $\tilde{n}_{TM}$ indicates that the multiple $n$ solutions are calculated by the TM method without considering surface roughness and $\tilde{n}_{MTM}$ that the MTM method considering surface roughness was applied. The green cross-dotted lines in Fig. 3.6 c) and 3.6 d) mark the physically meaningful values selected out of the multiple solution curves $\tilde{n}_{TM}^{Rou}$ from CGSe and CISe, respectively.

As stated theoretically above, the MTM method can compensate for the negative effect of surface roughness directly without smoothening the samples. The multiple solution $n$ curves ($\tilde{n}_{MTM}^{Rou}$), calculated by MTM method for the samples CGSe and CISe without smoothening, are illustrated in Fig.3.6 c) and d), respectively. It can be clearly observed for each sample that the continuity of the curve $\tilde{n}_{MTM}^{Rou}$ (considering roughness) also improves in contrast to $\tilde{n}_{TM}^{Rou}$ (not considering roughness): branch gaps largely narrow or even disappear. This proves that the $\sigma/\lambda$ factor in the MTM method is able to

consider the surface-roughness-induced scattering. To further confirm the effectiveness of $\sigma/\lambda$ factor in the MTM method, multiple $n$ solution curves for each smoothened sample $\tilde{n}_{TM}^{Smo}$ are needed as references and shown in Fig.3.6 c) and d). Compared to the curves $\tilde{n}_{TM}^{Smo}$ calculated by TM method on smoothened samples, the continuity of $\tilde{n}_{MTM}^{Rou}$ fails to go to the extent that $\tilde{n}_{TM}^{Smo}$ curves can reach, especially for CISe. This implies that the MTM method can only partially correct for the effect of surface roughness. To explain this point, we should go back to the assumption of $\sigma/\lambda \ll 1$. Taking CISe sample with 20 nm surface roughness as an example, $\sigma/\lambda$ in the visible range is not ideally far less than 1. When this requirement is not completely fulfilled, the MTM method will fail to fully calibrate the effect arising from surface roughness.

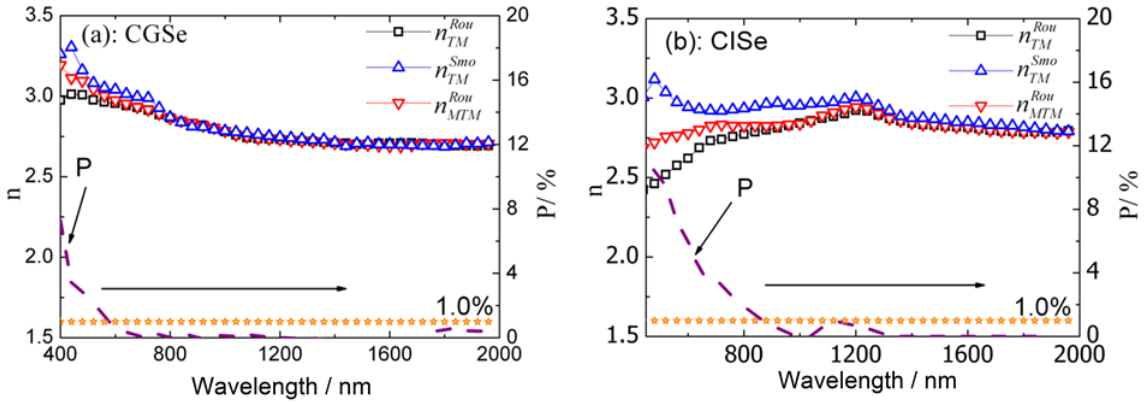


Fig.3.7: Physically meaningful $n$ data of CGSe a) and CISe b) extracted from corresponding curves in Fig.3.6 c) and d), respectively ($n_{TM}^{Rou}$ originates from $\tilde{n}_{TM}^{Rou}$ and likewise for the rest). $P$ denotes $\frac{n_{MTM}^{Rou} - n_{TM}^{Rou}}{n_{TM}^{Rou}}$. $P$, less than 1%, is regarded as the experimental error.

For quantitative illustration of the calibrating effect for $n$ values after applying the MTM method to the rough samples and the TM method to the smoothened samples compared to the application of the TM method to the rough samples, physically meaningful $n$ values from all $\tilde{n}$ curves were extracted and are shown in Fig.3.7. The extraction is according to the criterion stated in the section 3.1.2. The physically meaningful curve $n_{TM}^{Rou}$ results from the multiple solution curve $\tilde{n}_{TM}^{Rou}$ and likewise for the rest. From Fig.3.7, we can see that the curve $n_{MTM}^{Rou}$ increases in the short wavelength range and approaches $n_{TM}^{Smo}$ further compared to $n_{TM}^{Rou}$ for each sample. $P$, given as

$\frac{n_{MTM}^{Rou} - n_{TM}^{Rou}}{n_{TM}^{Rou}}$, is used to quantify the increased amplitude of the $n$ value after applying the MTM method for both samples. The increased amplitude declines gradually as the wavelength increases in both P curves. This is due to the fact that the $\sigma/\lambda$ factor in the modified Fresnel coefficients can calibrate the $R$ reduction due to surface scattering. As the wavelength decreases and/or surface roughness increases, the calibrating effect is more obvious. As it was proven both in my simulation and in literature [56], higher $R$ indicates higher $n$ value. This is why $P$ value (increased amplitude) gradually decreases as the wavelength is increasing and also $P$ value of CISe is bigger than CGSe introduced.

To illustrate the degree of improvement of $n$ values from the MTM method for both CGSe and CISe, $n_{MTM}^{Rou}$ values need to be compared to the inherent values. $\widetilde{n}_{TM}^{Smo}$ was calculated from smoothened sample and has the highest continuity among all multiple solution curves for each sample. The corresponding extracted n values ($n_{TM}^{Smo}$) are thus regarded as most comparable to the inherent values. $n_{TM}^{Smo}$ are approximately considered as the inherent values and will serve as the reference values here. We define the conformity ratio $G$ to describe the degree of improvement. $G$ denotes the average value of $\sum \frac{n_{MTM}^{Rou}}{n_{TM}^{Smo}}$ above the bandgap since the obvious difference locates mainly in this spectrum range. Obviously, a higher $G$ value implies higher conformity to the inherent values. It is calculated that the $G$ value for CGSe ($G$ = 0.979) is higher than that for CISe ($G$ = 0.954). As can be obviously seen in Fig.3.7, $n_{MTM}^{Rou}$ values for CGSe approach to the corresponding $n_{TM}^{Smo}$ values much closer than CISe, which indicates that MTM method is applicable much better for CGSe with low surface roughness than for CISe with high surface roughness. This is in accordance with the assumption of $\sigma/\lambda << 1$ stated above. CGSe is more in line with the assumption than CISe, thereby the conformity factor $G$ for CGSe is higher.

Since MTM method is proved to take the surface roughness into account and improve the calculation accuracy of optical constants of CISe and CGSe above. In the following, the optical constants of CIGSe with varied Ga/[Ⅲ] ratio (x), with considering surface roughness, are summarized and presented in Fig.3.8.

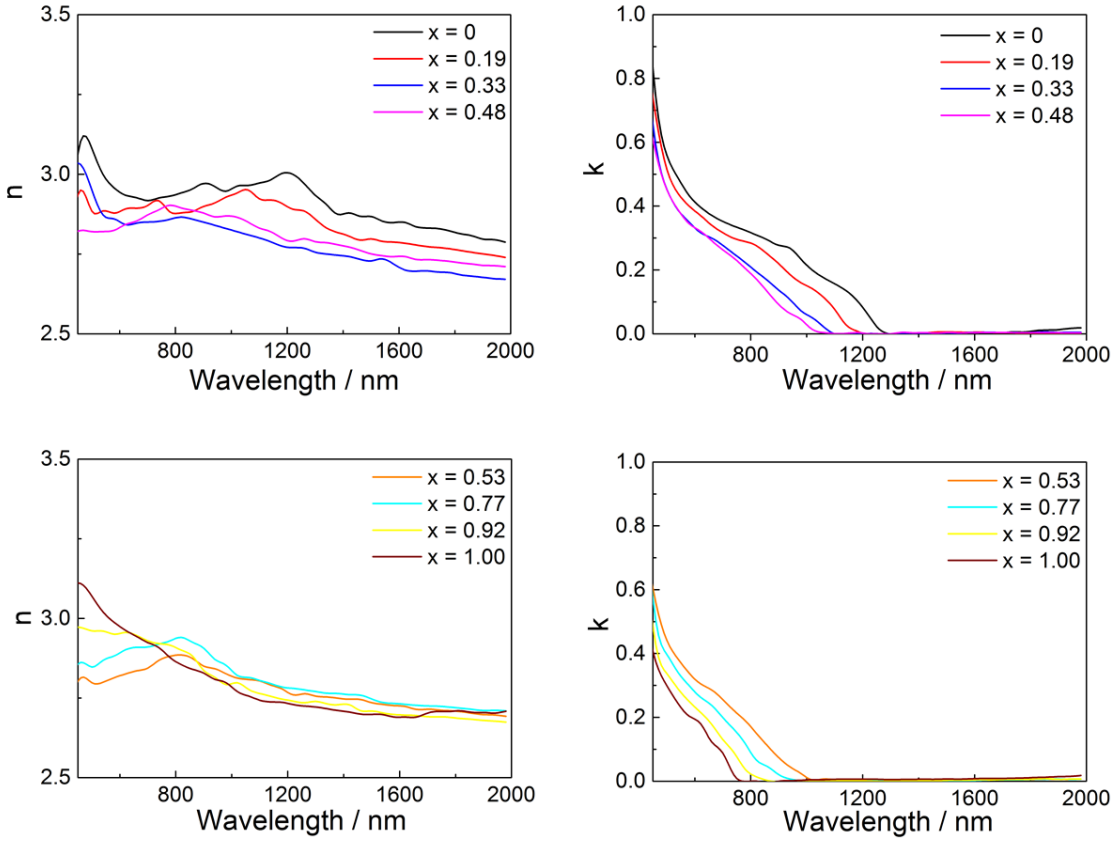


Fig.3.8 Optical constants of CIGSe layer with varied [Ga]/[III] ratios (x) taking the surface roughness into account

The calculated optical constants of CIGSe layers with varied [Ga]/[III] ratios can form a database, which can be used for general optoelectronic simulations of CIGSe solar cells. Regarding the change in trend of optical constants with [Ga]/[III] ratio, this is beyond the scope of this thesis and will not be discussed here. The optical constants with arbitrary [Ga]/[III] ratio can be interpolated from the data of neighbouring [Ga]/[III] ratios since the [Ga]/[III] (x) points are dense enough . The database can be accessed from Appendix B or from the author.

## 3.2.2 Influence of substrate temperature

In the calculation above, CIGSe samples were deposited at the maximum temperature ($T_s$ = 610 °C) the glass substrate could bear. CIGSe layers deposited at low temperature are a focus in my work because the low substrate temperature not only enhances the $J_{sc}$ of bare ultra-thin solar cells, but also favours the thermal stability of light-trapping structures. Further, the low substrate temperature is also a general trend since it enables

to make the CIGSe deposition possible on flexible polymer substrate as well as a better performance on TCO back contact [30, 39, 61]. The substrate temperature, being a key deposition parameter, can affect the growth and the resulting properties of materials. It is hence necessary and meaningful to investigate the influence of substrate temperature on the optical constants of CIGSe layers. The samples grown at 610 °C were already investigated above. For comparison, the low substrate temperature is set at 440 °C. This is the lowest temperature at which well-performed solar cells can be obtained in my work. To make the investigated samples representative for illustrating the influence of substrate temperature on the optical constant, CISe (x = 0.0), CGSe (x = 1.0) and CIGSe (x = 0.4) were selected. For CISe (x = 0.0) and CGSe (x = 1.0), there is no [Ga]/[III] depth distribution inhomogeneity. However, CISe (x = 0.0) couldn't form the chalcopyrite structure at 440 °C, so CGSe (x = 1.0), as a sample without considering the influence of [Ga]/[III] depth distribution, is investigated. CIGSe (x = 0.4) contains both elements of Ga and In, the influence of [Ga]/[III] depth distribution needs to be taken into account for optical constants. The [Ga]/[III] ratio of 0.4 is selected due to the fact that the solar cells at this [Ga]/[III] ratio perform quite well. The samples with each [Ga]/[III] ratio were preapred on glass substrate at both temperatures of 610 °C and 440 °C as described in section 2.2.

***Results and discussion***

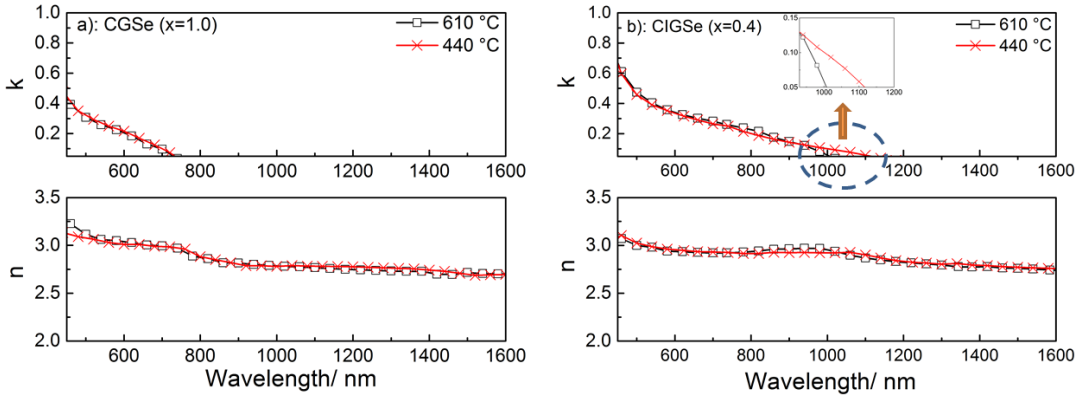


Fig.3.9 Calculated optical constants of a) CGSe and b) CIGSe (x = 0.4) at two substrate temperatures of 610 °C and 440 °C

Fig.3.9 compares the optical constants of CIGSe (x = 0.4) and CGSe (x = 1.0) at two substrate temperatures of 610 °C and 440 °C on glass substrate. For CGSe both the refractive index *n* and the extinction coefficient *k* remain almost the same. This may be

reflected by the similar morphologies shown in Fig.3.10: both CGSe (x = 1.0) layers are composed of closely-packed small grains. However, the cross sections of the CIGSe (x = 0.4) layers in Fig.3.10 (b) differ in grain size: at the low substrate temperature (440 °C), the CIGSe (x = 0.4) layer exhibits much smaller grains compared to that at high temperature (610 °C). However, the grains for both temperatures are closely packed and it is the compactness of the films, which is believed to impact the refractive index values. This can possibly explain the observed fact of the relatively stable refractive indexes for the two CIGSe (x = 0.4) films. However, the extinction coefficients *k* exhibit differences. The *k* values are comparable in the wavelength range of 450-900 nm for both CIGSe (x = 0.4) layers, while the *k* values corresponding to a substrate temperature of 440 °C are higher than those corresponding to 610 °C above the wavelength of 900 nm and show absorption in a broader wavelength range. This is related to the changed Ga/[Ш] depth profile of the CIGSe (x = 0.4) layer at different substrate temperatures. GDOES results in Fig.2.7 already confirmed that the CIGSe absorber at $T_s$ = 440 °C has a lower minimum Ga/[Ш] phase and much more lower Ga/[Ш] phases due to the less inter-diffusion of Ga-In. The bandgap is linearly dependent on the Ga/[Ш] ratio, the CIGSe layer at 440 °C has a lower minimum bandgap and thus a broader absorption wavelength range. Furthermore, lower Ga/[Ш] phases have higher absorption ability, this explains why the absorption ability (*k*) for the CIGSe (x = 0.4) at 440 °C is higher in long wavelength range (> 900 nm).

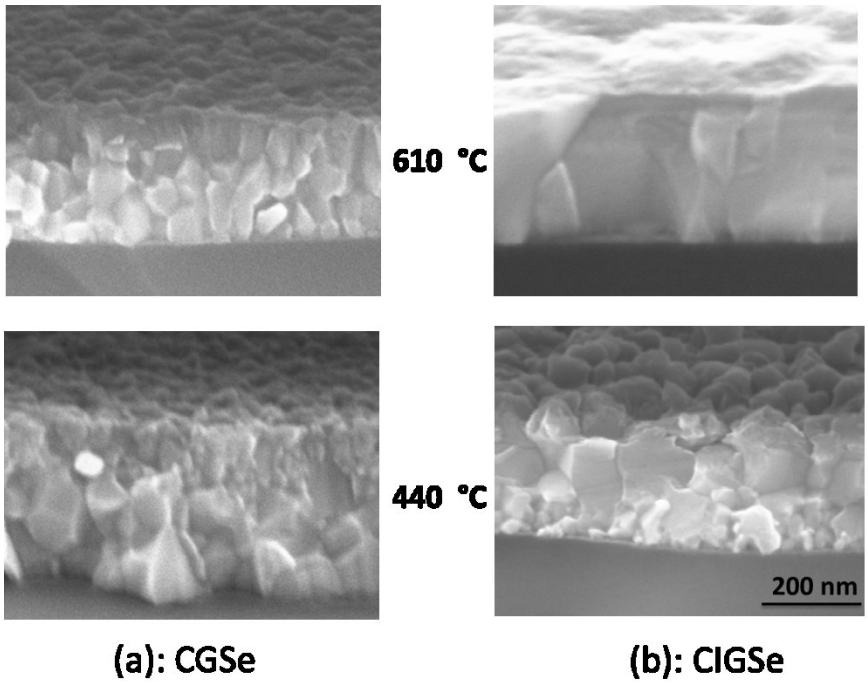


Fig.3.10. SEM cross sections of a) CIGSe and b) CGSe at two substrate temperatures of 610 °C and 440 °C on glass substrate

## 3.3 Optical constants of CdS, ZnO, AZO and Mo layers

These 3 layers (CdS, ZnO, AZO) in this work are quite smooth, the surface roughness consideration is not necessary. The optical constants are similarly investigated as for CIGSe samples and are presented in Fig.3.11. However, for Mo, its optical constants are evaluated via of ellipsometry method (one belongs to the polarimetric). The TM method couldn't deal with the Mo layer because there is no transmission for the 800 nm thick Mo layer due to its high absorption ability. This disobeys the requirement of $T > 0$ for TM method. The details of ellipsometry method can be found in literature [47], but it is not the focus of this thesis and will not be discussed here.

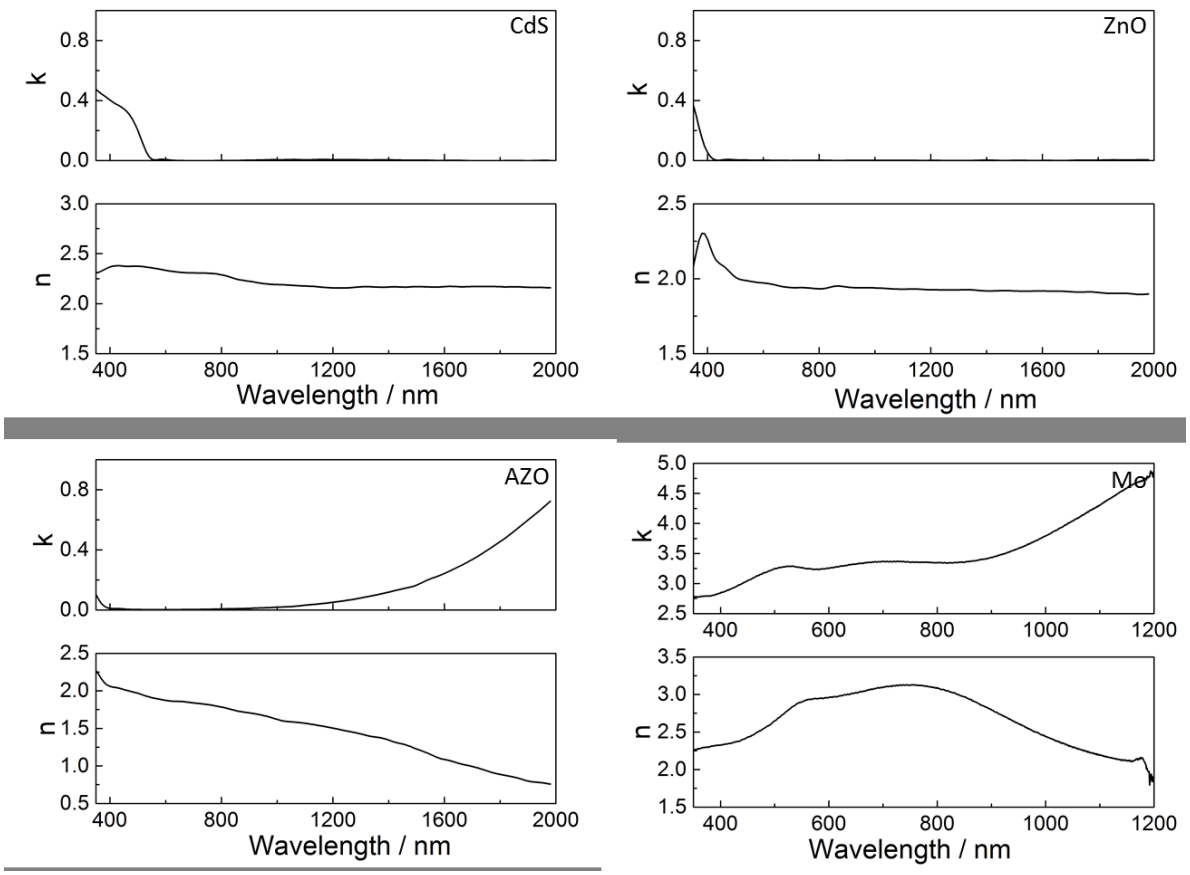


Fig.3.11 Optical constants of practical CdS, ZnO, AZO and Mo thin films on glass substrates

## 3.4 Conclusion

In this chapter, the optical constants of each layer in solar cells (AZO, ZnO, CdS, CIGSe and Mo) are investigated with a special focus on CIGSe layers due to its importance. Transfer-Matrix (TM) method is employed as the main method for its simplicity and the same illumination geometry as the corresponding solar cells. The novelty is that the surface roughness is taken into account in the TM method (in terms of MTM method) and results in accurate optical constants of CIGSe films. An optical constant database of CIGSe layers grown at high temperature with varied Ga/[III] ratios is established and available for theoretical simulations. Moreover, the optical constants of CGSe (x = 0) and CIGSe (x = 0.4) grown at both high temperature (610 °C) and low temperature (440 °C) are compared. It is found the refractive indexes *n* of both CGSe (x = 0) and CIGSe (x = 0.4) stay relatively stable. However, for CIGSe (x = 0.4), the extinction coefficients *k* exhibit differences, which is higher at 440 °C than 610 °C in the wavelength range of 900–1200 nm. The less inter-diffusion of In-Ga at 440 °C is

proved to contribute to this. It is implied that the optical constants can be altered due to different Ga/[III] profiles.

Finally, it should be mentioned that the possible error for the application of the obtained optical constants. The experimental sample structure for evaluating the optical constants is a simple stack of a thin layer on glass substrate. But the real device is deposited layer by layer sequentially instead of on a glass substrate. The substrate materials and deposition of layers on top can possibly inter-alter the properties of films. For example, CIGSe is mostly deposited on Mo instead of glass substrate and the deposition of the window layer can possibly influence it. This is however not considered in my case. The reasons are as follows: AZO/ZnO/CdS are prepared at a low substrate temperature below 200 °C, I don't expect a non-negligible inter-influence for these layers. More importantly, comparing the simulated *Abs* in CIGSe layer using the obtained optical constants to the EQE of the corresponding solar cells, they match quite reasonably. It is therefore assumed that the optical constants extracted from the sample on glass substrate are reliable and can be applied for optical simulations of solar cell devices in my work.

# Chapter 4

# Identification of optical losses in ultra-thin $CuIn_{1-x}Ga_xSe_2$ solar cells and implication for light-trapping structures

## 4.1 Identification of optical loss

To choose appropriate light-trapping structures, the priority is to identify where and how much of the optical loss for ultra-thin CIGSe solar cells. Amongst all the layers in the CIGSe solar cell devices, only the absorption in CIGSe absorber layer ($Abs_{CIGSe}$) can contribute to the photocurrent [62], reflection ($R$) and absorption in the other layers are dissipated. The ultimate goal of light trapping is thereby to enhance $Abs_{CIGSe}$ by minimizing $R$ and parasitic absorption in the other layers.

Table 4.1 Structures of the investigated CIGSe solar cells

| No. | Structure (from top to bottom) | Thickness of CIGSe (nm) |
|---|---|---|
| **S1** | AZO/ZnO/CdS/CIGSe/**Mo**/glass substrate | 2000 |
| **S2** | AZO/ZnO/CdS/CIGSe/**Mo**/glass substrate | 300 |
| **S3** | AZO/ZnO/CdS/CIGSe/**Ag**/glass substrate | 300 |
| **S4** | AZO/ZnO/CdS/CIGSe/**ITO**/glass substrate/**Ag back reflector** | 300 |

I employed TM method inversely to calculate the optical responses (*R/Abs*) of the solar cell device. The optical constants of CIGSe layer are extracted from a sample prepared at substrate temperature of 440 °C with Ga/[III] of 0.35. For the window and buffer layers (AZO/ZnO/CdS), the thicknesses are the same as in Fig.2.2 (240/130/50/200 nm) and the corresponding optical constants are taken from chapter 3.3. The back contact has a thickness of 200 nm. The integrated current density of each optical response (*Abs/R*) is calculated assuming the complete conversion under standard AM 1.5

irradiation. Table 4.1 lists the structure information of investigated solar cells as follows.

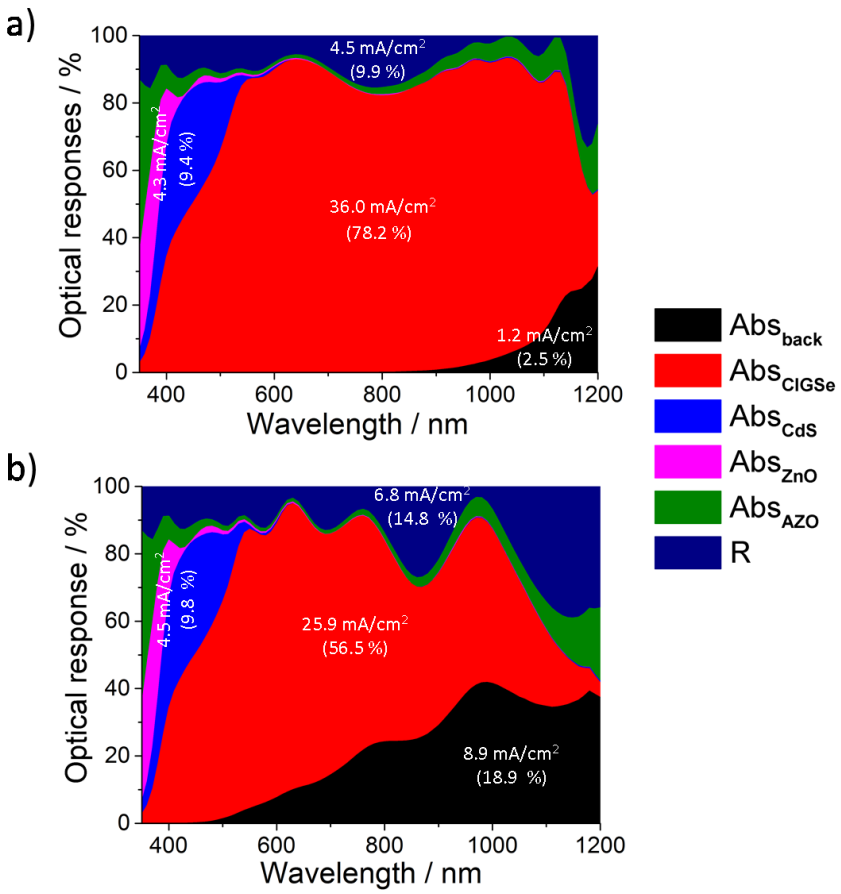


Fig.4.1 The optical responses (*R/Abs*) of the cell device (AZO/ZnO/CdS/CIGSe/Mo) with a CIGSe thickness of a) 2000 nm (S1) b) 300 nm (S2)

Fig.4.1 compares the optical responses (*R/Abs*) of solar cells on Mo back contact with a CIGSe thickness a) 2000 (S1) and b) 300 nm (S2). I start with solar cells with Mo back contact, because Mo is mostly used for achieving good solar cells. The optical losses are sub-divided into 3 parts: R, the parasitic *Abs* in AZO/ZnO/CdS ($Abs_{AZO/ZnO/CdS}$) and back contact ($Abs_{back}$). R loss covers the whole interested spectrum. The parasitic $Abs_{AZO/ZnO/CdS}$ dominates the absorption in the visible range (350-550 nm) due to the band-to-band absorption. This absorption mainly occurs before light reaches the CIGSe layer. We can also observe $Abs_{AZO/ZnO/CdS}$ beyond 550 nm, this is related to the free charge carrier absorption of AZO. The parasitic $Abs_{back}$ starts from the wavelength where light is not completely absorbed by the CIGSe absorber. The photocurrent density corresponding to the complete conversion of AM 1.5 incident spectrum is

constant (46.04 mA/cm$^2$). Compared to the solar cell device with a 2000-nm-thick CIGSe absorber (Fig.4.1 a)), the cell with a 300 nm (Fig.4.1 b)) exhibits much lower $Abs_{CIGSe}$ ascribed to CIGSe thickness reduction and the absorption reduction mainly lies in the infrared range. The photocurrent density from $Abs_{CIGSe}$ accounts for 78.2% for the 2000-nm-thick-absorber cell and drops to 56.5% when the CIGSe thickness is 300 nm thick. Meanwhile, $R$ and parasitic $Abs_{back}$ increase from 9.9% to 14.8% and from 2.5% to 18.9%, respectively. $Abs_{AZO/ZnO/CdS}$ keeps relatively stable. It can be concluded that the $Abs_{CIGSe}$ loss due to thickness reduction is dissipated both by the increased $R$ and the parasitic $Abs_{back.}$ This increase is especially serious for $Abs_{back}$. This can be interpreted by the poor reflectivity ability of Mo: light will be dominantly absorbed rather than reflected. It was reported that the reflection at the Mo/CIGSe interface was below than 20% [63]. As the CIGSe thickness reduces, the intensity of light hitting on the Mo layer increases, indicating more parasitic absorption by Mo. It implies the high necessity to replace Mo by other alternative materials with better reflectivity. To confirm the implication, Ag is used to replace Mo due to its better reflectivity. Fig.4.2 a) depicts the corresponding optical responses for the 300-nm-thick-CIGSe solar cell with Ag back contact (S3). The parasitic $Abs_{back}$ greatly reduces and only accounts for 0.9 %. Due to its high reflectivity of Ag, unabsorbed light after passing through CIGSe layer will be dominantly reflected back into CIGSe absorber. As a result, the portion that $Abs_{CIGSe}$ takes enhances from 56.5% to 65.3 % compared to the solar cell on Mo back contact. Besides, $R$ follows the similar trend, increasing from 14.8% to 23.5%. The increase in $R$ mainly lies in the long wavelength range, due to the poor absorption ability of solar cells. Unfortunately, the implementation of Ag and other metallic materials like Al, Au having better reflectivity is not experimentally feasible due to their poor thermal stability. An alternative back contact material, which is experimentally stable, is the transparent back contact ITO. It also has poor reflectivity, which can however be overcome by placing a back reflector (like Ag) at the rear side of glass substrate. The optical responses (S4) are shown in Fig.4.2 b). $Abs_{CIGSe}$ increases by 6.8% compared to that of the corresponding cell on Mo. The parasitic $Abs_{back}$ (both ITO and Ag back reflector) takes a portion of 5.9 %, which mainly stems from ITO. $Abs_{back}$ in ITO plus Ag back reflector is stronger than that in pure Ag back contact in Fig.4.2 (a) but greatly lower than that in Mo back contact in Fig.4.1 b). Therefore, the back contact of ITO plus a back reflector is favourable for ultra-thin CIGSe solar cells. Nevertheless, even with Ag back contact, $Abs_{CIGSe}$ for ultra-thin CIGSe cells is still below that for their

thick counterparts, further light-trapping technologies are therefore indispensable for highly efficient ultra-thin solar cells.

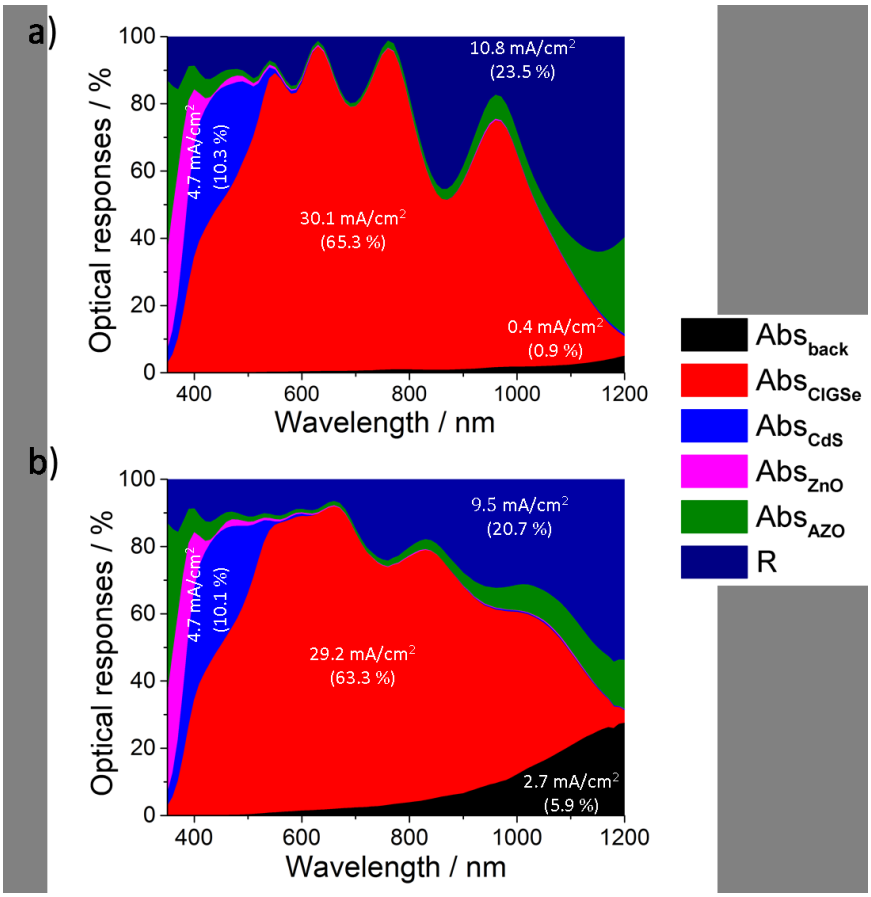


Fig.4.2 The optical responses (*R/Abs*) of 300-nm-thick-CIGSe cell with a) Ag back contact (S3) b) ITO back contact plus a Ag back reflector (S4)

## 4.2 Approaches of light absorption enhancement

**Optimization of AZO/ZnO/CdS layers**

To enable the effective absorption in the CIGSe layer, light must pass through AZO/ZnO/CdS layers, which indicates that $Abs_{AZO/ZnO/CdS}$ is inevitable. Replacing CdS by a larger bandgap material like Zn(O,S) [36] can reduce the parasitic absorption. Besides, reducing the net thickness of AZO/ZnO/CdS layers can also decrease the parasitic $Abs_{AZO/ZnO/CdS}$. Since CdS favours the electrical properties of solar cells and the thicknesses of AZO/ZnO/CdS layers are already optimized for electrical consideration, these two optimization points are however not discussed in this work. The focus of light trapping is mainly to reduce *R* and the parasitic $Abs_{back}$, thus to improve $Abs_{CIGSe}$.

Conventionally, light-trapping schemes work by preferentially scattering, which can incouple more light propagating longer path in the cells. This effect can be decomposed into two effects: Anti reflection and larger angular scattering. In the following, these two effects will be theoretically analyzed for the ultra-thin CIGSe solar cells from the top.

**Anti-reflection effect**

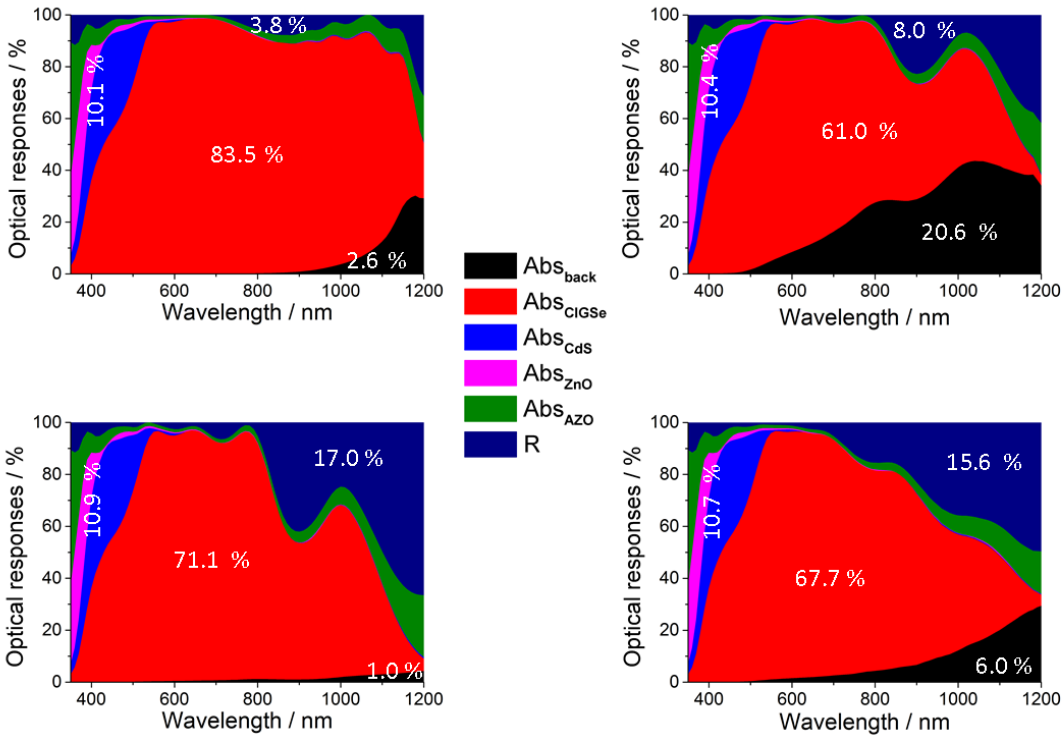


Fig.4.3 The corresponding optical responses (*R/Abs*) of the solar cell structures in Table 4.1 with a 110 nm thick anti-reflection layer of $n$ = 1.3

Fig.4.3 shows optical responses (*R/Abs*) of the 4 solar cell structures described in table 4.1 plus an anti-reflection layer ($n$ = 1.3) with an optimized thickness of 110 nm. For all 4 structures, it is seen that R is reduced after coating the anti-reflection layer over the whole spectrum range. The reduction of R ($\Delta R$) is gained by $Abs_{CIGSe}$, $Abs_{back}$ and $Abs_{AZO/ZnO/CdS}$. Fig.4.4 quantitatively calculates the gain portion of the absorption in back contact, CIGSe, AZO/ZnO/CdS from R reduction with the anti-reflection layer. For thick solar cell (S1), $Abs_{CIGSe}$ enhancement ($\Delta Abs_{CIGSe}$) takes the main benefit of $\Delta R$, accounting for 86.5% of $\Delta R$. The gain of parasitic $Abs_{back}$ due to $\Delta R$, $\frac{\Delta Abs_{back}}{\Delta R}$, is only 2.1%. While the gain of $Abs_{CIGSe}$ from $\Delta R$, $\frac{\Delta \mathrm{Abs_{CIGSe}}}{\Delta \mathrm{R}}$, drops to 69.9% and $\frac{\Delta Abs_{back}}{\Delta R}$

increases sharply to 19.6% for the 300-nm-thick-CIGSe cell on Mo (S2). This indicates that $Abs_{CIGSe}$ benefits less from $R$ reduction as the CIGSe thickness decreases. With Ag back contact or ITO back contact plus Ag back reflector, $\frac{\Delta Abs_{CIGSe}}{\Delta R}$ is much greater than the cell with Mo back contact and $\frac{\Delta Abs_{back}}{\Delta R}$ is negligible.

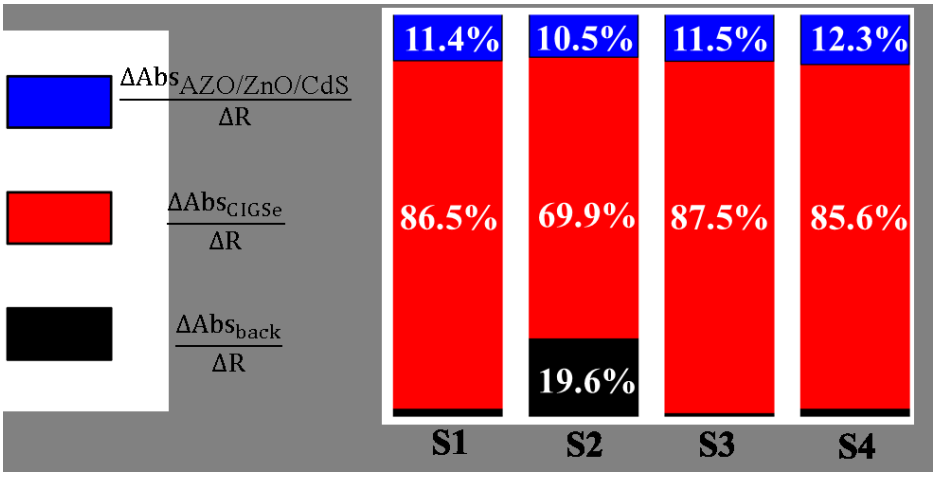


Fig.4.4 Comparison of the gain portions of the absorption in back contact, CIGSe, AZO/ZnO/CdS from $R$ reduction arising from the 110 nm thick anti-reflection layer

**Large angular scattering**

As implied above, Mo back contact is the main impeding factor for the improvement of $Abs_{CIGSe}$. To achieve a better anti-reflection effect for ultra-thin solar cells, one approach is to scatter light with large angles. This can length the propagating path in the CIGSe layer and $Abs_{CIGSe}$ is thus enhanced. Consequently, light intensity hitting on Mo is thus reduced and $Abs_{back}$ is minimized. However, we should keep in mind: there are 3 layers (AZO/ZnO/CdS) on top of the CIGSe layer, all these 3 layers have parasitic absorption, light scattering from the top of solar cells will firstly length the propagating distance through the AZO/ZnO/CdS layers and thereby the parasitic $Abs_{AZO/ZnO/CdS}$ is increased. This possibly reduces the light intensity through the CIGSe layer and worsens $Abs_{CIGSe}$.

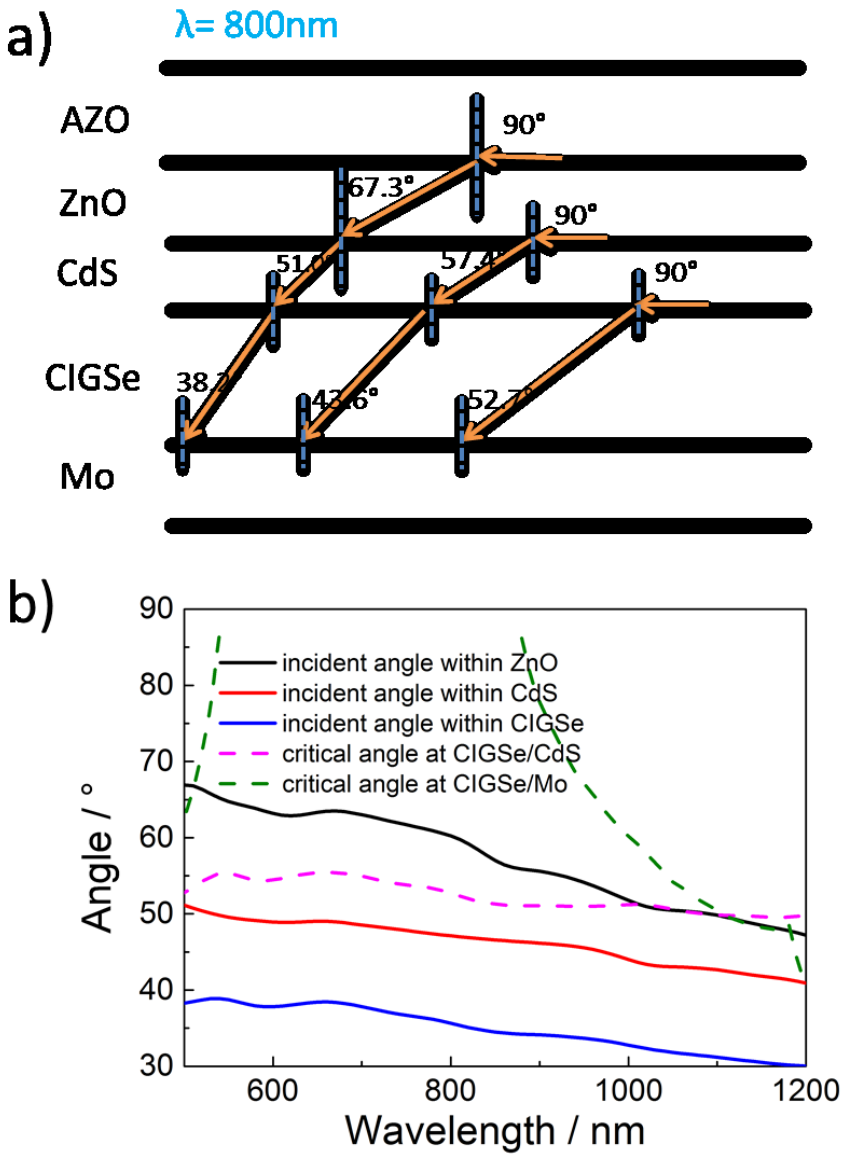


Fig.4.5 a) Illustration of the propagating angle in the solar cell for the wavelength λ = 800 nm with an initial angle of 90° within AZO, ZnO and CdS; b) The propagating angles in each layer of a CIGSe solar cell with an initial angle of 70° in the AZO layer and the critical angles at interfaces of CIGSe/CdS and CIGSe/Mo

Besides, the scattered angles will be largely narrowed due to the continuously increasing refractive indexes from AZO to CIGSe and the increase of effective propagating length in CIGSe is restraint. Fig.4.5 a) illustrates an example (λ = 800 nm) of the propagating angles in each layer with a maximum angle of 90° by Snell law. Starting from AZO, ZnO, CdS corresponds to the locations of light-trapping structures at the interfaces of Air/AZO, AZO/ZnO, ZnO/CdS. The further the initial scattering location from the CIGSe layer, the narrower the scattering angles will be in the CIGSe

layer. Since most light-trapping structures are located on the top surface, Fig.4.5 b) shows the changing trend of scattering angles over the whole wavelength range with an initial incident angle of 70° within the AZO layer. This 70° incident angle is for the maximum scattering angle of a dipole can scatter at the interface of Air/AZO. We can see the scattering angles gradually narrowing to around 30°. Regarding the desired planar wave-guided modes, intending to trap the light within the CIGSe layer, total reflection is one precondition. The critical angles of total reflection at CIGSe/CdS and CIGSe/Mo interfaces are also calculated and shown in Fig.4.5 b). The propagating angles in the CIGSe layer are much smaller than the critical angles at the interfaces of CIGSe/CdS and CIGSe/Mo. This means that the wave-guided modes barely occur at this case of placing light-trapping structures on the surface. To achieve the wave-guided modes, light trapping structures are needed to be located at the interfaces of CdS/CIGSe and CIGSe/Mo and the scattering angles can thus be maintained. Conclusively, the benefit of large incident angles from the top can be weakened by the increased parasitic $Abs_{AZO/ZnO/CdS}$ as well as the narrowed propagating angles. Therefore, the light-trapping structures on the surface of ultra-thin CIGSe cells should be carefully designed to obtain the increase of $Abs_{CIGSe}$. From the optical point of view, light-trapping structures at the interfaces touching the CIGSe layer are promising.

**Light-trapping mechanisms**

Recently, numerous innovative light-trapping structures in nanoscale [16-23] are emerging and have shown the potential to better enhance the absorption of photoactive layers in solar cells. In principle, the absorption enhancement mechanisms can be sorted to:

1) Anti-reflection [21, 64] or back reflecting [23, 65]: nanostructures can preferentially scatter light into the solar cells. The reflection can be suppressed if the nanostructures are placed on the surface of solar cells, or the unabsorbed light can be in-coupled back into solar cell if the nanostructures are located at the rear side. These are similar to conventional anti-reflection or back reflecting effects.
2) Large angular scattering [19, 22, 65]: light is scattered into high angular range by nanostructures with respect to the incident angle and propagating length of light in the photoactive layers is thus beyond the physical thickness. It is like the conventional interface texturing but shows the potential to be more efficient.

3) Near field enhancement [19]: light induces the movement of electrons around nanoparticles, which can locally concentrate the energy of light in the vicinity in the form of strong near field. Its energy can be locally absorbed by the surrounding absorbing media and absorption enhancement can be achieved.
4) Leaky mode [66, 67]: dielectric particles can confine the incident light around the particles and form strong near field due to specific resonance modes. The energy of near field can leak into the adjacent photoactive layers (leaky mode).

Among them, light-trapping mechanisms 3 and 4 belong to the discussion of wave optics and are not discussed in this chapter. In practice, one innovative light-trapping structure often contains more than one enhancement mechanism. Besides, the working wavelength range can be selective by tuning the geometries and materials of light-trapping structures in nanoscale. Regarding the location in solar cells, light-trapping structures are mostly placed on the top and at the rear surface for the consideration of the electrical stability of solar cells. However, if the mechanism 1 and 2 are utilized on the surface, light-trapping effects will be largely discounted for ultra-thin CIGSe solar cells from our analysis above. This indicates to place the nanoparticles as closely as possible to the CIGSe photoactive layer. Additionally, it can enable the solar cells to better utilize the enhancement mechanism 3) near field enhancement, which requires to place the light-trapping structures touching or within the CIGSe absorber. It should be stressed here, if placing the light-trapping structures at the interfaces of CdS/CIGSe and CIGSe/back contact, electrical properties at the interfaces should be carefully considered. In view of the critical p-n junction interface of CdS/CIGSe, the location selection is favoured at CIGSe/back contact.

Following chapters are related to the application of light-trapping structures on CIGSe solar cells, chapter 5 focuses on the metallic nanoparticles (Ag) locating underneath the transparent back contact (ITO) layer, mechanisms 1 and 2 will be of interest; chapter 6 investigates the 2-D closely packed $SiO_2$ nanosphere arrays on the top of cells, mechanism 1 and 4 are mainly used; Chapter 7 places the $SiO_2$ dielectric nanostructures at the interface of CIGSe/Mo and the main light-trapping effect is mechanism 2.

# Chapter 5

# Light trapping by plasmonic Ag nanoparticles in ultra-thin $CuIn_{1-x}Ga_xSe_2$ solar cells

Among the conventional light-trapping technologies for solar cells, texturing the interfaces [68, 69], depositing an anti-reflection layer [70] and a rear reflector [71, 72] (Ag, white paste) are typically applied. Texturing the interfaces can scatter light into a large angular range and thereby increases the effective propagating length of light beyond the physical thickness of cells. However, textured interfaces increase the interface area as well, which possibly leads to a high carrier recombination. This case is assumed to be possibly more serious for the heterogeneous thin-film CIGSe solar cells and is thereby seldom applied compared to Si solar cells. Besides, as analyzed in the last chapter, texturing the surface may largely increase the parasitic $Abs_{AZO/ZnO/CdS.}$ The anti-reflection effect is normally realized by coating a thin $MgF_2$ layer with an approx. 110 nm thickness, which however fails to achieve a comparable photocurrent density to that of thick CIGSe solar cells as shown in Fig 4.3. A rear back reflector can scatter back the unabsorbed light into the cells again. This approach requires a transparent back contact or to transfer the cell stack from the typical Mo back contact to other metallic materials having a better reflectivity [7]. The transferring process has been successfully reported but the lifting-off process was quite complicated and the transferring area of solar cells was limited in the scale of few centimeters [73]. In the past few years, metallic nanoparticles have attracted tremendous attentions in the application of absorption enhancement for solar cells due to their unique plasmonic properties [16, 18, 69, 74, 75]. It has been theoretically demonstrated that the absorption enhancement factor of metallic nanoparticles can exceed the classic value of $4n^2$, which is the limit of the conventional textured interfaces ($n$ is the refractive index of the medium surrounding the nanoparticles) [76]. This implies the potential of a better absorption enhancement using metallic nanoparticles as light-trapping elements.

Metallic nanoparticles in a sub-wavelength size can support the localized surface plasmon (resonant modes) arising from the collective oscillation of electrons under illumination. These plasmonic nanoparticles interact with light strongly in the resonance

wavelength range. To be specific, the corresponding absorption enhancement mechanisms for solar cells behind the localized plasmon can be generally classified into [19]: plasmonic scattering and near-field concentration. For the plasmonic scattering, the scattering angular range can be broader than the conventional light-trapping technologies and exceed the critical angle of reflection at two media [77] and thus trap the light in the cells; further, light can be preferentially scattered into the medium with a higher refractive index when metallic nanoparticles are placed at the interfaces of two media [78], which is similar to the anti-reflection or back-reflecting effect. The metallic nanoparticles in the resonance of localized plasmon can also form the strong local electrical field (referring to near field) around themselves especially for particles in small size. They can localize the light energy around the particles and serve as an "antenna" [79]. The decaying time of the induced near field is in 10-50 fs, it is therefore required that the absorption rate of the surrounding media is faster than the decaying time and the plasmonic nanoparticles are placed as closely as possible to the photoactive layers in the cells, otherwise the energy stored in the strong near field will dissipate in terms of ohmic damping [19].

The optical responses of metallic nanoparticles depend on the material itself, particle size, shape, surface coverage, adjacent medium and etc. [77, 80, 81]. The light-trapping concepts of metallic nanoparticles have been intensively demonstrated both experimentally and theoretically in the Si-based [65, 74] , GaAs [82] and organic solar cells [83, 84]. For CIGSe solar cells, the structures and preparation conditions differ a lot from the cells of other types. Whether the metallic nanoparticles can be successfully applied in CIGSe solar cells or not has not been verified yet. To my best knowledge, few reported the plasmonic application of the metallic nanoparticles in the CIGSe solar cells. Therefore, it is quite meaningful to demonstrate the plasmonic light-trapping effect of metallic nanoparticles in the CIGSe solar cells.

## 5.1 Plasmonic behavior of metallic nanoparticles and application to CIGSe solar cells

### 5.1.1 Introduction to particle plasmons

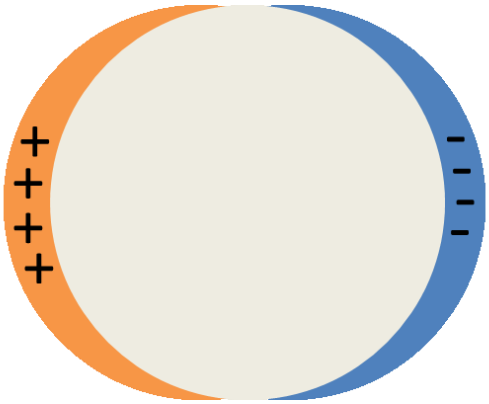

Fig.5.1 An illustration of movement of electrons of metallic particles under an external electric field

As Fig.5.1 shows, when a metallic particle is subject to an external electric field (eg, electromagnetic wave), the conduction electrons are driven to the opposite direction to the electric field. Consequently, a restoring force forms and a dipole is induced in terms of a net negative charge and a net positive charge accumulating on each side of the particle. Under the illumination of electromagnetic waves, the time-varying electric field allows for the occurrence of a resonant condition (collective oscillation of free electrons). The oscillation of electrons in such a nanoparticle is referred to a localized surface plasmon resonance (LSPR).

A key parameter to characterize the resonance behavior is the polarizability (α), which is expressed by Clausius-Mossotti equation for a spherical particle in the electrostatic limit [85]. This parameter is to describe the distortion extent of the free electrons around the particles by an external electric field.

$$\alpha = 4\pi r^3 \frac{\varepsilon - \varepsilon_d}{\varepsilon + 2\varepsilon_d} \qquad 5\text{-}1$$

where r is the particles radius, $\varepsilon_d$ the dielectric function of surrounding media, $\varepsilon$ $(= n^2 - k^2 + 2nki)$ the complex dielectric function of metal.

We can observe that the particle polarizability can reach the maximum when $\varepsilon = -2\varepsilon_d$, which corresponds to the resonance behavior of LSPR. At resonances, the oscillating dipole can re-radiate (in terms of scattering) and absorb the incident light. Scattered light has the same frequency as the incident. To describe the scattering and absorption ability, scattering ($C_{sca}$) and absorption, $C_{abs}$ cross-sections are defined to quantify how much of the incident light is scattered and absorbed [80], respectively. Using Mie

theory, the mathematical $C_{sca}$ and absorption $C_{abs}$ of a single sphere particle can be given and the extinction cross section ($C_{ext}$) is defined as the sum of the $C_{sca}$ and $C_{abs}$.

$$C_{sca} = \frac{1}{6\pi}(\frac{2\pi}{\lambda})^4|\alpha|^2 \quad \propto r^6 \qquad 5\text{-}2$$

$$C_{abs} = \frac{2\pi}{\lambda} IM[\alpha] \qquad \propto r^3 \qquad 5\text{-}3$$

$$C_{ext} = C_{abs} + C_{sca} \qquad 5\text{-}4$$

Where, λ is the incident wavelength.

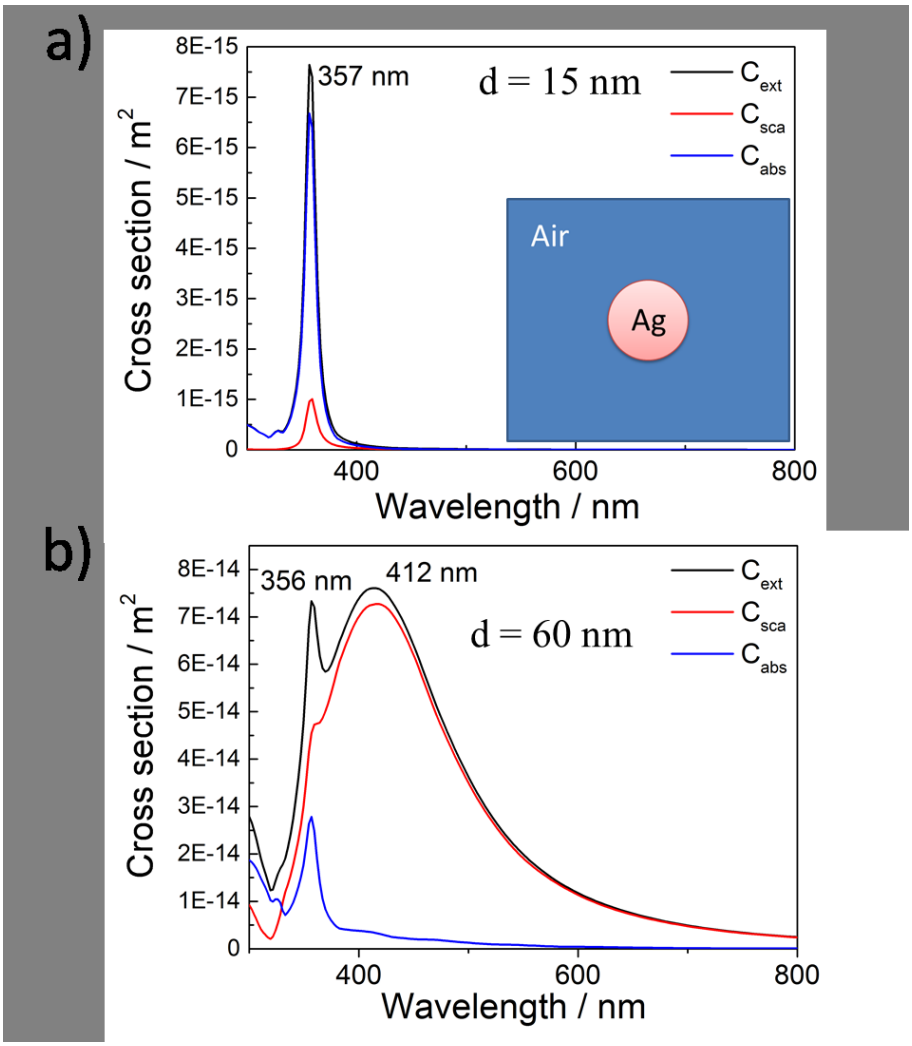


Fig.5.2 Cross sections ($C_{sca}$, $C_{abs}$, $C_{ext}$) of a Ag sphere in air for the diameter of a) $d$ = 15 nm and b) $d$ = 60 nm

For larger particles comparable to the wavelength, the electrostatic assumption is not completely valid. There is a phase retardation of the collective electrons across the particles, which results in a weakened restoring force and hence a red-shift of the dipolar resonance and the appearance of higher order modes [85]. To confirm this, the

cross sections ($C_{sca}$, $C_{abs}$, $C_{ext}$) of a Ag nanosphere in air are calculated for diameter ($d$) of 15 nm and 60 nm using Mie theory. The calculations are depicted in Fig.5.2. The dipole resonance shifts from λ = 357 nm to λ = 412 nm and simultaneously the quadrupole appears at λ = 356 nm when the diameter increases to 60 nm. Besides, for the case of the Ag nanopshere with a diameter of 60 nm, the dipole resonance becomes broader.

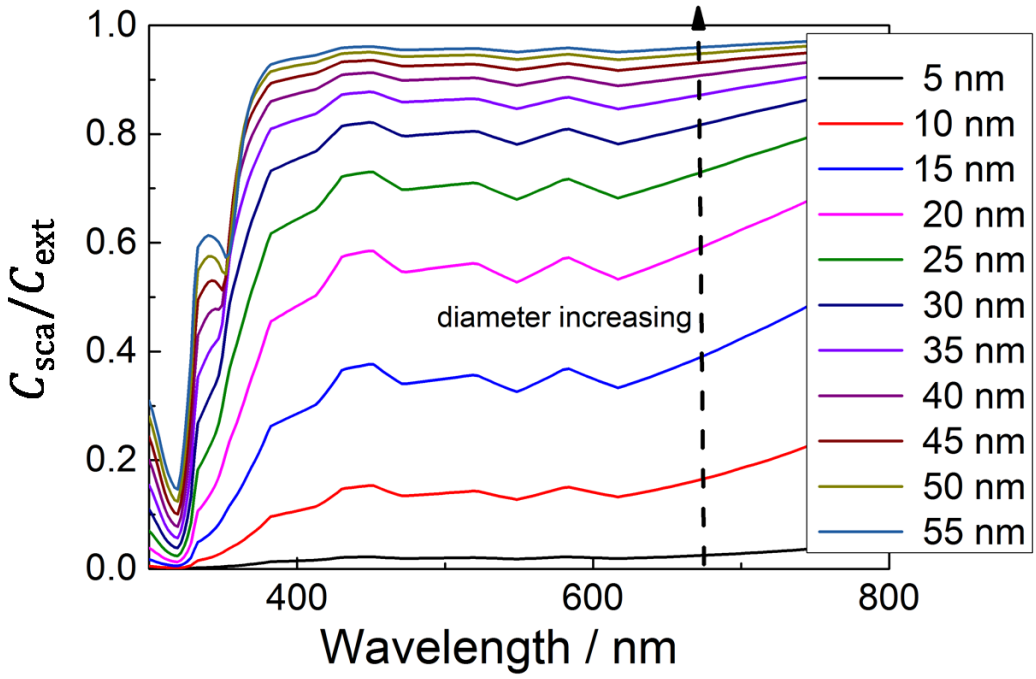


Fig.5.3 Scattering efficiency ($C_{sca}/C_{ext}$) of a Ag sphere dependence of the diameter $d$

Equations 5-2 and 5-3 show the trend that $C_{sca}$ is increasing more rapidly than $C_{abs}$ as the size is increasing. Fig.5.3 shows the scattering efficiency ($C_{sca}/C_{ext}$) dependence of the diameter of Ag sphere. The 5-nm-diameter Ag sphere has a low $C_{sca}/C_{ext}$ value, which indicates that the sphere absorbs the most incident light. As the diameter goes up, scattering efficiency $C_{sca}/C_{ext}$ keeps increasing and gradually approaches 1. This implies that bigger size is favourable to take advantage of the scattering ability of metallic nanoparticles.

The surrounding media can significantly alter the optical responses of the metallic nanoparticles as well. Fig.5.4 shows the cross sections ($C_{sca}$, $C_{abs}$, $C_{ext}$) of a 30-nm-diameter Ag sphere in medium with varied refractive index ($n$). The resonance peak red-shifts significantly due to the increase in the refractive index of the surrounding media. This is because the higher refractive index media can weaken the accumulation of charges around the particles and a resulting weakened storing force. This can be also

interpreted in another way: the effective wavelength in the media is reduced to $\lambda/n$ and leads to the red-shift of the resonance peak [86].

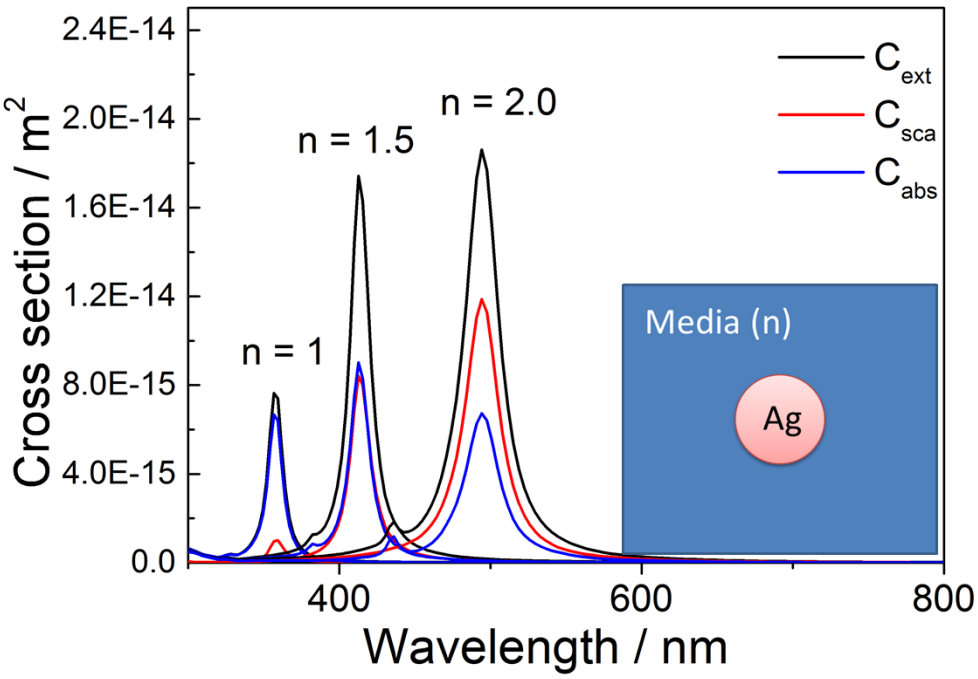


Fig.5.4 Cross sections ($C_{sca}$, $C_{abs}$, $C_{ext}$) of a Ag sphere (30 nm in diameter) in medium with varied refractive indexes

For metallic nanoparticles at the interfaces, particles preferentially scatter the light towards the side with a higher refractive index due to the corresponding higher optical states [78]. Fig.5.5 depicts the angular distribution of the radiation power of the dipole for a 120-nm-diamter sphere at the interfaces of air-air and air-AZO. At the air-air interface, scattering is equal between the backward and the forward. However, due to the refractive index of AZO being higher than air, the forward scattering is dominant at the interface of air-AZO. The calculation of angular distribution of the scattering power in Fig.5.5 is done via finite element method (FEM) using the software JCMwave [87]. The preferential scattering can be utilized to couple the light into the solar cells more efficiently.

Conclusively, to utilize the plasmonic metallic nanoparticles for light absorption enhancement in the solar cells, the location and the geometry of metallic nanoparticles should be thoughtfully tuned and designed to achieve maximum effective light absorption.

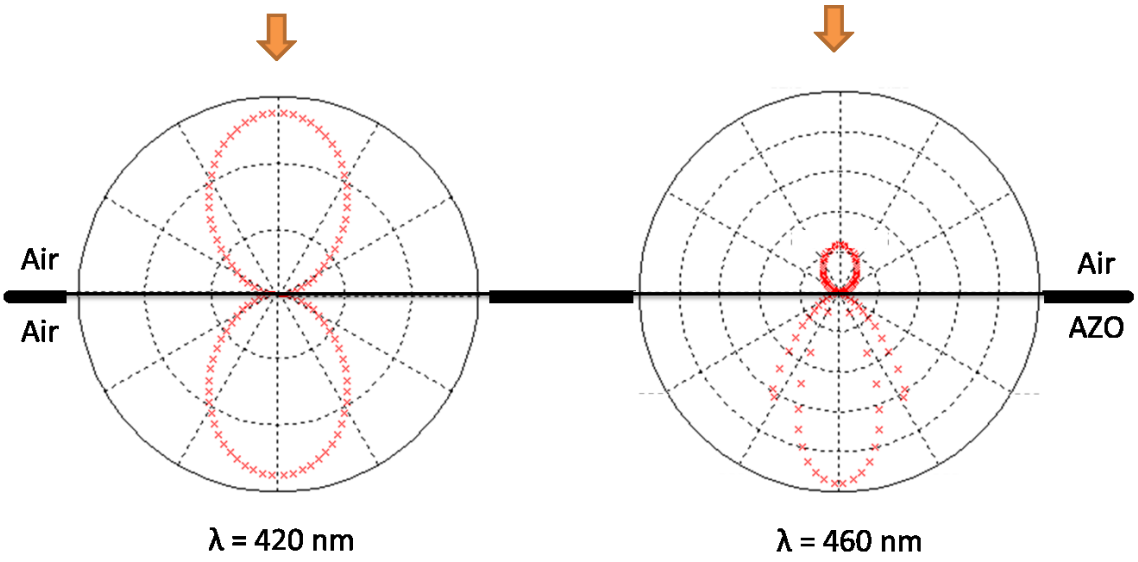


Fig.5.5 Angular distribution of scattering power of the dipole for a 120-nm-diameter sphere at the interfaces of air-air and air-AZO

### 5.1.2 Determination of plasmonic materials and location of particles in the CIGSe solar cell

**Plasmonic Material:** Amongst these most commonly used metallic materials, like Au, Ag, Cu and Al, Ag is chosen as the plasmonic material in this work. Two reasons contribute to the decision. Firstly, Ag has a strong resonance and low absorption ability in the spectrum of interest [85]. Moreover, Ag nanoparticles can be easily fabricated by surface-tension-induced agglomeration method [65], without needing expensive and complicated lithography technologies.

**Location:** Regarding the location of particles in the solar cell, we can in principle place the particles at any interface and even within layers. For the consideration of thermal stability of Ag particles and favourable electrical properties of solar cells, it is not suggested to put the nanoparticles at interfaces within AZO/ZnO/CdS/CIGSe/back contact. Placing the particles on the top of solar cells (air/AZO) is not recommended as well. This is due to fano effect [88]. The scattered light at wavelengths below the resonance is out of phase with the incident light, which leads to destructive interferences and poor coupling of light into the underlying solar cell. For Ag particles, this fano effect can largely reduce the absorption of solar cells in the visible wavelength range, the effective absorption over the whole wavelength range can be consequently reduced. Besides, in my experimental case, the method for preparing Ag nanoparticles requires

substrate temperature above 200 °C, which can cause the diffusion of CdS buffer layer and damage the solar cells. The location of the interface of back contact/glass substrate is the option left. However, due to the high absorption ability of Mo substrate, there will be no light penetrating it even for a 100 nm thick layer. To demonstrate the benefit of Ag particles, the transparent back contact is demanded to replace Mo. In my experiment, ITO (Sn doped $In_2O_3$) is employed for its successful application in the transparent CIGSe solar cells [61]. As mentioned above, taking advantage of the near field concentration is required to place the nanoparticles to the photoactive layer closely, which indicates that the location is either at the interface of CdS/CIGSe or CIGSe/back contact. Therefore, the utilization of the near field enhancement is not realistic if placing the nanoparticles at the interface of glass/ITO. I will limit the investigation to the enhancement mechanism of plasmonic scattering in this chapter.

### 5.1.3 Challenges of incorporating metallic nanoparticles into CIGSe solar cells

Why are there few successful applications of metallic nanoparticles for light absorption enhancement in CIGSe solar cells? Taking Si-based solar cells as references, the specific reasons are assumed as follows: 1) the fabrication of metallic nanoparticles is done on top of $Si_3N_4$ or $SiO_2$ passivation layer for crystalline Si solar cells, which can prevent the metallic particle diffusion into solar cells. Or the deposition of amorphous/nano-crystalline Si solar cells can be done at a temperature below 200 °C, which is not high enough to trigger the diffusion of metallic particles underneath the back contact layer (TCO). However, the CIGSe absorber is usually deposited above 500 °C, which poses high risk to trigger the diffusion of metallic material through the back contact. 2) CIGSe solar cells perform much more inferiorly on the ITO back contact than the conventional Mo due to the mismatch of working functions between ITO and CIGSe layers [11].

To be promising, it was discovered in my experiment that low deposition temperature (440 °C) could improve the solar cell performance on ITO substrate. Moreover, the low deposition temperature can reduce the risk of Ag diffusion into the CIGSe absorber. Therefore, low deposition temperature is taken for the CIGSe solar cells incorporating Ag particles at the interface ITO/glass in this work.

# 5.2 Experimental incorporation of Ag nanoparticles into CIGSe solar cells

## 5.2.1 Fabrication of Ag nanoparticles

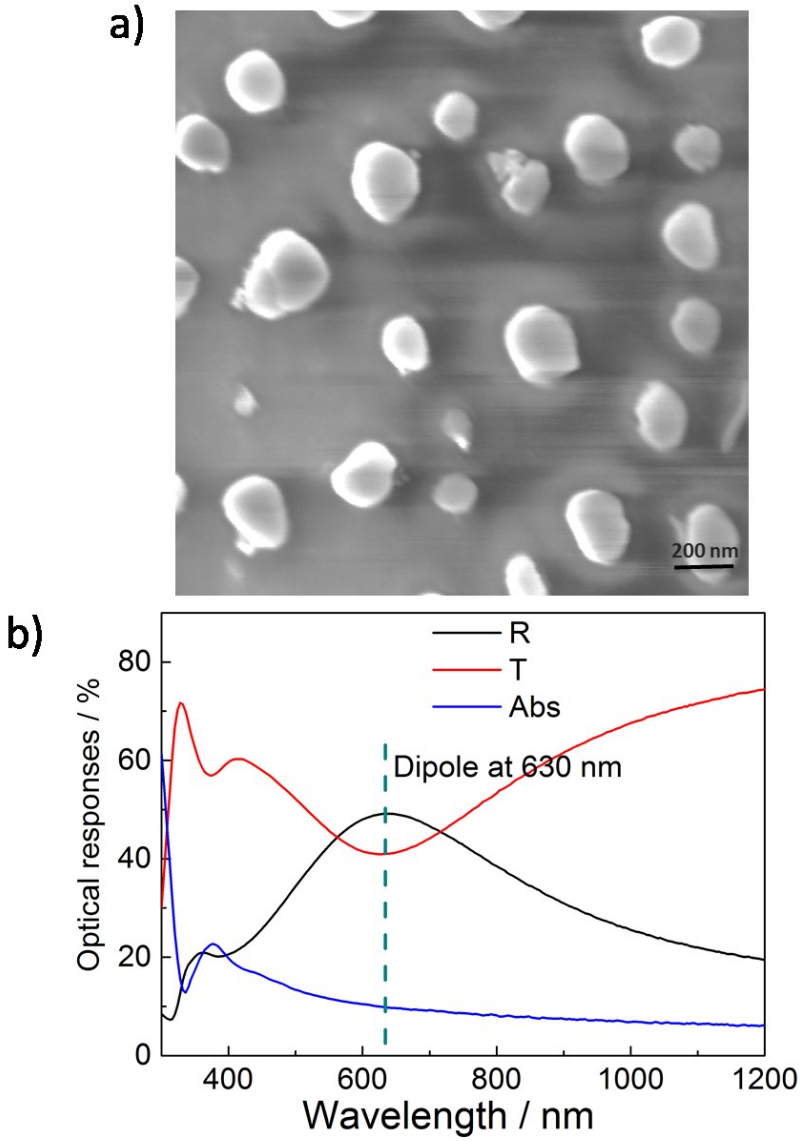


Fig.5.6 a) surface morphology, b) optical responses (*R, T, Abs*) of Ag nanoparticles on glass substrate

The Ag particles were prepared by the so-called surface-tension-induced agglomeration method. A 30 nm thick Ag film was grown on glass substrate by e-beam evaporation. Subsequently, Ag films were annealed at 450 °C for 30 minutes in ambient atmosphere. Fig.5.6 (a) shows the surface morphology of prepared Ag nanoparticles, we can observe

approximately ellipsoidal Ag particles. They are randomly separated and the 200 nm-major radius particles dominate the size distribution. The corresponding optical responses (R/T/Abs) are depicted in Fig.5.6 (b). There is a broad resonance peak centered at the wavelength of 630 nm. This corresponds to the dipole resonance mode of Ag nanoparticles. The broadness of the resonance peak is due to the non-uniform size distribution and is actually beneficial for the broadband light-trapping requirement. Besides, the absorption for the prepared nanoparticles is below 10 % beyond 600 nm, which suggests that the scattering predominates over parasitic absorption over the most wavelength range. As to the strong parasitic absorption in the wavelength range below 600 nm, this does not worsen the light-trapping effect of cells since light in this wavelength range is mainly absorbed by the cell before reaching the Ag nanoparticles at the interface of ITO/glass substrate.

### 5.2.2 Introduction of an $Al_2O_3$ passivation layer

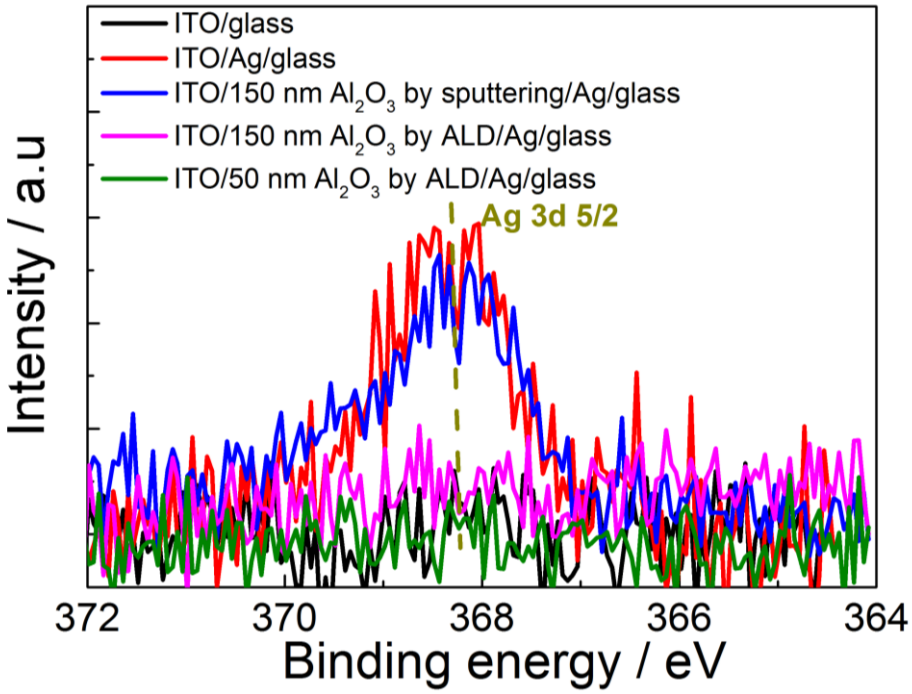


Fig.5.7 Investigation of Ag diffusion after the CIGSe deposition process via X-ray photoelectron spectroscopy (XPS)

Though CIGSe deposition temperature was largely reduced to 440 °C in the experiment, we still couldn't make sure that Ag nanoparticles are thermally passivated. To confirm

this, the Ag nanoparticles were coated by a 200 nm thick ITO back contact layer and the sample (ITO/Ag/glass substrate) experienced the whole CIGSe deposition process but is blocked from CIGSe deposition by a mask on top. X-ray photoelectron spectroscopy (XPS) is then used to characterize from the ITO surface and the result is shown in Fig.5.7. We can see that the signal of Ag is still detected, which means that the ITO layer fails to thermally passivate the Ag particles even at the reduced substrate temperature during the CIGSe deposition. Further lowering CIGSe deposition temperature may help block the diffusion of Ag, this will however lead to low-quality CIGSe absorbers and is not suggested. Increasing the thickness of the ITO layer is another alternative approach to thermally passivate the Ag nanoparticles, this is not feasible as well. Because ITO also has strong absorption ability due to free charge carriers, especially in the near infrared range, thicker ITO layer implies that more part of back-scattered light from Ag particles will be dissipated in ITO. A third approach is to insert a layer between ITO and Ag nanoparticles. This layer should fulfill at least two requirements: 1) there is no absorption ability in the range of 600-1200 nm, where ultra-thin CIGSe solar cells have poor absorption; 2) this inserting layer should be quite compact and thermally stable. Accordingly, dielectric materials like $Al_2O_3$ and $Si_3N_4$ fulfill the requirements mentioned above. Considering the available experimental conditions, $Al_2O_3$ is selected.

The $Al_2O_3$ film was prepared by Atom Layer Deposition (ALD) using trimethylaluminium and deionized water as precursors at room temperature. To determine the proper thickness of $Al_2O_3$, both 50 and 150 nm were tested. The XPS results are included in Fig.5.7 as well, it can be observed that even the 50-nm-thick $Al_2O_3$ film is able to block the diffusion of Ag particles. I should stress here that whether the $Al_2O_3$ film can passivate the diffusion of Ag is also dependent on how the $Al_2O_3$ film is prepared. Fig.5.7 shows the XPS result of the sample corresponding to a sputtered 150-nm-thick $Al_2O_3$ film, which fails to block the diffusion of Ag. This is probably due to that the ALD-prepared $Al_2O_3$ film has better conformity to the surface features and is much more compact than the sputtered.

Fig.5.8 shows both the cross sections and surface topographies of the ITO/$Al_2O_3$/Ag NP/glass substrate samples with different thicknesses of $Al_2O_3$ films prepared by ALD. The cross sections show the Ag particles survived after the CIGSe deposition and are conformally covered by the compact $Al_2O_3$ films. This observation reflects the XPS

results. What is more, the ITO layer is also laterally continuous on top of the $Al_2O_3$ layer and no fracture is observed, which is critical for electrical properties of the back contact. The top views also confirm the conformal growth: the particles tend to 'grow' bigger and become closely touched when the thickness of the $Al_2O_3$ film is from 50 nm to 150 nm.

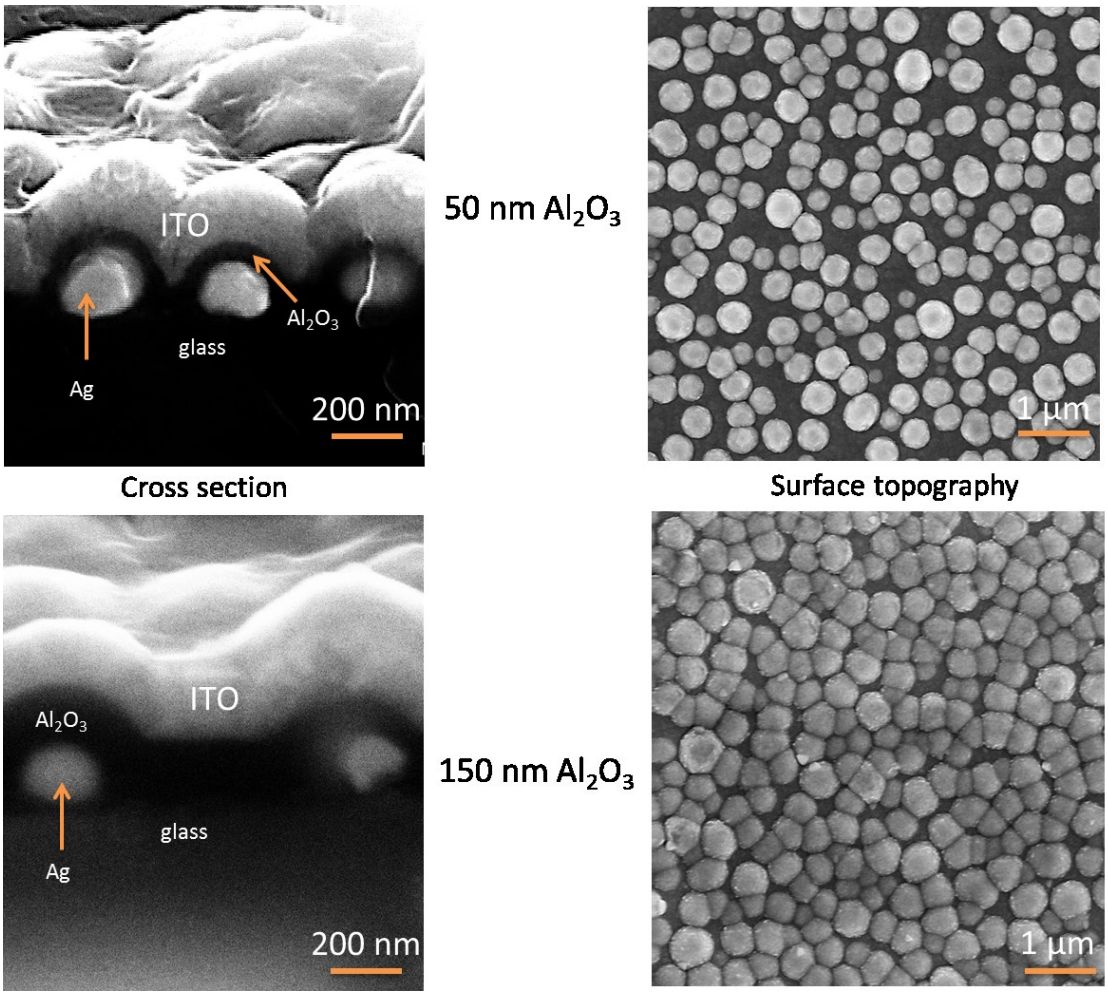


Fig.5.8 Morphologies of the structure of ITO/$Al_2O_3$/Ag/glass substrate after experiencing the CIGSe deposition

The coated $Al_2O_3$ film can influence the optical responses of Ag nanoparticles as well. Fig.5.9 shows the R comparison of Ag nanoparticles before and after the 50-nm-thick ALD-prepared $Al_2O_3$ film. The dipole resonance peak red-shifts from the wavelength 630 nm to around 790 nm due to the higher refractive index of $Al_2O_3$ than air. Actually, this redshift is beneficial for the light trapping since the resonance peak is shifted to the center of the poorly absorbed wavelength range for ultra-thin CIGSe solar cells.

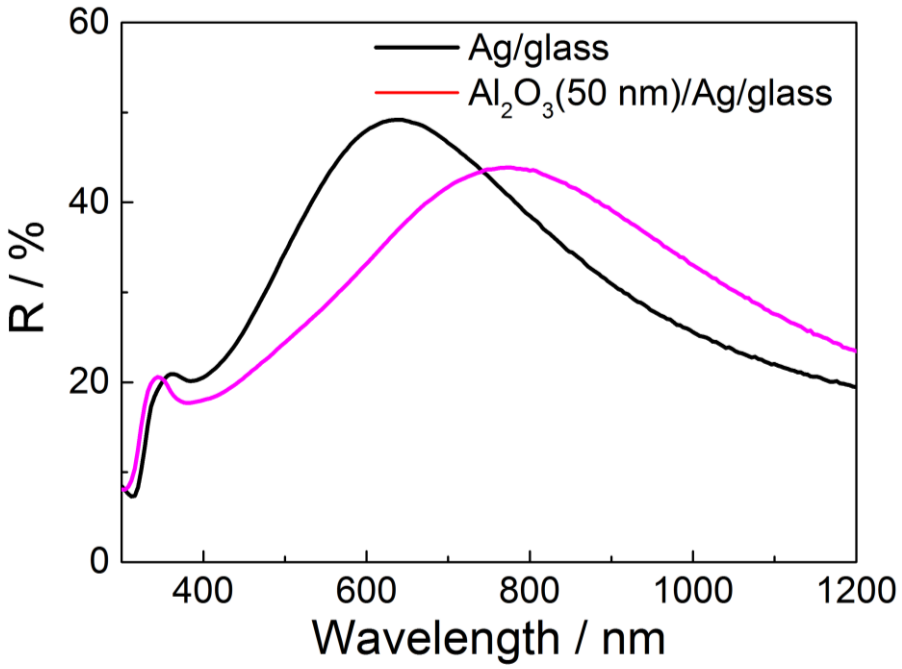


Fig.5.9 R comparison of Ag/glass substrate before and after coating the 50-nm-thick ALD-prepared $Al_2O_3$ film

### 5.2.3 Solar cell performance incorporating Ag nanoparticles

To confirm the light-trapping effect of Ag nanoparticles on the ultra-thin CIGSe solar cells, the solar cells were prepared subsequently on top of ITO/$Al_2O_3$/Ag/glass. The 50-nm-thick $Al_2O_3$ sample was taken since this thickness can already passivate the diffusion of Ag. The CIGSe thickness is 460 nm. For comparison, solar cells without Ag nanoparticle incorporation were also done simultaneously. Unfortunately, the cells with Ag nanoparticles still did not work electrically. The reason is assumed to be related to the textured ITO layers from the conformal growth shown in Fig.5.8. Each single solar cell was mechanically scribed from 2.5*2.5 cm substrate to 0.5*1 cm. However, due to the texture on the back contact, the mechanical needle either failed to completely separate the CIGSe absorber or cut off the back ITO layer completely. This can shunt or open circuit the cells.

Anyway, the optical absorption (*Abs*) of the complete solar cells without (solid lines) and with (dashed lines) Ag incorporation were characterized and shown in Fig.5.10. It is seen that the *Abs* has a great enhancement in the wavelength range of 600-1200 nm due to the presence of Ag nanoparticles. Since the solar cells couldn't work electrically and Ag nanoparticles can also have the parasitic absorption, it is difficult to comment

whether the absorption increase of the complete solar cell ($Abs_{solarcell}$) is from the effective $Abs_{CIGSe}$ or the parasitic absorption in either particles or any of the other layers. To distinguish this point, 3-D FEM simulations are carried out to check whether Ag nanoparticles can contribute to the effective $Abs_{CIGSe}$ using the complete Finite Element software package (JCMwave).

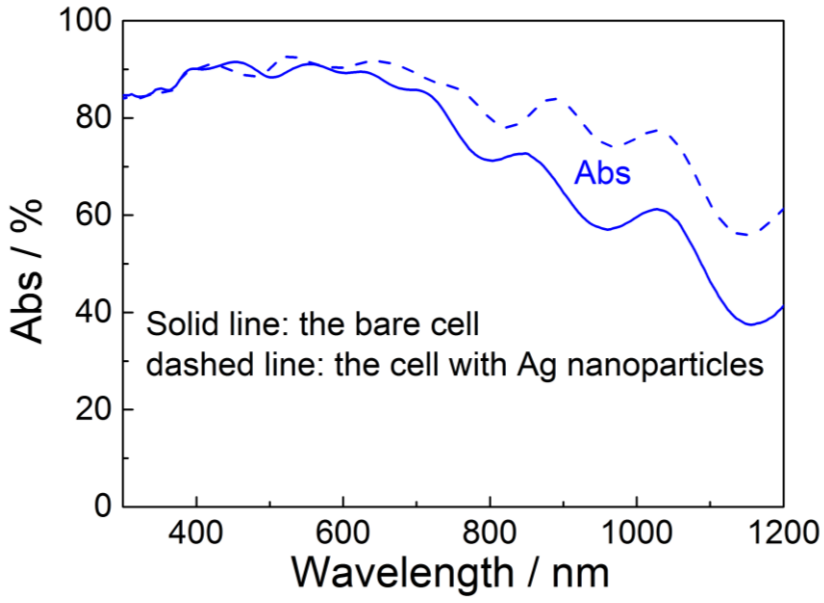


Fig.5.10 Abs of the complete cells with and without Ag incorporation

To make the simulation comparable to the experimental case, the simulation unit consists the structure of AZO/ZnO/CdS/CIGSe/ITO/$Al_2O_3$/glass substrate with the thicknesses of 240/130/100/460/200/50/200 nm from top to bottom. The structure and thickness values are according to the experimental samples. The optical constants are the same as given in chapter 4. The Ag nanoparticles are assumed to be tetragonally coordinated at the interface of $Al_2O_3$/glass substrate with a height of 40 nm, a length of 150 nm and a pitch of 270 nm. This geometry gives a comparable resonance (around 800 nm) to the experimental samples. Perfectly matching layer (PML) boundary conditions in the positive and negative z direction was used. The simple simulation structure is illustrated as Fig.5.11 a). To reduce the programming and calculation efforts, conformal growth of layers on top of Ag nanoparticles is not taken into account. Since we intend to confirm that $Abs_{solarcell}$ is from the $Abs_{CIGSe}$ or not, the approximation is still reasonable to predict the optical responses of the solar cells. Fig.5.11 b) shows both the $Abs_{CIGSe}$ and $Abs_{solarcell}$ with and without Ag nanoparticles (the absorption responses of solar cells without Ag particles are calculated by Transfer-Matrix method).

After incorporating Ag nanoparticles, the $Abs_{solarcell}$ is generally higher over the poor-absorbing spectrum, which agrees with the changing trend of the experimentally measured in Fig.5.10. Similar to the $Abs_{solarcell}$, $Abs_{CIGSe}$ is improved as well, which indicates that Ag nanoparticles can improve the effective $Abs_{CIGSe}$. Further, from the comparison of differences of $Abs_{solarcell}$ and $Abs_{CIGSe}$ with and without Ag nanoparticles, we can conclude that the improvement of $Abs_{CIGSe}$ dominates the increase of $Abs_{solarcell}$. Therefore, we can conclude that Ag nanoparticles at the interface of $Al_2O_3$/glass substrate can improve the effective absorption in CIGSe layers. Here, it is stressed again that the goal of this work is to prove the concept of the effective light-trapping effects of Ag nanoparticles at the interface of ITO/glass substrate. As to the maximum optical benefit, this requires further optimizations in the next step.

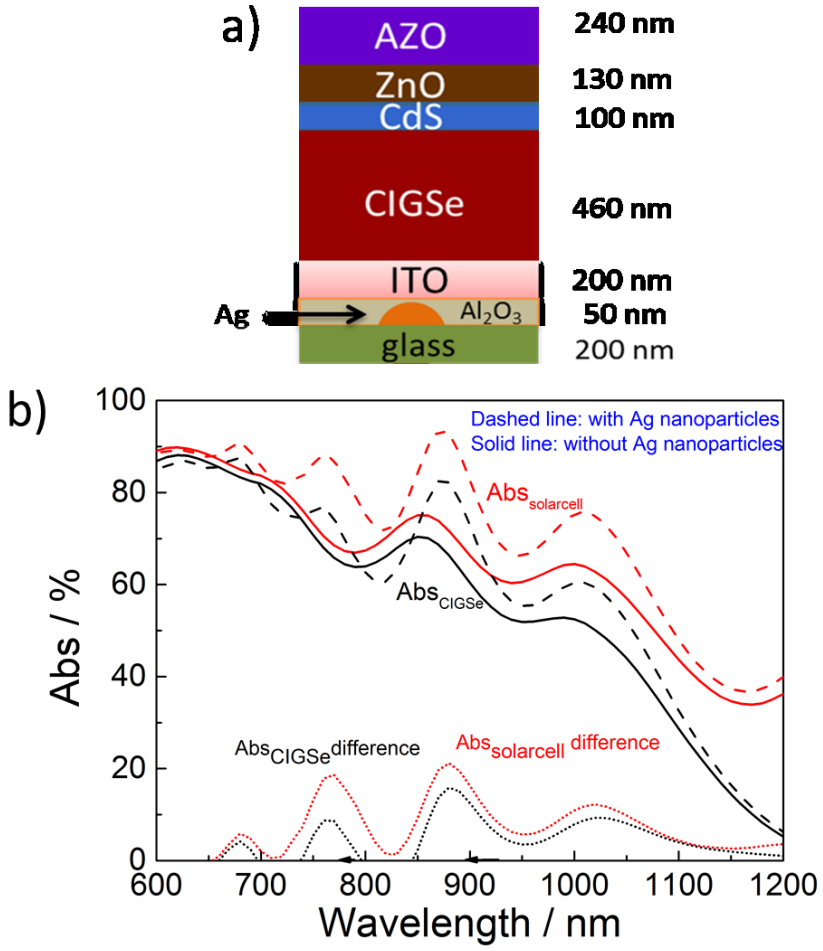


Fig.5.11 a) The cross section of the simulation unit for finite element method (FEM); b) simulate $Abs_{CIGSe}$ and $Abs_{solarcell}$ with and without Ag nanoparticles at the interface of ITO/glass substrate

## 5.3 Conclusion and outlook

In this chapter, incorporating Ag nanoparticles at the interface of ITO/glass substrate for light trapping has been investigated. It was confirmed that Ag nanoparticles can still penetrate the ITO back contact even at a low substrate temperature of 440 °C. The ALD-prepared $Al_2O_3$ film with a thickness of 50 nm is proved to be able to thermally passivate the diffusion of Ag. However, the solar cells fail to electrically perform well possibly due to the scribbling problems arising from the texture. With the help of the optical 3-D FEM simulation, it is proved that Ag nanoparticles underneath the ITO back contact can optically contribute to the effective $Abs_{CIGSe}$ of solar cells. It is therefore shown the potential to utilize the plasmonic scattering of Ag nanoparticles.

To transfer the optical benefit to the electrical gain of solar cells, the first and necessary step is to address the scribing problem arising from the texture of the back contact. Further, to achieve the optimum gain of light trapping and to reduce the parasitic absorption into minimum, theoretical simulations are required to optimize Ag nanoparticles for the experimental guidance. The optimizing parameters cover the size, shape and coverage of Ag nanoparticles, plus that Ag nanoparticles are periodically or randomly arrayed, which are closely related to the resonance positions and scattering efficiency.

# Chapter 6

# Light trapping by 2-D close-packed dielectric nanosphere arrays for ultra-thin $CuIn_{1-x}Ga_xSe_2$ solar cells

Table 6.1: Comparison of the related properties between the metallic and dielectric nanoparticles with respect to the light trapping elements in solar cells

| | **Metallic** | **Dielectric** |
|---|---|---|
| **High scattering ability** | √ | √ |
| **No parasitic absorption** | × | √ |
| **Good thermal stability** | × | √(Inorganic) |
| **No recombination center** | × | √ |
| **Low cost** | × | √ |

Besides the plasmonic metallic ones, dielectric nanoparticles can also serve as light-trapping elements in solar cells. For a first and clear comparison, Table 6.1 summarizes the properties between the metallic and dielectric nanoparticles serving as the light trapping elements in solar cells. Unlike the metallic materials, dielectric materials don't have free electrons. Dielectric nanoparticles can also however oscillate and have resonances in response to the incident electromagnetic waves [80]. The resonances are commonly termed as Mie resonances, which is distinguished from the plasmonic resonances in metallic nanoparticles. The scattering ability of dielectric nanoparticles is dependent on the geometry of the nanoparticles and surrounding media, dielectric nanoparticles are proved to be able to feature a comparable scattering ability to the metallic counterparts via the Mie resonances [89]. Fig.6.1a depicts the calculated scattering cross-section (normalized to the geometrical cross section) contour image of a dielectric sphere in air ($n$ = 1, $k$ = 0) dependence of size using Mie theory. The optical constants of the sphere are set constant ($n$ = 2, $k$ = 0), which are comparable to the commonly used inorganic dielectric materials (eg. $SiO_2$, $Al_2O_3$, $Si_3N_4$). When the size is beyond 400 nm in diameter, the scattering cross-section can exceed the geometrical

cross-section overall the whole spectra of interest (400–1200 nm). Besides, it can be observed that the maximum cross section is more than 5.5 time times larger than the geometrical cross section. The wavelength for the maximum scattering cross section is nearly linear to the diameter of a sphere. To clearly see the resonance details, Fig.6.1b shows the scattering cross-section spectra of the 400-nm-diameter sphere. There are three distinct resonances corresponding to the dipole, the quadrupole, the hexapole Mie modes. Remarkably, the dielectric materials have almost no parasitic absorption. The benefit of no parasitic absorption is especially obvious if the particles are located on top of the absorbers in solar cells. Metallic nanoparticles (Au, Ag) were proved to always have the serious parasitic absorption in the short wavelength range and negatively affects the absorption enhancement overall the spectrum of interest when they were placed on the surface of solar cells. This concern is not however necessary for dielectric materials. As to the thermal stability, the inorganic dielectric materials (eg. $SiO_2$, $Al_2O_3$) are generally much superior to the metallic ones. Since the CIGSe absorber being prepared at temperature above 400 °C and AZO/ZnO at 150 °C, this indicates that it is not favourable to place the metallic particles without a passivation shell at the interfaces touching p, n layers of CIGSe solar cells. This is why in my experiments in chapter 5, Ag nanoparticles are placed at the interface of back contact (ITO)/glass substrate. However, even under the ITO layer at a low substrate temperature of 440 °C, Ag is able to penetrate through the ITO layer and could be only passivated when the additional compact layer is inserted. The diffusion not just influences the scattering properties of nanoparticles, but also has high risk to damage the solar cells. Comparatively, the stable inorganic materials like $SiO_2$, $Al_2O_3$, have higher potential to be applied within the interfaces of CIGSe solar cells. Besides, the metallic nanoparticles can also serve as recombination centers. Further, the normally used metallic nanoparticles are the noble Au, Ag, which cost more than the dielectric materials. Conclusively, dielectric nanoparticles are potentially more compromising than the metallic ones as light-trapping elements for CIGSe solar cells. Nevertheless, whether the dielectric nanoparticles are compatible to the performance stability and can enhance the light absorption of the CIGSe solar cells is unknown and not thoroughly investigated. Therefore, the light-trapping structures based on the dielectric nanoparticles will be focused on ultra-thin CIGSe solar cells in this chapter and chapter 7.

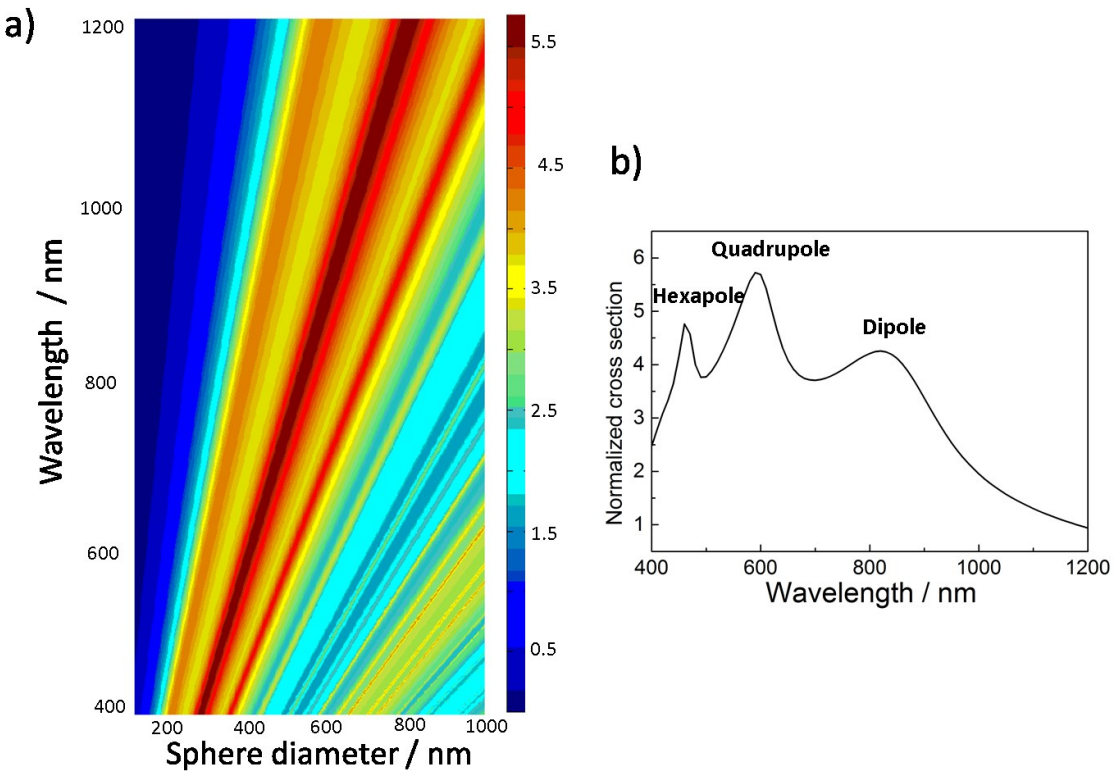


Fig.6.1 a) Contour image of the scattering cross-section (normalized to geometrical cross section) of a sphere ($n$ = 2, $k$ = 0) in air ($n$ = 1, $k$ = 0); b) scattering cross-section spectra for the 400-nm-diameter sphere

Dielectric nanostructures have substantiated the potential to significantly enhance the light absorption of solar cells by coupling incident light to various guided modes [90]. Besides the general Mie resonant modes, which are universal to dielectric nanoparticles, some particles with specific shapes can have other resonant modes. The 2-D dielectric nanosphere arrays are a promising light-trapping structure for solar cells when the sphere size is comparable to the incident wavelength and were substantiated to be able to support Whispering Gallery Modes (WGMs) [91] both theoretically and experimentally. The WGMs can significantly increase the absorption in Si and GaAs solar cells by leaking the confined light in the resonant modes into the solar cells if the spheres are placed in close proximity to solar cells [66, 92, 93]. WGMs are specific modes of a wave field circling inside a cavity surface due to the total refection. Besides the total reflection, the condition of the constructive interference should be fulfilled as well that the wave should propagate back to the initial point with the same phase [91].

Apart from the optical lossless property of the dielectric materials, the dielectric 2-D nanosphere arrays have other advantages [66, 92-94]: 1) the geometry of spheres is symmetric, which enables to accept the large angular incidence of light without increasing great reflection loss; 2) the sphere array can be prepared by the simple and cheap self-assembly methods rather than the complicated and expensive lithography technologies and the preparation can be easily scaled to large area.

Though 2-D $SiO_2$ nanosphere arrays have been proven to be able to enhance the light absorption for amorphous Si and GaAs solar cells mainly in terms of WGMs [66, 92], whether and how the 2-D nanosphere arrays benefit the CIGSe solar cells needs to be identified. In this chapter, I will investigate in detail how the nanosphere arrays work on the surface of ultra-thin CIGSe solar cells and identify the absorption enhancement mechanisms.

Regarding the locations of sphere arrays in CIGSe solar cells, placing the sphere arrays at the interfaces within the solar cells is not favoured for the consideration of electrical properties. This is because: for large spheres, the thicknesses of thin layers in the solar cell are below the size of spheres, which possibly leads to a laterally discontinuous layer on top or/and increases the interface area and a higher carrier recombination; for small spheres, the following deposited layer couldn't penetrate to the small space between the spheres. Therefore, the interface Air/AZO (surface) is selected for the location of nanosphere arrays.

## 6.1 Numerical demonstration

### 6.1.1 Finite Element simulation

To understand better how the 2-D nanosphere arrays perform on CIGSe solar cells, the 3-D numerical simulations were carried out using a complete Finite Element software package (JCMwave). Fig.6.2 a) depicts the illustration of a nanosphere array on a CIGSe solar cell. The nanosphere array is assumed to be hexagonally coordinated and close-packed, because this structure is commonly fabricated by the simple and cheap self-assembly methods. A corresponding cross section is also illustrated in Fig.6.2 b). The thicknesses of the AZO/ZnO/CdS/CIGSe/Mo layers are 240/130/100/300/200nm. The interfaces between the layers are assumed to be flat. The optical constants of each layer in the cell are the same as used in the simulations in chapter 4.

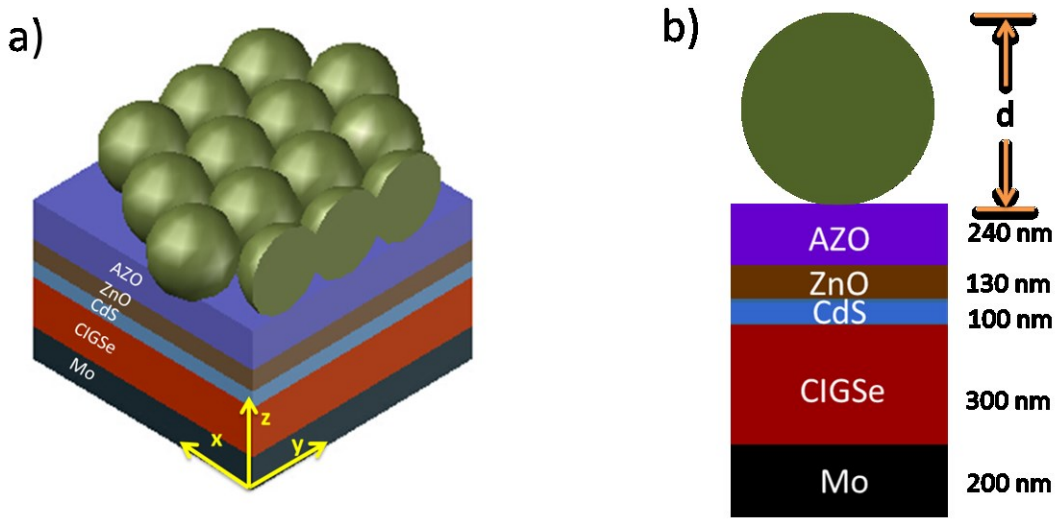


Fig.6.2 a) Schematic illustration of hexagonally close-packed $SiO_2$ spheres atop of an ultra-thin CIGSe solar cell, b) a corresponding cross section

A hexagonal computational domain with three sets of periodic boundary conditions in the x-y plane and perfectly matching layer (PML) boundary conditions in the positive and negative z direction was used. The light is normally incident along the z axis and the polarization direction is along the x axis. The electric field intensity profiles ($|E|^2/|E_0|^2$) in the following images are normalized to the incident electric field intensity ($|E_0|^2$).The diameter of the computational domain was made 10% smaller than the diameter of the simulated spheres. This was done in order to, firstly, avoid the spheres touching the periodic boundaries at a singular point, and secondly, to more accurately model particles in the monolayer, which will be compressed slightly by surrounding particles causing a deviation from the spherical shape. The illumination was a plane wave orientated along the negative z axis (normal incidence). The polarization direction is in x axis. To calculate the absorption in the layers of the solar cell, the total field integration inside those layers was used. The corresponding photocurrent density is integrated assuming complete conversion of absorption to collected carriers under standard AM 1.5 illumination condition. To calculate the reflection, the integration of the pointing flux of the scattered wave leaving the domain in the positive z direction was used.

### 6.1.2 Large sphere array

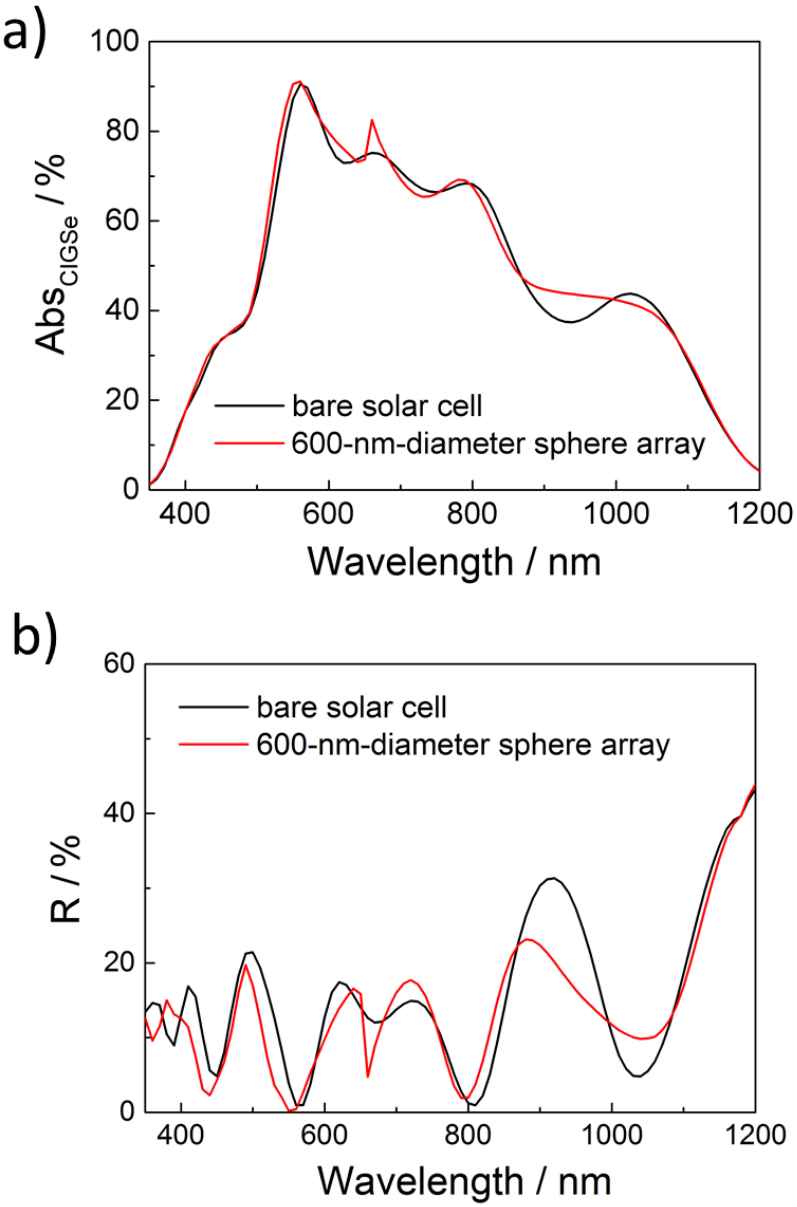


Fig.6.3 Comparison of a) absorption in CIGSe ($Abs_{CIGSe}$) for the solar cells without and with the presence of the $SiO_2$ nanosphere array and b) reflection ($R$) without and with the 600-nm-diameter $SiO_2$ sphere array

**Whispering Gallery modes**

It has been investigated that the refractive indexes of surrounding media determines the optical properties of the nanoparticles to a great extent. I start the investigation from the dielectric sphere with a low refractive index ($SiO_2$, $n$ = 1.46), which is lower than the underneath medium (AZO here). Fig.6.3 a) compares the absorption in the CIGSe layer ($Abs_{CIGSe}$) for the solar cells without and with the presence of the $SiO_2$ nanosphere arrays. Taking the 600-nm-diameter sphere array as example, there is a reduction in

$Abs_{CIGSe}$ in certain narrow wavelength ranges due to the interference shift. We however can see an overall enhancement of $Abs_{CIGSe}$ over the whole spectrum. The integrated current density is 24.94 mA/cm$^2$, which corresponds to an enhancement of 0.34 mA/cm$^2$ compared to the cell without the $SiO_2$ sphere array. Remarkably, a sharp and discrete absorption enhancement can be observed at around $\lambda$ = 660 nm. This is due to the resonant modes of the sphere array. To further identify it, the electric field intensity profiles in the middle of a sphere in the (y-z) and (x-z) planes are shown in Fig 6.4 a). There are obvious lobes where the electrical field is intensified within the sphere. This particular mode pattern has been attributed to whispering gallery modes (WGMs) [93]. The WGMs act as a cavity for light, trapping it inside the $SiO_2$ sphere. It can be reflected by the largely reduced *R* at around $\lambda$ = 660 nm shown in Fig.6.3 b). Due to the underlying AZO layer having a higher refractive index than air, WGMs have a low Q factor and the confined electric field within $SiO_2$ spheres preferentially leaks into the underlying solar cell. From the electric intensity profiles in Fig.6.4 a), we can observe this leaky effect: the intensity of enhanced electric field is gradually attenuating as it is propagating from the sphere to the solar cell below. Besides, the electric field intensity lobs at the left and right sides in the (y-z) plane are extending beyond the $SiO_2$ sphere, which indicates the WGMs are the collective resonances due to the inter-coupling of spheres in proximity. For comparison, the electric field intensity profiles in the (y-z) and (x-z) planes for a wavelength off resonance ($\lambda$ = 710 nm) is also shown in Fig.6.4 b). The electric field intensity inside the sphere is greatly reduced, which leads to less light being incoupled to the underlying solar cell. As the $SiO_2$ diameter varies, the coupling conditions of WGMs between the spheres and the resoance wavelength actually change as well.

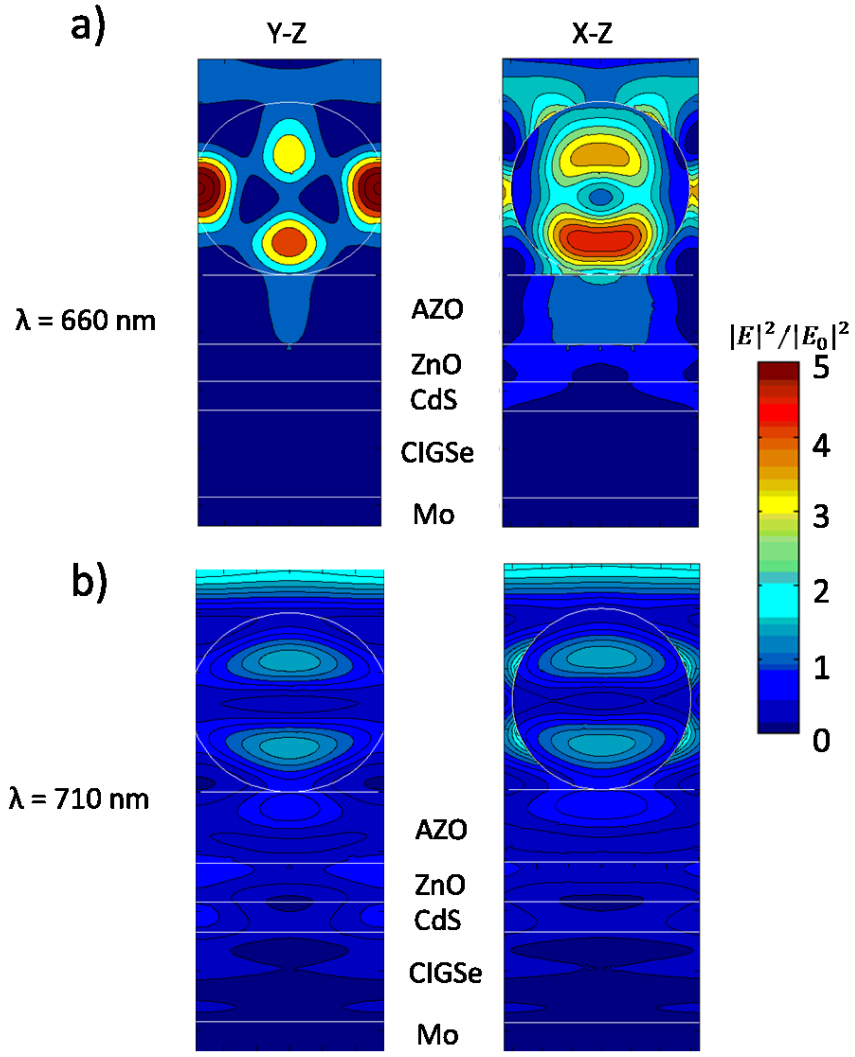


Fig.6.4 The cross sections of electrical field intensity at the middle of the 600-nm-diameter sphere in both (y-z) and (x-z) planes, a) at the resonance wavelength (λ = 660 nm); b) off the resonance wavelength (λ = 710 nm)

**High order multiple resonances**

From Fig.6.3, we can find that the $Abs_{CIGSe}$ enhancement arising from WGMs is only available in a narrow wavelength range due to the nature of resonant behavior. This is incompatible with the requirement of the broad band enhancement in the solar cells. From our simulations, the minimum size of $SiO_2$ sphere supporting the WGMs is around 450 nm in diameter. Aside from the WGMs, there are multipole Mie resonances, which can concentrate light within spheres and preferentially scatter light into the forward direction (towards the solar cell in our case). The near field intensity profiles at λ = 400 and 500 nm in Fig.6.5 a) and b) confirm the concentration and preferential scattering of light. Higher order multipole resonances (without dipole) of

spheres were proved to be able to obviously benefit the light absorption in crystalline Si solar cells. However, the excitation of higher order multipole resonances mainly lies in short wavelength range, which is within the parasitic absorption range of AZO/ZnO/CdS for CIGSe solar cells. The electric field intensity profiles in Fig.6.5 a) and b) imply this. We can observe that the concentrated electric field leaks into the underlying solar cells but is attenuated almost completely before reaching the CIGSe layer. This indicates the corresponding benefit is dissipated by the parasitic absorption in AZO/ZnO/CdS layers. This observation is in agreement with the corresponding $Abs_{CIGSe}$ and R curves in Fig.6.3 a) and b): there is a reduction in $R$ but barely an increase of $Abs_{CIGSe}$ in the range of 350-600 nm with the presence of the 600-nm-diameter $SiO_2$ sphere array on top.

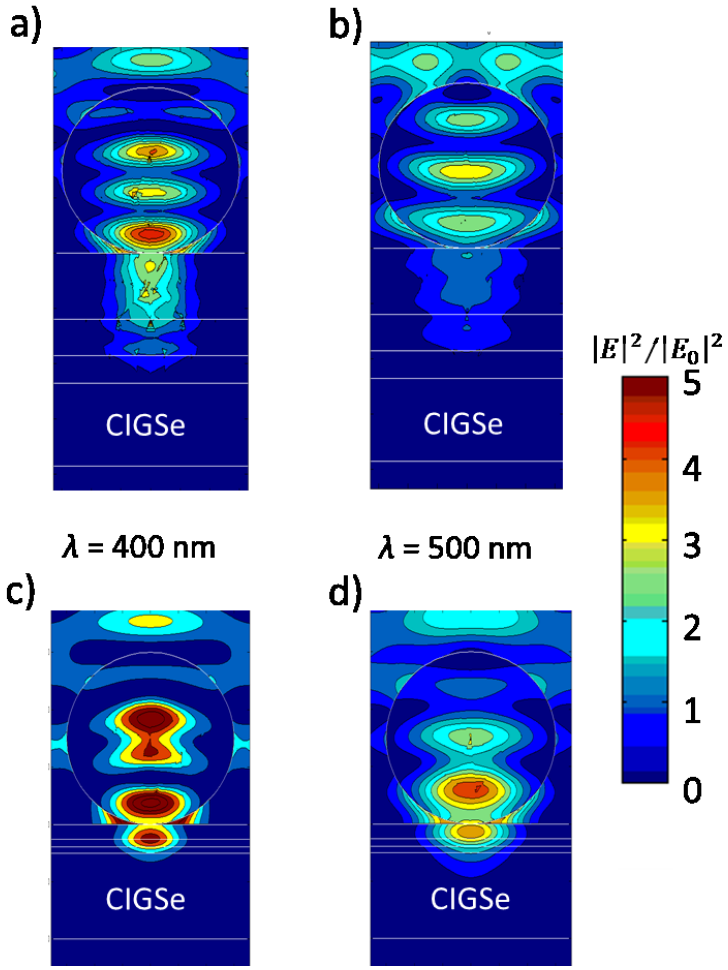


Fig.6.5 The cross sections of electrical field intensity at the middle sphere in the (x-z) plane for at λ = 400 and 500 nm for solar cells with two different thick AZO/ZnO/CdS layers

One approach to take advantage of the higher order mutipole resoances is to reduce the net thickness of the AZO/ZnO/CdS layers. Numerical simulation was also performed for the cell with 100-nm-net-thick AZO/ZnO/CdS layers. The individual thickness of AZO/ZnO/CdS layers is proportionally reduced to the net thickness 100 nm compared to the standard thicknesses. The electrical field intensity profiles at λ = 400 and 500 nm are plotted in Fig.6.5 c) and d). Compared to the cell with standard thick AZO/ZnO/CdS layers, the concentrated electric field penetrates into CIGSe layer for the cell with thinner AZO/ZnO/CdS layers. This enhances the absorption in CIGSe layers. The ratios of $Abs_{CIGSe}$ with $SiO_2$ spheres to that without are compared between cells having the two different thick AZO/ZnO/CdS layers in Fig.6.6. It is observed that the ratio for the cell with thinner AZO/ZnO/CdS layers is overall higher than that with the standard thickness in the wavelength range of 350 - 600 nm. The results are in line with the analysis from the electric field intensity profiles. However, thinning the AZO/ZnO/CdS layers should be experimentally compatible with the electrical properties of cells.

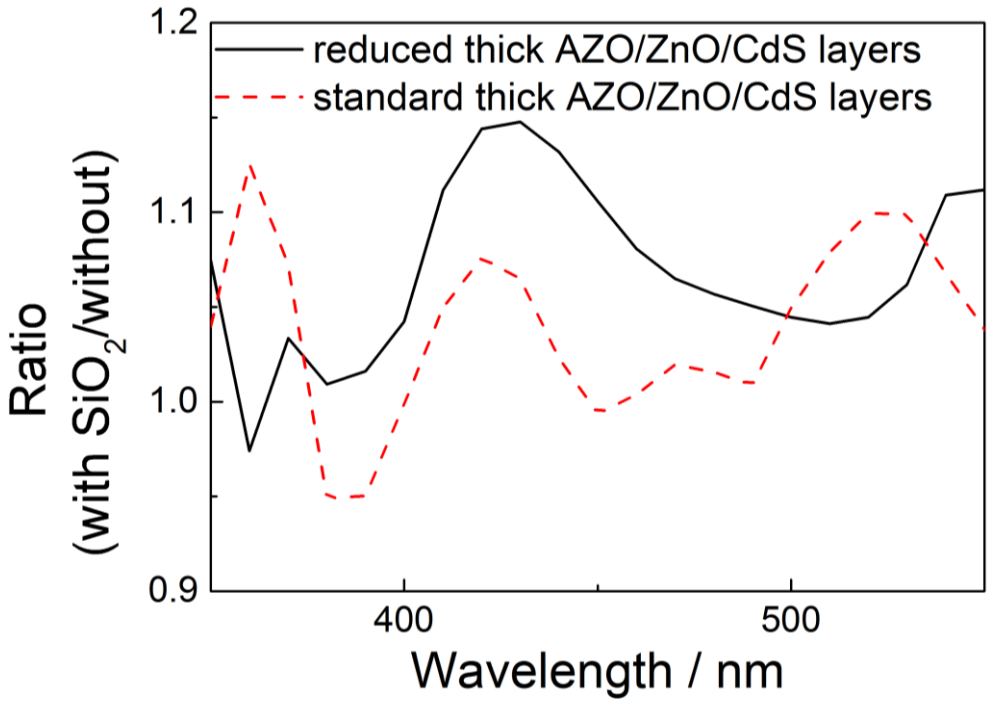


Fig.6.6 $Abs_{CIGSe}$ ratio of solar cell with $SiO_2$ to that without for two different net thick AZO/ZnO/CdS layers

Actually, as the sphere diameter ($d$) increases, the multipole resonances can be supported in a broader wavelength range, which can go beyond the parasitic absorption range of AZO/ZnO/CdS layers. This indicates that the multiple resonances of spheres

can be utilized for effective light absorption enhancement. Fig.6.7 shows the electric field intensity profiles in (x-z) plane at λ = 600 nm, 650 nm, 700 nm for the cell with the 875-nm-diameter sphere array. The intensified near field can penetrate the AZO/ZnO/CdS layers and reach the CIGSe layer, the effective light absorption enhancement is thus contributed.

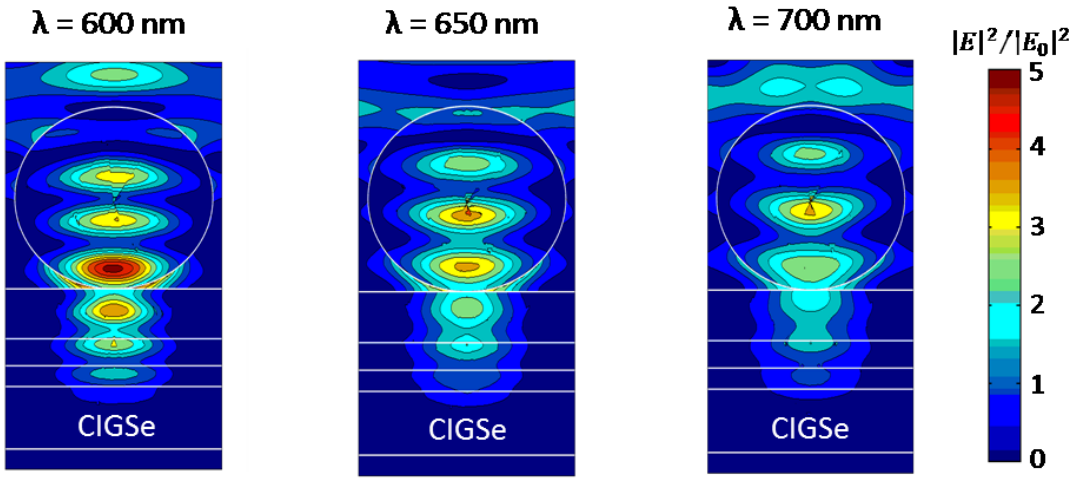


Fig.6.7 The cross sections of electrical field intensity at the middle sphere in the (x-z) plane for at λ = 600, 650 nm, 700 nm for solar cell with a 875-nm-diameter sphere array on top

The dipole resonance of spheres can also in principle scatter light preferentially into the cell. However, this beneficial effect was not seen (for example, the cell with 600-nm-diameter sphere array). The reasons can be interpreted from three factors: 1) The contacting area (point contact) between the sphere and the AZO layer is quite small and the preferential scattering is thus weakened; 2) The effective dipole for the large sphere is far away from the AZO layer and for small spheres the excitation wavelength range is within the parasitic range of AZO/ZnO/CdS layers, so the preferential scattering of the dipole is not obvious; 3) The refractive index of the AZO layer (substrate) is higher than that of the $SiO_2$ sphere (scatter), which can also restrain the preferential scattering of the dipole mode [89]. Of course, the three factors can suppress the preferential scattering of higher order resonances as well, but the ability of preferential scattering of higher order resonances are less sensitive to the mentioned two factors than the dipole [89]. This is why we can observe the effect of higher order resonances instead of the dipole.

To evaluate the influence of sphere diameter supporting WGMs on the $Abs_{CIGSe}$ of solar cells, $Abs_{CIGSe}$ for the cells with sphere arrays on top normalized to that without is illustrated in Fig.6.8. The sphere diameter varies from 450 nm where WGMs start to be supported to 1000 nm with a diameter interval of 25 nm. The dark region in the wavelength range of 1050-1150 nm corresponding to a serious $Abs_{CIGSe}$ reduction is due to the interference shift. We can see that it is hard to get $Abs_{CIGSe}$ enhancement over the whole interested spectrum for a single particle diameter. Relatively, the large-sphere array can bring a greater overall $Abs_{CIGSe}$ enhancement.

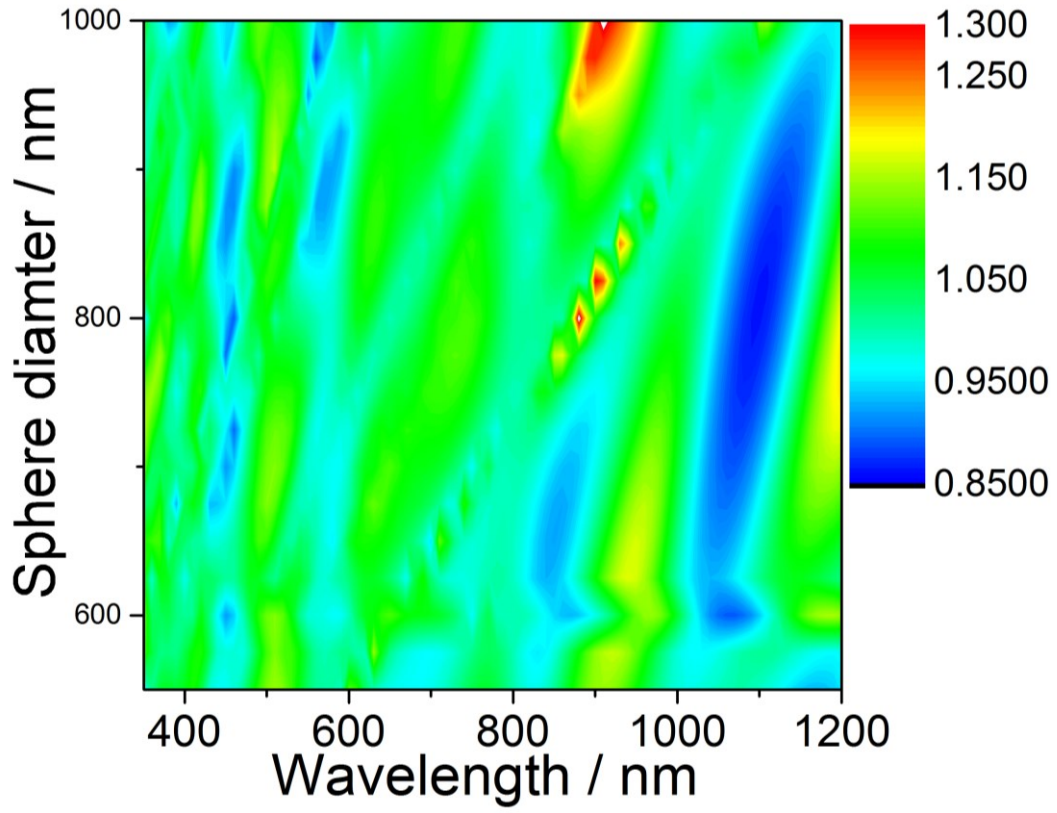


Fig.6.8 Contour image of $Abs_{CIGSe}$ for cells with the presence of spheres in varied size normalized to that without

## 6.1.3 Small sphere array

**An effective anti-reflection layer**

In the investigation above, the focus is on the big $SiO_2$ spheres supporting WGMs and high order multipole resonances. How about smaller spheres? Fig.6.9 presents the influence of the small-diameter ($d$ = 110 nm) $SiO_2$ sphere array on $Abs_{CIGSe}$ and $R$. This size corresponds to the maximum overall photocurrent enhancement. There is an obvious $Abs_{CIGSe}$ enhancement in a broad wavelength range, which arises from the

reduction in $R$. However, the $R$ reduction is mainly ascribed to the close-packed $SiO_2$ spheres forming an effective anti-reflection layer. To verify this, a layer corresponding to the equivalent occupied volume of the spheres and of the same thickness as the diameter of the spheres is assumed and the effective refractive index is 1.30. $R$ for the solar cell with this effective layer is simulated and compared to that with the sphere array in Fig.6.9 b). $R$ from the cell assuming a corresponding effective layer is quite comparable to that from the cell assuming the sphere array on top. This demonstrates that $Abs_{CIGSe}$ enhancement is mainly due to the formation of an effective anti-reflection layer.

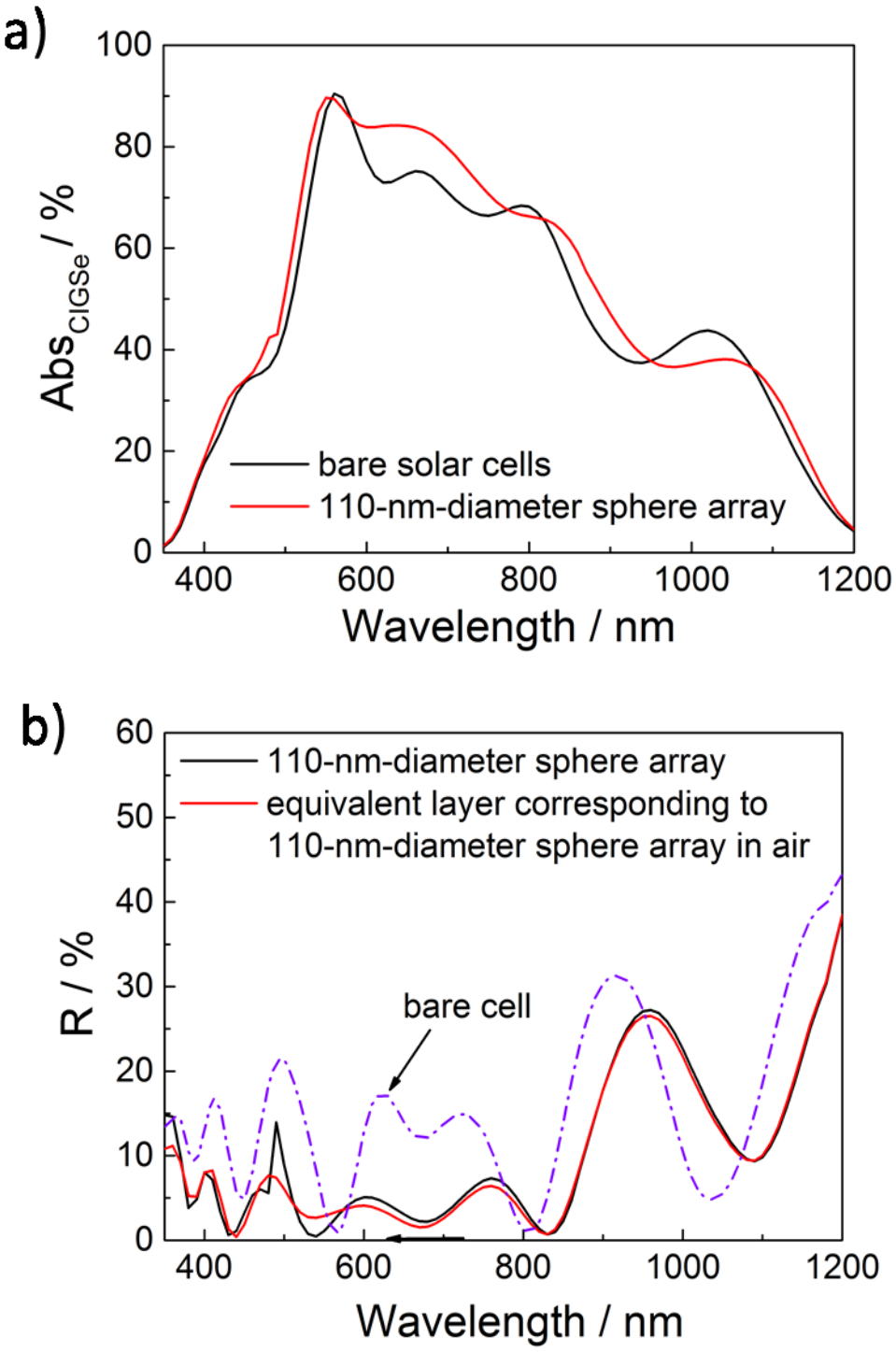


Fig.6.9 a) Comparison of $Abs_{CIGSe}$ without and with the 110-nm-sphere array on top, b) R for the cell with the sphere array on top and with an atop layer corresponding to the refractive index of the sphere array ($n$ = 1.3)

### 6.1.4 Sphere size-dependent photocurrent density enhancement

There are three mechanisms contributing to the light absorption in solar cells from the close-packed sphere array. Fig.6.10 illustrates the working wavelength ranges of the three mechanisms. They are the formed effective anti-reflection sphere layer, WGMs and higher order mutipole resonances. To determine the influence of sphere diameters on the overall $Abs_{CIGSe}$ enhancement, the integrated photocurrent density enhancement is plotted as a function of sphere diameters in Fig.6.11. The sphere diameter varies from 40 to 1000 nm. The small spheres dominate the light trapping effect by the effective anti-reflection layer, which can cover a broad wavelength range. For large spheres, WGMs can be supported but only in a narrow wavelength range. High order multipole resonances are also be supported in the short wavelength range, which is mainly within the parasitic absorption range of the AZO/ZnO/CdS layers. Accordingly, we can readily understand that the maximum photocurrent density enhancement reaching 1.60 $mA/cm^2$ is at 110-nm-diameter sphere array. As the size of large sphere further increases, the resonant wavelength range can go beyond the parasitic absorption range of the AZO/ZnO/CdS layers. This is mainly why the photocurrent density enhancement generally improves as the sphere size increases from 400 to 1000 nm.

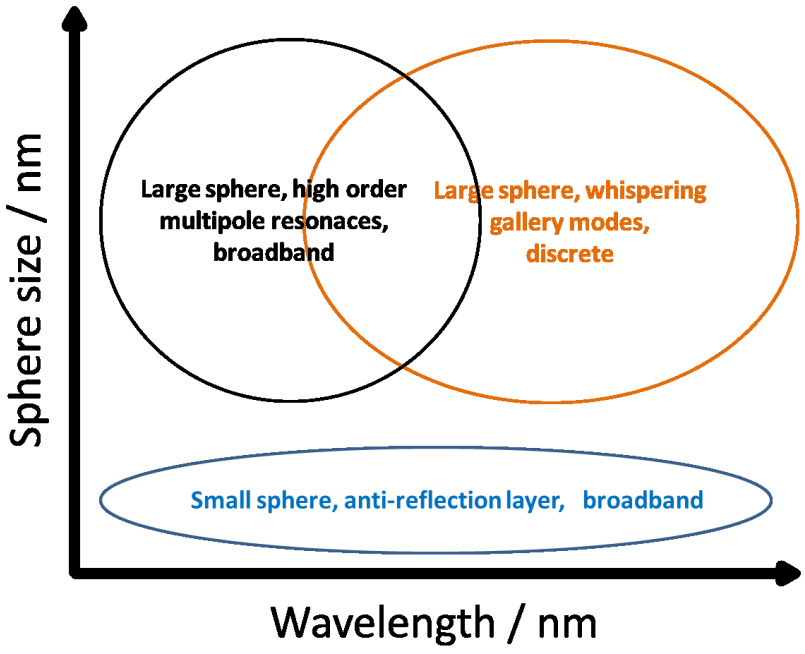


Fig.6.10 Illustration of the working wavelength ranges and sphere sizes of the anti-reflection effect, whispering gallery modes and high order multipole resonances

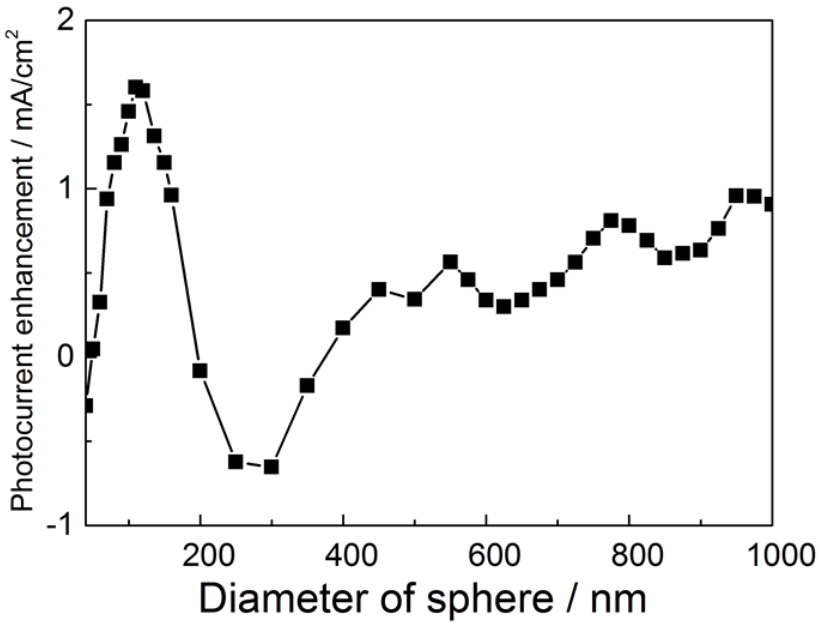


Fig.6.11 Photocurrent enhancement of solar cells dependence of the diameter of $SiO_2$ sphere

Above, the influence of the $SiO_2$ sphere was investigated thoroughly. The refractive index of $SiO_2$ is $n$ = 1.46. How about the sphere with a higher refractive index, for example $n$ >2? Actually, this is not favourable, because that sphere arrays with a larger refractive index tend to couple more light backward to the free space rather than forward to the solar cells than the $SiO_2$ sphere arrays. For the small-diameter sphere array, it cannot serve as an effective anti-reflection layer since the effective refractive index doesn't fulfill the criteria of the square root of the media at the interfaces. Conclusively, the sphere array with a lower refractive-index material favours the light absorption enhancement of ultra-thin CIGSe solar cells more than the higher refractive-index sphere array.

## 6.2 Experimental verification

Since $SiO_2$ sphere arrays with a lower refractive index were numerically confirmed to favour the light absorption in the ultra-thin solar cells, in this section, the $SiO_2$ nanosphere arrays will be prepared on the top of ultra-thin CIGSe solar cells and the light-trappling effect will be experimentally verified and compared to the simulation results.

### 6.2.1 Preparation

**Solar cell**

For experimental verification of the influence of $SiO_2$ sphere arrays on cells, ultra-thin CIGSe solar cells were prepared. Because of the poor device quality for the 300-nm-thick CIGSe cells, the experimental CIGSe layer is 460 nm thick with a Ga/[Ga+In] ratio of 0.35. The CdS thickness was reduced to around 50 nm to favour the $Abs_{CIGSe}$ enhancement arising from high-order multipole resonances. The thicknesses of other layers are kept the same as in the simulations.

**2-D $SiO_2$ sphere array**

From the experimental point of view, preparing 2-D nanosphere arrays is a main challenge. The preparing methods are including lithography, spin coating, electrophoretic assembly, vertical deposition et.al. In this work, Langmuir-Blodgett (LB) is applied to prepare the 2-D sphere array for its simplicity [95]. The colloidal $SiO_2$ plain spheres without any chemical group around spheres are purchased from the company (micro particles GmbH, Berlin). The preparation process of 2-D $SiO_2$ sphere arrays is as follows:

1) Suspend the $SiO_2$ spheres in Butanol and homogeneously dispersed by sonication.
2) Submerge the solar cell under water in a petri dish.
3) Drop the sphere suspension onto the surface of Air/Water. The suspension will spread out on the water surface. The spheres rest on the surface in seconds after Butanol evaporates. Keep adding the suspension until the surface is completely covered by the spheres. At the moment, the closely packed 2-D monolayer forms.
4) Use an injector and suck off water. The formed 2-D $SiO_2$ sphere array rests on the surface of solar cell when the water level is below the height of solar cell.

For more details regarding the preparation, please refer to [95]. This is a very simple approach to prepare closely packed 2-D sphere arrays. In my experiments, the area of the petri dish is only $5*5cm^2$, but this technology can be easily scaled to module dimensions. The sphere sizes of $d$ = 120 nm, 600 nm are experimentally chosen because they corresponds to the small sphere arrays with the effective anti-reflection layer and large sphere arrays with WGMs from the simulations above. Fig.12 a1, b1 show the $SiO_2$ sphere array of $d$ = 120 nm, 600 nm on top of CIGSe solar cells, respectively. The spheres are generally hexagonally close-packed and form a monolayer, though a 5-10

nm distance gap between some spheres is observed mainly due to the influence of surface roughness. This implies that the method used is a reliable approach to prepare 2-D closely packed $SiO_2$ sphere arrays.

## 6.2.2 Comparison of experiment and simulation

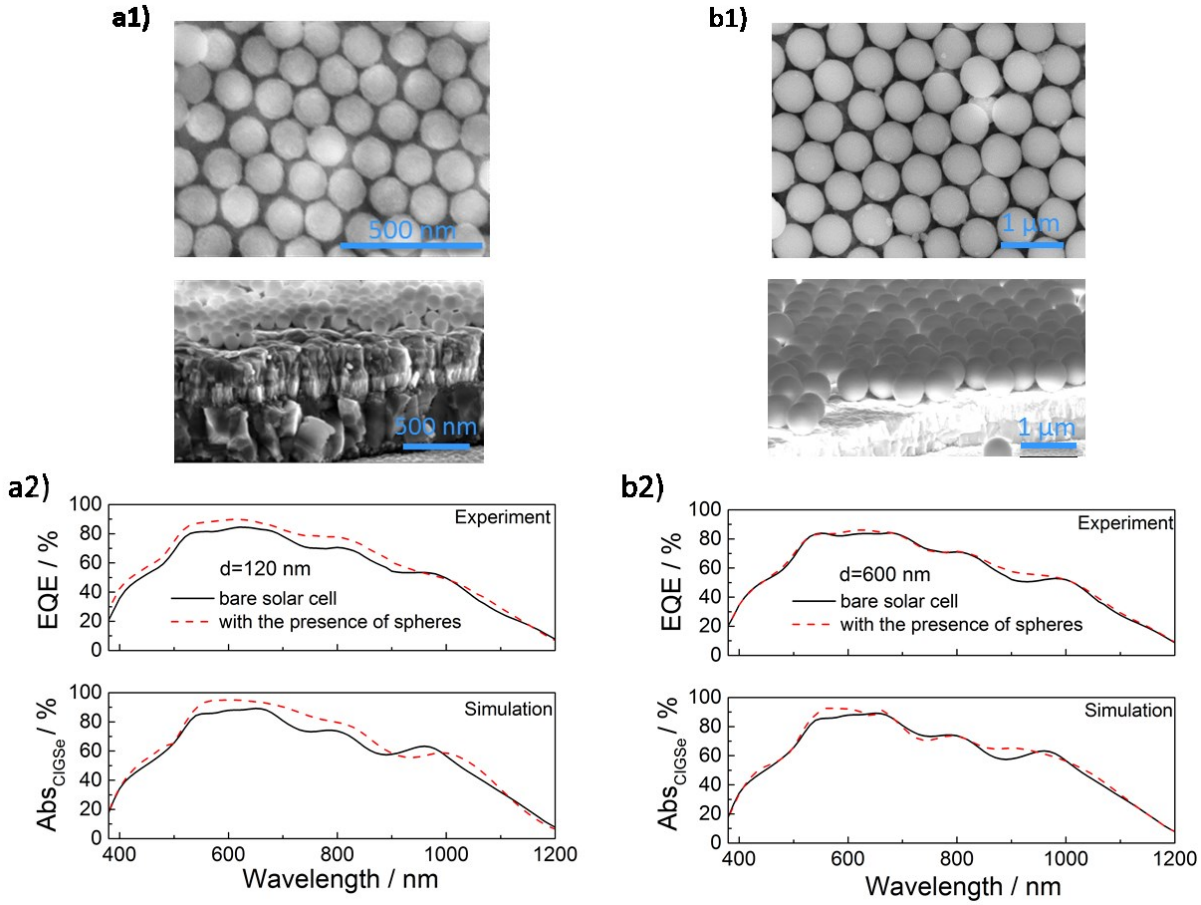


Fig.6.12 SEM images of $SiO_2$ sphere array with sphere diameter a1) 120 nm and b1) 600 nm in top and cross views; comparison of both experimental *EQE* and simulated $Abs_{CIGSe}$ for the cells without and with a2) 120-nm-diameter sphere array and b2) 120-nm-diameter sphere array

Simulations have shown that a 5-10 nm gap between spheres barely influence the optical responses of cells in contrast to the ideally closely-packed spheres. The *EQE* curves of solar cells were characterized before and after coating the $SiO_2$ sphere arrays, which are depicted in Fig.6.12. The corresponding simulated $Abs_{CIGSe}$ curves are also attached. Firstly, it should be mentioned that the simulated $Abs_{CIGSe}$ is generally higher than the corresponding measured *EQE*, this is due to the carrier collection loss. Besides, the interface roughness, the narrow size distribution of the experimental $SiO_2$ spheres

and thickness deviations between the experimental samples and the simulated are not considered for reducing the calculation effort. All those factors will lead to deviations between the simulated $Abs_{CIGSe}$ and experimentally measured *EQE*. Nevertheless, the changing trends for both the experimentally measured *EQE* and the simulated $Abs_{CIGSe}$ agree quite well after coating the 2-D sphere array for all the three sphere sizes. It proves that our simulation is highly reliable to predict the influence of the sphere array on the optical responses of cells. The integrated photocurrent density enhancement from *EQE* can reach 2.19 mA/cm$^2$ provided by the 120-nm-diameter sphere array and 0.46 mA/cm$^2$ by the 600-nm-diameter sphere array, which corresponds to an relative increase of 8.4% and 1.6% compared to the cells without the presence of spheres. The corresponding photocurrent density enhancements from the simulation are 2.17 mA/cm$^2$ and 0.7 mA/cm$^2$ showing great comparability to those from experimental *EQE*.

## 6.3 Conclusion

It has been both experimentally and theoretically investigated the light-trapping effect of ultra-thin CIGSe solar cells using closely packed $SiO_2$ sphere arrays. For large spheres, it is demonstrated that whispering gallery modes can enhance the light absorption for CIGSe cells and dominate the absorption enhancement mechanism. Whereas the high order multipole resonances of large spheres, which can benefit the light absorption in crystalline Si solar cells, are confirmed to barely enhance the effective absorption in the CIGSe layer. Small spheres are also proved to be able to enhance the light absorption due to the formation of an effective anti-reflection layer. Because the formed anti-reflection layer can work in a much broader wavelength range than WGMs, the maximum absorption enhancement is achieved for the small spheres with a diameter of 110 nm. Finally, the simulations were experimentally confirmed.

# Chapter 7

# Light trapping by $SiO_2$ dielectric nanostructures at the interface of CIGSe/Mo for ultra-thin $CuIn_{1-x}Ga_xSe_2$ (CIGSe) solar cells

Using the sub-wavelength metallic nanoparticles as the light-trapping elements have been extensively investigated in solar cells, in most cases the underlying enhancement is the great scattering ability including big scattering cross sections induced by the localized surface plasmons. However, due to the thermal instability and parasitic absorption of the metallic nanoparticles analyzed in chapter 5, the successful applications of plasmonic metallic structures for light trapping in CIGSe solar cells faces a great challenge and have been seldom reported. As stated in chapter 6, the wavelength-scale dielectric particles can feature great scattering cross sections and large scattering angular ranges as well via Mie resonances. Also as discussed in chapter 4 and confirmed in chapter 6, light-trapping effects from the surface will be inevitably attenuated and even possibly worsen the $Abs_{CIGSe}$ due to the parasitic absorption in $Abs_{AZO/ZnO/CdS}$. In this work, the dielectric light-trapping structures at the interfaces within CIGSe solar cells are therefore focused. For maintaining the scattering angles to the maximum extent and reducing the possible increase of parasitic absorption in other layers, the interfaces touching the CIGSe layer (CdS/CIGSe and CIGSe/Mo) are preferred. Compared to the critical p-n junction interface of CdS/CIGSe, the interface of CIGSe/Mo is selected for the consideration of stable electrical properties of solar cells.

## 7.1 Material determination of dielectric nanoparticles in the CIGSe solar cells

The scattering properties of the particles are dependent on the surrounding media with varied refractive indexes. Unlike the plasmonic materials that the refractive indexes are normally lower than the surrounding media, actually, there are two cases of refractive-index contrast between the particles and surrounding media for dielectric materials: 1) the particles have higher refractive indexes than the surrounding media; 2) the particles

are lower than the surrounding media in refractive index. Considering the refractive indexes of surrounding media (CIGSe, $n$ = 2.5-3; Mo, $n$ = 2.2-3), it is easy and realistic to fulfill the case of a lower refractive index of the particles than the surrounding media.

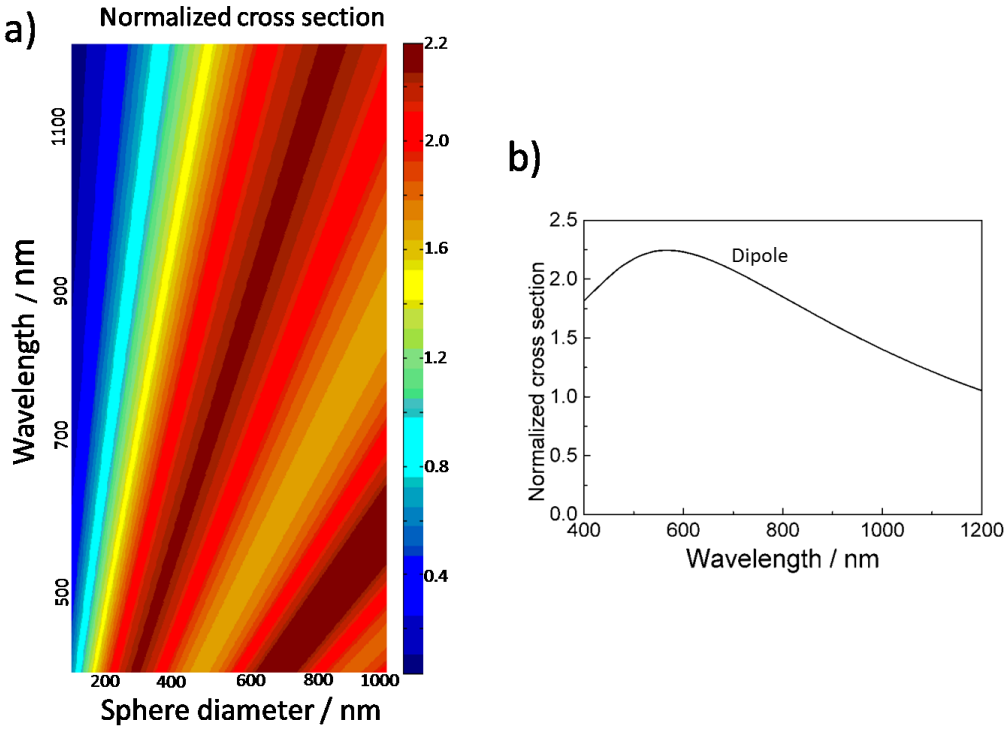


Fig.7.1 a) Contour image of the scattering cross-section (normalized to geometrical cross section) of a sphere ($n$ = 2, $k$ = 0) in the medium ($n$ = 3, $k$ = 0); b) scattering cross-section spectra for the 400-nm-diameter sphere

Fig.7.1 plots scattering properties of a nanoparticle in a homogeneous media in the case: the refractive index of the sphere ($n$ = 2, $k$ = 0) is lower than that of the surrounding medium ($n$ = 3, $k$ = 0). When the size is beyond 400 nm in diameter, the scattering cross-section can exceed the geometrical cross-section overall the whole spectra of interest (400–1200 nm). Besides, it can be observed that the maximum cross section is more than 2 times larger than the geometrical cross section. The wavelength for the maximum scattering cross section is nearly linearly proportional to the diameter of the sphere. Besides, the resonance for the sphere in the medium with a higher refractive index is quite broadband. This is confirmed by the example of a 400-nm-diameter sphere in Fig.7.1b: the dipole covers almost the whole spectrum of interest. Actually, the broadband resonance is quite desirable for the requirement of broadband absorption enhancement in solar cells.

Regarding the materials of dielectric nanostructures, the first requirement is that the materials should be thermally stable, which can bear the deposition temperature of CIGSe layer and don't react with the CIGSe layer or inter-diffuse. In my work, the CIGSe deposition temperature is 440 °C. Therefore, the normal organic materials are not possible and stable inorganic oxides are preferred. Another concerning point is related to the contrast extent of refractive indexes between the dielectric particles and surrounding media. To figure out the influence of refractive-index contrast, Fig.7.2 further simulates the scattering cross-section spectra of a 400-nm-diameter sphere in varied refractive indexes but less than the surrounding medium ($n = 3$, $k = 0$). We can observe that the higher the refractive-index contrast is, the larger the cross section is and the broader the resonance peak is. Mann [96] also observed the similar trend. For the material of nanoparticles, it is better if the particles have a lower refractive index. Considering the difficulty of experimentally preparing nanoholes at the interface of CIGSe/Mo interface, $SiO_2$ is taken as the particle material, which has the lowest refractive indexes (around 1.5) among the commonly used inorganic dielectric materials as well as a good thermal stability.

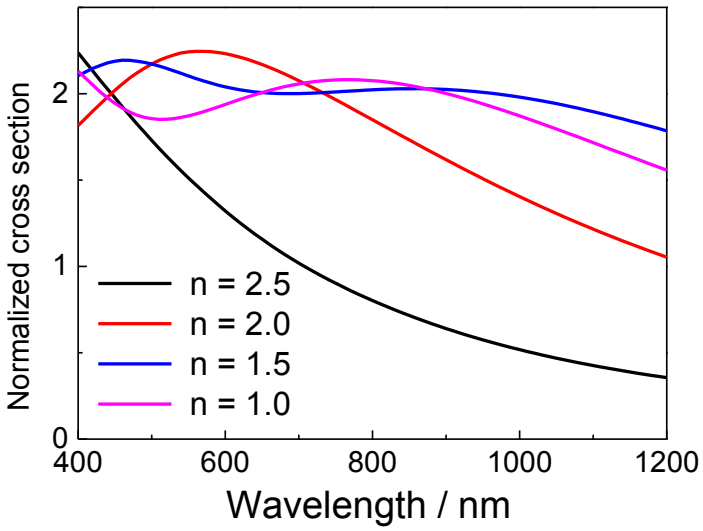


Fig.7.2 Normalized cross-section spectra of a sphere in the homogeneous medium ($n = 3$, $k = 0$) dependent on the refractive index of the sphere

Whether the incorporation of $SiO_2$ light-trapping nanostructures is compatible with the growth and the electrical properties of cells is not experimentally verified. How much of absorption can be enhanced also needs to be identified. In this chapter these possible issues will be investigated. In the following, the preparation of $SiO_2$ dielectric nanostructures is elaborated first, then the incorporation of $SiO_2$ dielectric

nanostructures into the ultra-thin CIGSe solar cells is investigated both experimentally and theoretically and detailed analysis is given as well.

## 7.2 Fabrication of $SiO_2$ dielectric nanostructures*

Fabrication of nanostrucutres for various applications is always a challenge. Every approach has its advantages and disadvantages. In this work, the substrate conformal imprint lithography (SCIL) [97] (developed by Philips Research and SUSS MicroTec) is employed based on the replication of a mask pattern formed by a stamp. This preparation method attracts tremendous attentions because of the features of high resolution (up to 20 nm), high throughput and large-scale preparation. Further, this method can prepare nanoparticles on the rough surfaces by using a soft and thin high-Yong, modulus X-PDMS stamp, which can not only avoid collapse and sticking of nanostructures, but also maintain a conformal contact between the stamp and sample surface. This greatly widens its implication because contamination and surface roughness are frequently present on the sample surfaces. Therefore, SCIL is an appropriate approach for fabricating the dielectric nanostructure for solar cells and is taken for fabricating $SiO_2$ nanostructures in this work. In the following, steps of an exemplary SCIL process [98] will be elaborated and schematically shown in Fig.7.3. Prior to the official steps, sample surfaces are cleaned by rinsing in i-PrOH and then drying by $N_2$.

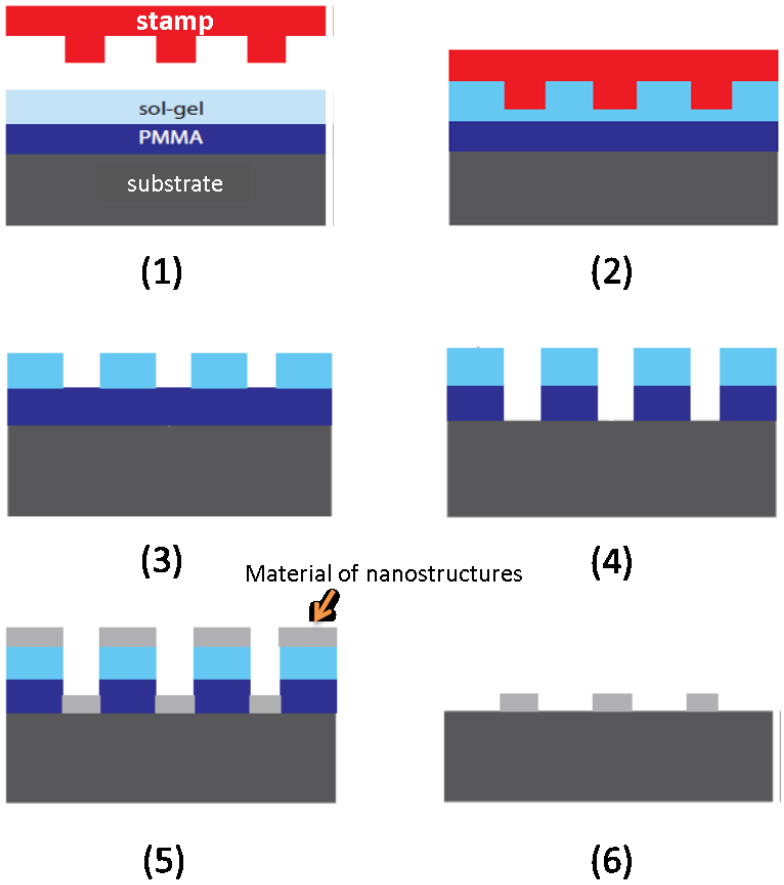


Fig.7.3 Schematic outline of fabrication steps for preparing nanostructures via substrate conformal imprint lithography (SCIL) [98]

(1) The sample is completely covered by PMMA using spin-coating. Afterwards, the PMMA layer is baked in air. This can make PMMA solidify and insoluble in the following sol-gel layer. Subsequently, the silica sol-gel is spin-coated with a thickness of 70 nm. The sol-gel contains two liquid alkoxide precursors of tetramethylorthosilicate (TMOS, $Si(OCH_3)_4$) and methyltrimethoxysilane (MTMS, $C_4H_{12}O_3Si$) in alcohol and water. The Si-O-Si network can form mainly due to the hydrolysis and condensation reaction. Water and alcohol can evaporate during the spin coating process.

(2) The soft PDMS stamp containing the nanopillars is molded in the sol-gel layer. After resting 20 min. at room condition in air, lift off the stamp. The corresponding holes are present in the residual sol-gel layer. An anisotropic RIE process is done to remove the residual sol-gel layer using a mixed gas of $CHF_3$ and Ar.

(3) The holes are transferred to PMMA layer after keeping etching by a low-bias $O_2$ RIE process. This process is deliberately done in a longer time to completely etch away the PMMA in the holes. This can benefits the final lift-off of the residual layers.

(4) The desired materials are deposited on top. For this experiment, $SiO_2$ is evaporated by e-beam.

(5) This is the final step of lifting off, which is carried out by dissolving the PMMA in 50 °C Acetone and followed by i-PrOH rinse and $N_2$ blowing. As a result, an array of nanoparticles rests on the surface of samples.

It should be mentioned that only i-PrOH and acetone are the only used solvents, which are not chemically active to the Mo back contacts. Fig.7.4 a shows the SEM image of the top view of $SiO_2$ nanostructures on Mo back substrate. The particles are tapered, which is not conformal to the cylinder shape of the stamp. This is mainly due to that the evaporation process fails to fill the cylinder holes completely. Besides, the particles are completely separated between each other and periodically aligned, the surface is pretty clean without any residual organic materials. From the photography image on the 2.5*2.5 cm Mo substrate in Fig.7.4 b, it can be seen there is small area absent of nanoparticles (dark part), this is mainly due to the imperfection of the stamp. Nevertheless, most part of the substrate is covered by the $SiO_2$ nanoparticles. The geometry of the experimental $SiO_2$ nanostructure is 205 nm in radius, 210 nm in height and 513 nm in pitch. So it can be concluded that SCIL is a reliable approach for fabricating the $SiO_2$ dielectric nanostructures on Mo.

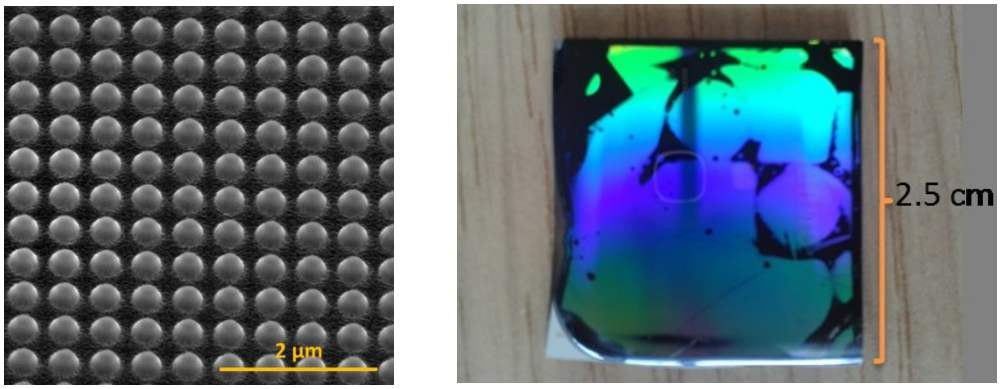


a) b)

Fig.7.4 a) SEM image of $SiO_2$ nanostructures on Mo substrate and b) the photography of nanostructures on the 2.5*2.5 cm Mo substrate [98]

## 7.3 Incorporation of $SiO_2$ dielectric nanostructures into ultra-thin CIGSe solar cells

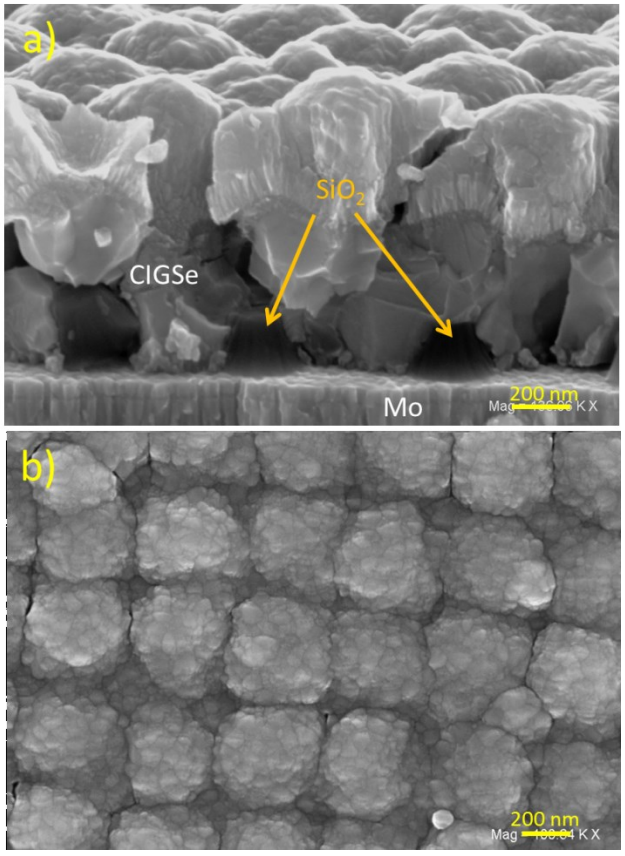


Fig.7.5 a) Cross section of the complete solar cell with $SiO_2$ nanoparticles at the interface of CIGSe/Mo; b) topography of the complete solar cell

To experimentally investigate that the ultra-thin CIGSe solar cells are able to survive on the $SiO_2$ dielectric-nanostructure-coated Mo substrates and achieve absorption enhancement arising from the scattering of the nanostructures, solar cells were prepared on top with a CIGSe thickness of around 460 nm and Ga/[III] of 0.35. For comparison, solar cells on bare Mo substrates without $SiO_2$ nanostructures were prepared simultaneously.

It can be observed that the layers on top of the $SiO_2$ nanostructure have a conformal growth layer by layer. The CIGSe layer is closely wrapping the $SiO_2$ particles and fills up the gaps between the particles, which implies a good electrical contact. It should be stressed here that the $SiO_2$ particles reduce the contacting area between the CIGSe layer and the Mo back contact, this however will not negatively influence the carrier (hole) collection, because the geometry scale of the experimental $SiO_2$ nanoarray (205 nm in

radius, 210 nm in height and 513 nm in pitch) is within the range of diffusion length (500-1000 nm) of holes in CIGSe solar cells [99]. Regarding whether $SiO_2$ particles can bring effective interface defects and increase the carrier recombination, this should be checked from the cell performance.

a)

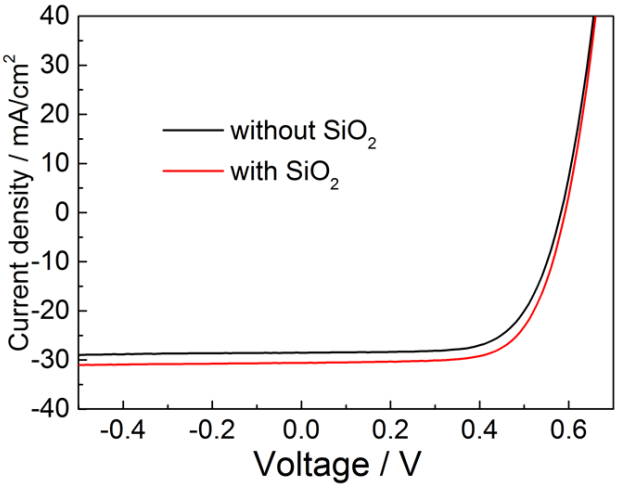


b)

| sample | *Voc* (mV) | $J_{sc}$ (mA/cm$^2$) | *FF* (%) | *Eff.* (%) | $J_{sc}$ from EQE (mA/cm$^2$) |
|---|---|---|---|---|---|
| bare cell | 583 | 28.6 | 67.4 | 11.2 | 28.2 |
| with $SiO_2$ at CIGSe/Mo | 592 | 30.6 | 68.2 | 12.4 | 30.5 |

Fig.7.6 a) *J-V* curves of solar cells with and without the $SiO_2$ nanostructure, b) *J-V* parameters extracted from corresponding curves

Fig.7.6 shows the *J-V* performances of the solar cells with and without the $SiO_2$ nanostructure averaged from 6 cells. All the parameters for cells with $SiO_2$ are better than those without, which indicates that the $SiO_2$ particles at least do not bring obvious negative electrical effects for the performance of cells. Remarkably, the short current density ($J_{sc}$) is obviously enhanced from 28.6 to 30.6 mA/cm$^2$, which confirms that the $SiO_2$ nanostructure can enhance the absorption in the CIGSe layer. The details will be analyzed in the following. The $V_{oc}$ and *FF* slightly increase from 583 to 592 mV and 67.4 to 68.2 %, respectively. Whether the increase is due to the increase of $J_{sc}$, or the back passivation effect of $SiO_2$ nanostructures, this needs further confirmation. As a

result, the efficiency is greatly improved to 12.4 %, which corresponds to an enhancement of 10.7 % compared to the cells without $SiO_2$.

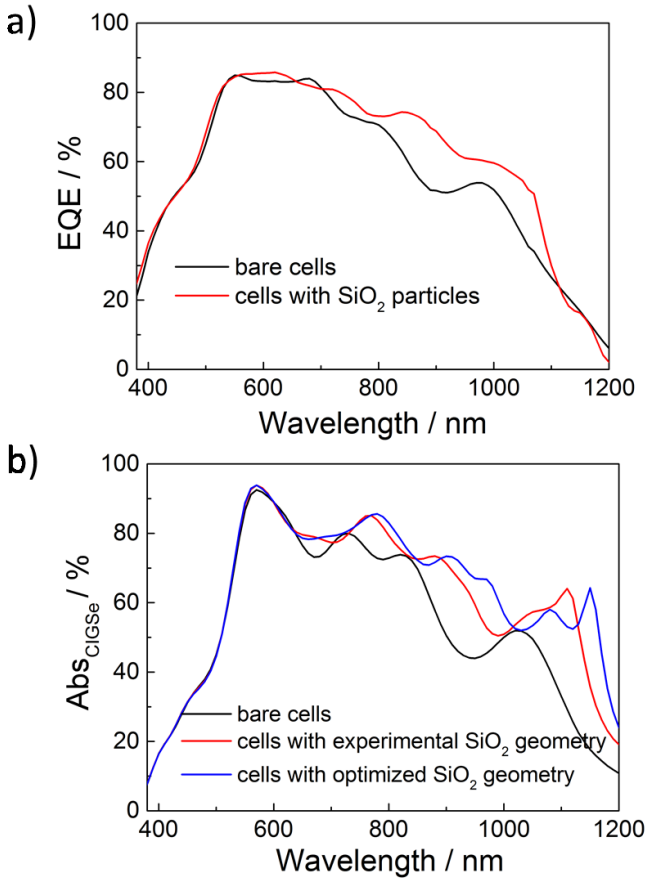


Fig.7.7 Comparison of a) experimental *EQE* and b) simulated $Abs_{CIGSe}$ between cells with and without the $SiO_2$ nanostructure at the interface of CIGSe/Mo

To further identify how the $SiO_2$ nanostructure influences the light absorption in cells, EQE were measured in Fig.7.7 a). In the wavelength range of 400-700 nm, there is nearly no change in the *EQE* for the cells with and without $SiO_2$, which shows the surface roughness arising from the conformal growth has no effect on this wavelength range. In the infrared range, where the light is not poorly absorbed in the CIGSe layer, the *EQE* is significantly enhanced. This results from that the $SiO_2$ nanostructures can effectively scatter back the unabsorbed light into the CIGSe layer and reduce the light intensity hitting on Mo. For the theoretical confirmation, theoretical 3-D simulations were carried out and shown in Fig.7.7 b). The simulations were done by the software package Finite Difference Time Domain (FDTD) [100] *. The conformal growth of the layers is not considered in the simulations. The CIGSe layer thickness of the cells with

$SiO_2$ was increased to compensate for the volume of the $SiO_2$ particles and keep the absorber volume the same for cells with and without $SiO_2$. All the optical constants and thicknesses are kept the same as the simulations in chapter 6, for more simulation details, please refer [101]. Comparable to the *EQE* measurement, the simulations exhibit no optical effect on the cell below the wavelength of 700 nm and a substantial broadband enhancement beyond 700 nm. There is a remarkable absorption enhancement peak around 1100 nm, which is attributed to the wave-guided modes. Actually, the geometry of the $SiO_2$ nanostructures can be further optimized (250 nm in radius, 250 nm in height, 550 nm in pitch) and the corresponding $Abs_{CIGSe}$ curve (blue) is also shown in Fig.7.9 b). It can be seen that the optimized $SiO_2$ structure has an overall better absorption enhancement. It is noted, in the wavelength range of 1000-1200nm, the enhancement for the *EQE* is not as obvious as the simulated. Two reasons possibly contribute to the deviation: 1) the simulated $Abs_{CIGSe}$ is always higher than the corresponding *EQE* due to the presence of the collection loss; 2) the inputting optical constants for simulations aren't exactly the same as the experimental, which can bring certain deviations in the simulations. Nevertheless, since the changing trend of the *EQE* curves between the cells with and without the $SiO_2$ nanostructure is quite comparable to that of the simulated $Abs_{CIGSe}$, it is concluded that the simulations are reliable to predict the influence of the nanostructures. As to the $J_{sc}$ difference between *J-V* measurement and *EQE* integration, this is mainly attributed to the area deviations of the scribed solar cells.

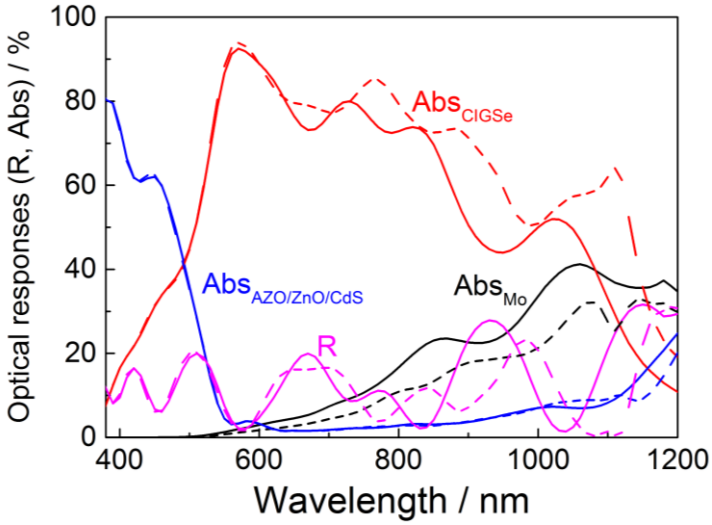


Fig.7.8 Comparison of simulated optical responses (R, Abs) of cells with and without the $SiO_2$ nanostructure at the interface of CIGSe/Mo

Though $J_{sc}$ is improved beyond 30 mA/cm$^2$ by incorporating the $SiO_2$ nanostructure at the interface of CIGSe/Mo, there is still a big gap compared to the $J_{sc}$ (approx. 35 mA/cm$^2$) of thick solar cells. To further identify where the optical loss is, the optical responses of the whole solar cell with (solid lines) and without (dashed lines) the experimental $SiO_2$ nanostructure were compared and depicted in Fig.7.8. As analyzed in chapter 4, the parasitic $Abs_{Mo}$ and $R$ are the main optical losses needing to be cursed. After integrating the $SiO_2$ nanostructure, simulations show that both $Abs_{Mo}$ and $R$ are overall reduced. $Abs_{Mo}$ is greatly lowered. However, the parasitic $Abs_{Mo}$ and R are still significant. Therefore, for achieving the goal of a comparable or even better $J_{sc}$ to that of thick cells, further reducing $R$ and $Abs_{Mo}$ is still required. For $R$ reduction, this can be realized by coating an anti-reflection layer. It was already proved in chapter 6, a 120-nm-diameter $SiO_2$ array on top of cells can act as an effective anti-reflection layer. This nanosphere array was prepared on the cells having $SiO_2$ nanostructures at the interface of CIGSe/Mo. The *EQE* and *J-V* results are shown in Fig.7.9. After coating the anti-reflection layer, the Fabry-Perot interferences in the *EQE* curve disappear and there is further improvement almost over the whole spectrum of interest. The resulting integrated $J_{sc}$ is 32.1 mA/cm$^2$, which corresponds to an enhancement of 3.9 mA/cm$^2$ compared to that of bare cells. The increased $J_{sc}$ also contributes a little to the $V_{oc}$ and *FF* and results in an efficiency of 13.1% from the *J-V* measurement, which corresponds to an enhancement of 17.0 % compared to the bare solar cells. It is noted that the $J_{sc}$ value from the *J-V* measurement is less than that integrated from *EQE*, this is mainly due to that the anti-reflection layer does not completely cover the whole cell for protecting the front contact for measurements. If $J_{sc}$ integrated from the *EQE* is used, the net efficiency is expected to be further improved.

Though the presence of the $SiO_2$ nanostructure can reduce the light hitting on Mo and the parasitic $Abs_{Mo}$, $Abs_{Mo}$ is still not negligible. For further $Abs_{Mo}$ reduction, replacing the Mo back contact by transparent conductive oxide (TCO) back contact is an approach. The unabsorbed light can transmit out of solar cells and be utilized by a rear reflector without the concern of serious parasitic absorption. Unfortunately, the solar cells on TCO don't electrically perform as well as on Mo, the improvement of the electric performance of solar cells on TCO is therefore critical for further efficiency enhancement.

a)

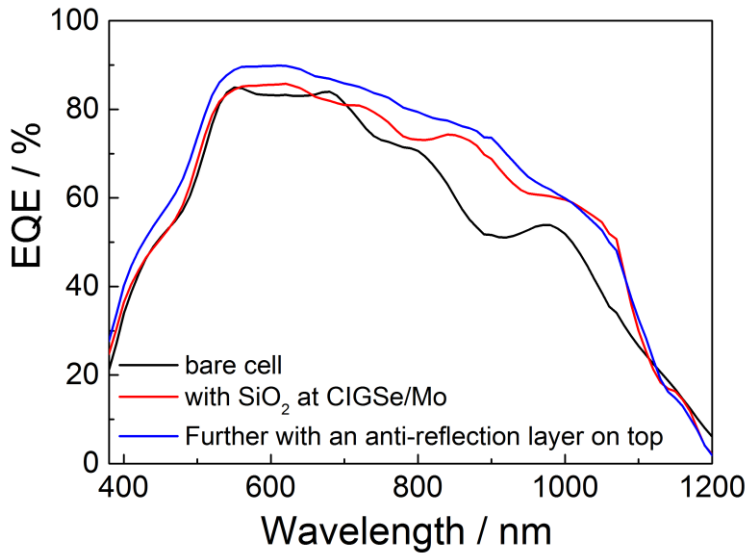


b)

| sample | $V_{oc}$ (mV) | $J_{sc}$ (mA/cm$^2$) | *FF* (%) | *Eff.* (%) | $J_{sc}$ from EQE (mA/cm$^2$) |
|---|---|---|---|---|---|
| without $SiO_2$ | 583 | 28.6 | 67.4 | 11.2 | 28.2 |
| Further with the anti-reflection layer | 600 | 31.6 | 68.9 | 13.1 | 32.1 |

Fig.7.9 Overview of a) *EQE* curves and b) *J-V* parameters among cells with and without $SiO_2$ light-trapping structures

## 7.4 Conclusion and Outlook

In this chapter, we have investigated the light-trapping effects of $SiO_2$ nanostructures at the interface of CIGSe/Mo on ultra-thin CIGSe solar cells. It is experimentally confirmed that $SiO_2$ nanostructures at the CIGSe/Mo interface are compatible with the growth of solar cells on top and barely influence the electrical performance of solar cells. Remarkably, $Abs_{CIGSe}$ is greatly enhanced due to the back-scattering of $SiO_2$ nanostructures and $Abs_{Mo}$ is significantly reduced. This is proved by the 3-D theoretical FDTD simulation as well as the experimental $J_{sc}$ and *EQE* improvement. $J_{sc}$ is greatly improved from 28.6 to 30.6 mA/cm$^2$ (from *J-V* measurement) and is mainly due to the $Abs_{CIGSe}$ enhancement in the long wavelengths (shown from *EQE* measurement), where light is poorly absorbed by the ultra-thin CIGSe absorbers. To my best knowledge, this is the first time that $J_{sc}$ is reported to be beyond 30 mA/cm$^2$ for ultra-thin CIGSe solar cells without an anti-reflection layer. For further $Abs_{CIGSe}$ and $J_{sc}$ enhancement, R is

suppressed by the anti-reflection layer of a close-packed 120-nm-diameter sphere array and the resulting $J_{sc}$ is increased to 31.6 mA/cm$^2$.

However, the parasitic $Abs_{Mo}$ is still significant even at the presence of the $SiO_2$ nanostructures and hinders the further improvement of $J_{sc}$. Though replacing the typical Mo back contact by TCO is an approach to reduce the parasitic absorption in back contact, CIGSe solar cells on TCO substrate don't electrically perform well due to the serious back recombination at the CIGSe/TCO interface. Therefore, the next step is to improve the electrical performance of CIGSe solar cells on TCO back contacts. The nanostructures can reduce the contacting area between CIGSe and TCO back contacts and may have the potential to reduce the back recombination as well, this needs to be further checked. Besides, $Al_2O_3$ material is experimentally discovered to be able to reduce the back recombination by repelling the electrons far away from the back contacts [84]. It will be promising that the $Al_2O_3$ nanostructures may improve the ultra-thin CIGSe solar cells both electrically and optically, which is worth experimental investigation in next step.

* *Clarification: The work in this chapter was cooperated with Claire van Lare and Albert Polman (the group of photonic materials, Amolf, the Netherland). The parts of preparing $SiO_2$ nanostructures and simulations were done by them. For more details, please refer to Ref. [101]*

# Chapter 8

# Summary

The ultimate goal of this work is to obtain ultra-thin (CIGSe absorber thickness below 500 nm) CIGSe solar cells with a comparable or even better performance to the typical thick counterparts. This allows a significant drop in material consumption (eg. In) and a resulting reduction in manufacturing cost. Back recombination and incomplete absorption are the two main factors hindering the achievement of high efficiencies for ultra-thin CIGSe solar cells. In this work, the initial work is done related to solving the two hindering factors in this thesis, with the main focus on the incomplete absorption. In the following, I will summarize what I have done, achieved and provide some prospects for further investigations.

To begin with, bare ultra-thin solar cells are a firm basis for further performance improvement. Therefore, the work started preparing highly efficient bare ultra-thin solar cells, this is the main content of Chapter 2. To reduce the back recombination for ultra-thin solar cells, a low substrate temperature (440 °C) was applied for ultra-thin absorber deposition using 3-stage co-evaporation process, since the low substrate temperature could reduce the inter-diffusion of Ga-In and create a high back Ga grading by preventing the intentional deposition sequence of Ga-Se prior to In-Se. *It was discovered that ultra-thin solar cells grown at the low substrate temperature were performing overall better than those at high temperature mainly in terms of much higher* $J_{sc}$. This was proved to be due to the joint effect of a reduction of back recombination and an improved absorption ability in long wavelengths both arising from a higher back Ga grading. The low substrate temperature not only provided the possibilities for the depositions on flexible substrates but also was possibly favourable to the thermal stability of incorporated light-trapping nanostructures. The efficiencies of bare ultra-thin CIGSe solar cells were reported in the range 10-12 % in the whole thesis. Actually, there is still much scope for further improvement. Since the work here concentrated more on the incomplete absorption, further optimization of bare ultra-thin CIGSe solar cells was not done yet.

To overcome the incomplete absorption of bare ultra-thin CIGSe solar cells, light-trapping structures are necessarily demanded. For the effective implementation of light-trapping structures, theoretical optical simulations are needed for experimental guidance. Optical constants are the basic and indispensable input parameters for the optical simulations and their accuracies determine the reliabilities of the optical simulations. In Chapter 3, Transfer-Matrix method was employed to extract the optical constants of each layer (except Mo) in the CIGSe solar cell structure based on *T/R* and thickness measurements. The special focus was on CIGSe absorber layers since they determine the optoelectric properties to a great extent. *In the optical-constant extracting process, Transfer-Matrix method was modified based on the scalar scattering theory and the surface roughness was taken into account.* It was discovered that the accuracies of the optical constants were improved especially for refractive indexes (*n*). *Further, the influence of substrate temperature was investigated as well, finding that low substrate temperature can lead to a higher extinction coefficient (k) in the long wavelengths for CIGSe layers. Finally, a database containing the optical constants of each layer in the CIGSe solar cell and a sub-database of optical constants of CIGSe layers with varied [Ga]/[III] ratios were established and ready for the optical simulations.*

Prior to the implementation of light-trapping structures, Chapter 4 concentrated on the identification of optical losses of ultra-thin CIGSe solar cells by comparing to their thick counterparts. *It was confirmed that the parasitic $Abs_{Mo}$ was largely increased and was the main optical loss: $Abs_{Mo}$ only accounts 2.5 % of the incident light in the form of energy for the solar cell with a 2-μm-thick CIGSe absorber, whereas this ratio is 18.9 % for the solar cell with a 300-nm-thick CIGSe absorber.* Straightly after the loss identification, the anti-reflection and large angular scattering effects on the surface of solar cells were studied but the resulting optical gains were compromised by the increased parasitic absorption in other non-active layers. *It was identified that placing the light-trapping structures closely touching the active CIGSe layer would be most favourable for light-trapping effects.*

Chapter 5, 6, 7 focused on the light-trapping structures: metallic nanoparticles underneath ITO back contact (chapter 5), 2-D $SiO_2$ nanosphere arrays on the surface (chapter 6) and $SiO_2$ dielectric nanostructures at the interface of CIGSe/Mo (chapter 7). In chapter 5, *it was firstly found that Ag nanoparticles at the interface of ITO/glass still failed to be thermally passivated by the ITO back contact even at a low substrate*

*temperature of 440 °C. The 50 nm thick $Al_2O_3$ film prepared by ALD was introduced to coat the Ag nanoparticles and was able to block the diffusion of Ag.* Unfortunately, the optical gain was not observed because the solar cells couldn't work electrically well. *Via the theoretical 3-D optical simulations, it was confirmed that the Ag nanoparticles underneath the ITO back contact can optically contribute to the effective $Abs_{CIGSe}$ of solar cells.* The further step for this light-trapping configuration is to identify the reasons of the electrically poor performance and solve it, transfer the optical gain to the electric benefit.

Considering the thermal instability and parasitic absorption being general problems for metallic materials, chapter 6 and 7 turned to the dielectric light-trapping structures. In chapter 6, the 2-D $SiO_2$ nanosphere arrays on the surface of solar cells were investigated. Larger spheres could support the whispering gallery modes (WGMs), which incoupled more light from air to the underlying solar cells in a narrow wavelength range. *Whereas the small sphere (around 110 nm) could form an optimum effective anti-reflection layer and offer a broadband $Abs_{CIGSe}$ enhancement.* Due to the broadband enhancement of anti-reflection effect, the 110-nm-diameter sphere array offers the maximum photocurrent density enhancement. Experiments and theoretical simulations show the agreeable results and a $J_{sc}$ enhancement of 2.17mA/cm$^2$ was experimentally achieved for the ultra-thin CIGSe solar cell with a 460-nm-thick absorber coating by the 120-nm-diameter sphere array.

*To reduce the parasitic $Abs_{Mo}$, $SiO_2$ nanostructures at the interface of CIGSe/Mo were investigated in chapter 7.* Due to the strong Mie scattering, $SiO_2$ nanostructures at the interface of CIGSe/Mo were able to scatter back the unabsorbed light into the CIGSe absorber and achieved the goal of increasing $Abs_{CIGSe}$ as well as reducing $Abs_{Mo}$. *With the presence of the $SiO_2$ nanostructures (pyramid shaped, 205 nm in radius, 210 nm in height and 513 nm in pitch), $J_{sc}$ was significantly enhanced from 28.6 to 30.6 mA/cm$^2$. From the simulation, it was found that $J_{sc}$ gain maily arose from the significant drop of $Abs_{Mo}$. This is the first time that $J_{sc}$ was reported to be above 30 mA/cm$^2$ for ultra-thin solar cells.* Further with the anti-reflection layer made of the 120-nm-diameter nanosphere array on the surface, $R$ was restraint and was further enhanced to 31.6 mA/cm$^2$. Since $SiO_2$ nanostructures can greatly reduce the parasitic $Abs_{Mo}$, which shows the most potential to achieve a $J_{sc}$ value comparable to that of the thick solar cells (around 35 mA/cm$^2$). The direction to narrow the $J_{sc}$ gap is to further reduce the

parasitic $Abs_{Mo}$. This can be possible realized by replacing Mo back contact by TCO or/and by adjusting the materials and geometries of nanostructures for better light-trapping effect.

# Appendix A: Optical simulation methods and tools

## A.1 Transfer-Matrix method - RefDex:

RefDex is a 1-D optical simulation tool, which is developed in house by Phillip Manley (phillip.manley@helmholtz-berlin.de). The calculation mechanism behind is the Transfer-Matrix method as described in Chapter 3. It is designed to calculate 1) optical constants of a single layer from R/T measurement and 2) inversely R/T/Abs from optical constants of each layer for the layer-stack structures with flat interfaces. It can deal with both coherent and incoherent propagation of light as well as oblique incidence. In my work, RefDex is used for the extraction of optical constants of layers in CIGSe layer in chapter 3 and the calculation of optical responses of ultra-thin CIGSe solar cells in chapter 4. The main features of RefDex are summarized as follows:

- The layer structure can reach as maximum layers as 9, which is generally enough for solar cell simulation. Each layer can be assigned a thickness and a set of optical constants.
- The definition of polarization and incidence of light is available. The incoherent propagation of light can be realized by the identification as substrates.
- Rough interfaces are taken into account with scalar scattering theory.
- Inhomogeneous layers are implemented through novel methods.
- Model-free method for the refractive index is assumed for the extraction of optical constants.

For more information about RefDex, please refer to Ref [55]

## A.2 Finite Element method - JCMwave:

JCMwave is a complete Finite Element software package for the computation of electromagnetic waves, elasticity and heat conduction. Since my work is related to the optical computations, I will explain the brief working principles from the aspect of electromagnetic waves in the following. The Finite Element (FE) method is a numerical calculation based on the Maxwell's equations. It is working by approximating the solutions to the exact solutions in the computational domain. For the solution computation, the computational domain is firstly sub-divided into small patches and defining a small polynomial space on each patch (finite elements). These locally defined polynomial spaces are then connected with the tangential continuity, allowing the electric and magnetic field across the boundaries of the patches. Finally, these conditions of tangential continuities can be introduced to the Maxwell's equations and approximate solutions can be obtained. This FE method has features:

- The complex geometry can be accurately represented without geometrical approximations.
- High order approximation can be obtained for fast convergence.
- The element meshes can be adjusted to suit the behavior of the solutions.
- The subdomain (small patches) can be very small, the local effects can be distinguished and captured (eg. near field of particles).

In this work, JCMwave is mainly used for the optical simulations on the CIGSe solar cells incorporating nanoparticles. As introduced above, RefDex is only applicable for the layer-stack structures with flat interfaces and cannot deal with the complete structures incorporating nanoparticles. Besides, the local effects of nanoparticles are needed to interpret the macroscopic optical phenomenon of the whole devices. The calculation process is operated by the command codes in the Matlab file.

For more information about the FE method and the program JCMwave, please refer to the references:

[87] http://www.jcmwave.com/

[102] http://en.wikipedia.org/wiki/Finite_element_method

# Appendix B: Optical constants of layers in the CIGSe solar cells

Table B.1: Optical constants of $CuIn_{1-x}Ga_xSe_2$ (x = 0, 0.19, 0.33, 0.48) shown in Fig.3.9.

| λ / nm | x = 0 | | x = 0.19 | | x = 0.33 | | x = 0.48 | |
|---|---|---|---|---|---|---|---|---|
| | *n* | *k* | *n* | *k* | *n* | *k* | *n* | *k* |
| 400 | 2.75 | 1.06 | 2.94 | 0.80 | 3.04 | 0.76 | 2.87 | 0.68 |
| 410 | 2.80 | 1.08 | 2.90 | 0.83 | 3.03 | 0.79 | 2.84 | 0.69 |
| 420 | 2.87 | 1.06 | 2.88 | 0.85 | 3.03 | 0.80 | 2.83 | 0.69 |
| 430 | 2.94 | 1.01 | 2.89 | 0.83 | 3.03 | 0.77 | 2.82 | 0.68 |
| 440 | 3.01 | 0.92 | 2.91 | 0.79 | 3.03 | 0.72 | 2.82 | 0.65 |
| 450 | 3.06 | 0.83 | 2.93 | 0.74 | 3.04 | 0.66 | 2.82 | 0.61 |
| 460 | 3.10 | 0.74 | 2.95 | 0.68 | 3.03 | 0.59 | 2.82 | 0.57 |
| 470 | 3.12 | 0.68 | 2.95 | 0.63 | 3.02 | 0.54 | 2.82 | 0.53 |
| 480 | 3.12 | 0.62 | 2.93 | 0.59 | 3.00 | 0.50 | 2.82 | 0.50 |
| 490 | 3.10 | 0.59 | 2.90 | 0.55 | 2.98 | 0.48 | 2.82 | 0.47 |
| 500 | 3.08 | 0.56 | 2.88 | 0.52 | 2.95 | 0.45 | 2.82 | 0.45 |
| 510 | 3.06 | 0.54 | 2.88 | 0.49 | 2.93 | 0.43 | 2.82 | 0.43 |
| 520 | 3.04 | 0.52 | 2.88 | 0.47 | 2.90 | 0.42 | 2.82 | 0.42 |
| 530 | 3.02 | 0.50 | 2.88 | 0.45 | 2.89 | 0.40 | 2.82 | 0.40 |
| 540 | 3.00 | 0.49 | 2.88 | 0.44 | 2.87 | 0.39 | 2.82 | 0.39 |
| 550 | 2.99 | 0.47 | 2.89 | 0.43 | 2.87 | 0.38 | 2.82 | 0.38 |
| 560 | 2.97 | 0.46 | 2.88 | 0.42 | 2.86 | 0.37 | 2.82 | 0.36 |
| 570 | 2.97 | 0.45 | 2.88 | 0.41 | 2.86 | 0.36 | 2.82 | 0.35 |
| 580 | 2.96 | 0.43 | 2.88 | 0.40 | 2.86 | 0.35 | 2.82 | 0.34 |
| 590 | 2.95 | 0.42 | 2.88 | 0.39 | 2.86 | 0.34 | 2.83 | 0.34 |
| 600 | 2.94 | 0.41 | 2.88 | 0.38 | 2.85 | 0.33 | 2.83 | 0.33 |
| 610 | 2.94 | 0.40 | 2.89 | 0.38 | 2.85 | 0.32 | 2.84 | 0.33 |
| 620 | 2.93 | 0.40 | 2.89 | 0.37 | 2.84 | 0.32 | 2.84 | 0.32 |
| 630 | 2.93 | 0.39 | 2.89 | 0.36 | 2.84 | 0.31 | 2.85 | 0.31 |
| 640 | 2.93 | 0.38 | 2.89 | 0.36 | 2.84 | 0.31 | 2.85 | 0.31 |
| 650 | 2.93 | 0.38 | 2.89 | 0.35 | 2.84 | 0.30 | 2.85 | 0.30 |
| 660 | 2.93 | 0.37 | 2.89 | 0.34 | 2.85 | 0.30 | 2.85 | 0.29 |
| 670 | 2.92 | 0.37 | 2.89 | 0.33 | 2.85 | 0.30 | 2.86 | 0.28 |
| 680 | 2.92 | 0.36 | 2.89 | 0.33 | 2.85 | 0.29 | 2.86 | 0.28 |
| 690 | 2.92 | 0.36 | 2.90 | 0.32 | 2.85 | 0.28 | 2.87 | 0.27 |
| 700 | 2.92 | 0.35 | 2.90 | 0.32 | 2.85 | 0.28 | 2.87 | 0.26 |
| 710 | 2.92 | 0.35 | 2.91 | 0.31 | 2.85 | 0.27 | 2.88 | 0.26 |
| 720 | 2.92 | 0.34 | 2.91 | 0.31 | 2.85 | 0.26 | 2.88 | 0.25 |
| 730 | 2.92 | 0.34 | 2.92 | 0.30 | 2.85 | 0.26 | 2.88 | 0.24 |
| 740 | 2.93 | 0.34 | 2.92 | 0.30 | 2.85 | 0.25 | 2.89 | 0.24 |
| 750 | 2.93 | 0.33 | 2.91 | 0.30 | 2.85 | 0.24 | 2.89 | 0.23 |
| 760 | 2.93 | 0.33 | 2.90 | 0.29 | 2.85 | 0.24 | 2.90 | 0.22 |
| 770 | 2.93 | 0.33 | 2.89 | 0.29 | 2.86 | 0.23 | 2.90 | 0.21 |
| 780 | 2.93 | 0.32 | 2.88 | 0.29 | 2.86 | 0.22 | 2.90 | 0.21 |
| 790 | 2.93 | 0.32 | 2.88 | 0.29 | 2.86 | 0.22 | 2.90 | 0.20 |
| 800 | 2.94 | 0.32 | 2.88 | 0.28 | 2.86 | 0.21 | 2.90 | 0.19 |
| 810 | 2.94 | 0.31 | 2.88 | 0.28 | 2.86 | 0.20 | 2.90 | 0.18 |
| 820 | 2.94 | 0.31 | 2.88 | 0.28 | 2.87 | 0.19 | 2.89 | 0.17 |
| 830 | 2.94 | 0.31 | 2.88 | 0.27 | 2.86 | 0.19 | 2.89 | 0.16 |
| 840 | 2.95 | 0.30 | 2.88 | 0.26 | 2.86 | 0.18 | 2.89 | 0.15 |
| 850 | 2.95 | 0.30 | 2.88 | 0.26 | 2.86 | 0.17 | 2.89 | 0.14 |
| 860 | 2.95 | 0.29 | 2.88 | 0.25 | 2.86 | 0.17 | 2.89 | 0.13 |
| 870 | 2.96 | 0.29 | 2.89 | 0.24 | 2.86 | 0.16 | 2.89 | 0.12 |
| 880 | 2.96 | 0.28 | 2.89 | 0.24 | 2.85 | 0.15 | 2.88 | 0.11 |
| 890 | 2.97 | 0.28 | 2.89 | 0.23 | 2.85 | 0.14 | 2.88 | 0.10 |
| 900 | 2.97 | 0.28 | 2.90 | 0.22 | 2.85 | 0.14 | 2.88 | 0.09 |
| 910 | 2.97 | 0.28 | 2.90 | 0.21 | 2.85 | 0.13 | 2.87 | 0.08 |
| 920 | 2.97 | 0.27 | 2.90 | 0.20 | 2.85 | 0.12 | 2.87 | 0.08 |
| 930 | 2.97 | 0.27 | 2.91 | 0.19 | 2.84 | 0.12 | 2.87 | 0.07 |
| 940 | 2.96 | 0.27 | 2.91 | 0.19 | 2.84 | 0.11 | 2.87 | 0.06 |
| 950 | 2.96 | 0.26 | 2.91 | 0.18 | 2.84 | 0.10 | 2.87 | 0.06 |
| 960 | 2.95 | 0.25 | 2.92 | 0.17 | 2.83 | 0.09 | 2.87 | 0.06 |

| $\lambda$ / nm | $x$ = 0 | | $x$ = 0.17 | | $x$ = 0.33 | | $x$ = 0.48 | |
|---|---|---|---|---|---|---|---|---|
| | $n$ | $k$ | $n$ | $k$ | $n$ | $k$ | $n$ | $k$ |
| 970 | 2.95 | 0.24 | 2.92 | 0.17 | 2.83 | 0.08 | 2.87 | 0.05 |
| 980 | 2.95 | 0.23 | 2.93 | 0.16 | 2.83 | 0.07 | 2.87 | 0.04 |
| 990 | 2.95 | 0.22 | 2.93 | 0.16 | 2.83 | 0.07 | 2.87 | 0.04 |
| 1000 | 2.95 | 0.21 | 2.93 | 0.15 | 2.83 | 0.06 | 2.87 | 0.03 |
| 1010 | 2.96 | 0.21 | 2.94 | 0.15 | 2.82 | 0.06 | 2.87 | 0.02 |
| 1020 | 2.96 | 0.20 | 2.94 | 0.14 | 2.82 | 0.05 | 2.87 | 0.01 |
| 1030 | 2.96 | 0.19 | 2.95 | 0.14 | 2.82 | 0.04 | 2.86 | 0.01 |
| 1040 | 2.97 | 0.19 | 2.95 | 0.13 | 2.81 | 0.04 | 2.86 | 0.01 |
| 1050 | 2.97 | 0.18 | 2.95 | 0.12 | 2.81 | 0.03 | 2.85 | 0.00 |
| 1060 | 2.97 | 0.18 | 2.95 | 0.11 | 2.81 | 0.02 | 2.85 | 0.00 |
| 1070 | 2.97 | 0.17 | 2.95 | 0.11 | 2.81 | 0.02 | 2.84 | 0.00 |
| 1080 | 2.97 | 0.17 | 2.94 | 0.10 | 2.81 | 0.01 | 2.84 | 0.00 |
| 1090 | 2.97 | 0.16 | 2.93 | 0.09 | 2.80 | 0.00 | 2.84 | 0.00 |
| 1100 | 2.97 | 0.16 | 2.92 | 0.08 | 2.80 | 0.00 | 2.83 | 0.00 |
| 1110 | 2.97 | 0.15 | 2.92 | 0.06 | 2.80 | 0.00 | 2.83 | 0.00 |
| 1120 | 2.98 | 0.15 | 2.92 | 0.05 | 2.80 | 0.00 | 2.83 | 0.00 |
| 1130 | 2.98 | 0.14 | 2.92 | 0.04 | 2.79 | 0.00 | 2.82 | 0.00 |
| 1140 | 2.98 | 0.14 | 2.92 | 0.03 | 2.79 | 0.00 | 2.82 | 0.00 |
| 1150 | 2.99 | 0.13 | 2.92 | 0.02 | 2.78 | 0.00 | 2.82 | 0.00 |
| 1160 | 2.99 | 0.12 | 2.92 | 0.02 | 2.78 | 0.00 | 2.81 | 0.00 |
| 1170 | 3.00 | 0.11 | 2.91 | 0.01 | 2.78 | 0.00 | 2.81 | 0.00 |
| 1180 | 3.00 | 0.10 | 2.91 | 0.01 | 2.77 | 0.00 | 2.80 | 0.00 |
| 1190 | 3.00 | 0.09 | 2.90 | 0.00 | 2.77 | 0.00 | 2.80 | 0.00 |
| 1200 | 3.00 | 0.08 | 2.90 | 0.00 | 2.77 | 0.00 | 2.79 | 0.00 |
| 1210 | 3.00 | 0.07 | 2.89 | 0.00 | 2.77 | 0.00 | 2.79 | 0.00 |
| 1220 | 3.00 | 0.06 | 2.89 | 0.00 | 2.77 | 0.00 | 2.79 | 0.00 |
| 1230 | 2.99 | 0.05 | 2.89 | 0.00 | 2.77 | 0.00 | 2.79 | 0.00 |
| 1240 | 2.99 | 0.03 | 2.89 | 0.00 | 2.77 | 0.00 | 2.79 | 0.00 |
| 1250 | 2.98 | 0.02 | 2.89 | 0.00 | 2.77 | 0.00 | 2.80 | 0.00 |
| 1260 | 2.97 | 0.01 | 2.88 | 0.00 | 2.77 | 0.00 | 2.80 | 0.00 |
| 1270 | 2.96 | 0.01 | 2.88 | 0.00 | 2.77 | 0.00 | 2.80 | 0.00 |
| 1280 | 2.95 | 0.00 | 2.87 | 0.00 | 2.76 | 0.00 | 2.79 | 0.00 |
| 1290 | 2.94 | 0.00 | 2.87 | 0.00 | 2.76 | 0.00 | 2.79 | 0.00 |
| 1300 | 2.93 | 0.00 | 2.86 | 0.00 | 2.76 | 0.00 | 2.79 | 0.00 |
| 1310 | 2.93 | 0.00 | 2.85 | 0.00 | 2.75 | 0.00 | 2.79 | 0.00 |
| 1320 | 2.92 | 0.00 | 2.84 | 0.00 | 2.75 | 0.00 | 2.79 | 0.00 |
| 1330 | 2.91 | 0.00 | 2.84 | 0.00 | 2.75 | 0.00 | 2.79 | 0.00 |
| 1340 | 2.91 | 0.00 | 2.83 | 0.00 | 2.75 | 0.00 | 2.79 | 0.00 |
| 1350 | 2.90 | 0.00 | 2.83 | 0.00 | 2.75 | 0.00 | 2.78 | 0.00 |
| 1360 | 2.89 | 0.00 | 2.82 | 0.00 | 2.75 | 0.00 | 2.78 | 0.00 |
| 1370 | 2.88 | 0.00 | 2.82 | 0.00 | 2.75 | 0.00 | 2.78 | 0.00 |
| 1380 | 2.87 | 0.00 | 2.82 | 0.00 | 2.75 | 0.00 | 2.78 | 0.00 |
| 1390 | 2.87 | 0.00 | 2.81 | 0.00 | 2.75 | 0.00 | 2.78 | 0.00 |
| 1400 | 2.88 | 0.00 | 2.81 | 0.00 | 2.74 | 0.00 | 2.78 | 0.00 |
| 1410 | 2.88 | 0.00 | 2.81 | 0.00 | 2.74 | 0.00 | 2.77 | 0.00 |
| 1420 | 2.88 | 0.00 | 2.81 | 0.00 | 2.74 | 0.00 | 2.77 | 0.00 |
| 1430 | 2.88 | 0.00 | 2.80 | 0.00 | 2.74 | 0.00 | 2.77 | 0.00 |
| 1440 | 2.87 | 0.00 | 2.80 | 0.00 | 2.74 | 0.00 | 2.77 | 0.00 |
| 1450 | 2.87 | 0.00 | 2.80 | 0.00 | 2.74 | 0.00 | 2.76 | 0.00 |
| 1460 | 2.87 | 0.00 | 2.79 | 0.01 | 2.73 | 0.00 | 2.76 | 0.00 |
| 1470 | 2.87 | 0.00 | 2.79 | 0.01 | 2.73 | 0.00 | 2.76 | 0.00 |
| 1480 | 2.87 | 0.00 | 2.80 | 0.01 | 2.73 | 0.00 | 2.76 | 0.00 |
| 1490 | 2.87 | 0.00 | 2.80 | 0.01 | 2.73 | 0.00 | 2.75 | 0.00 |
| 1500 | 2.87 | 0.00 | 2.80 | 0.01 | 2.73 | 0.00 | 2.75 | 0.00 |
| 1510 | 2.86 | 0.00 | 2.80 | 0.01 | 2.73 | 0.00 | 2.75 | 0.00 |
| 1520 | 2.86 | 0.00 | 2.79 | 0.01 | 2.73 | 0.00 | 2.75 | 0.00 |
| 1530 | 2.86 | 0.00 | 2.79 | 0.01 | 2.73 | 0.00 | 2.75 | 0.00 |
| 1540 | 2.85 | 0.00 | 2.79 | 0.01 | 2.73 | 0.00 | 2.74 | 0.00 |
| 1550 | 2.85 | 0.00 | 2.79 | 0.00 | 2.73 | 0.00 | 2.74 | 0.00 |
| 1560 | 2.85 | 0.00 | 2.79 | 0.00 | 2.73 | 0.00 | 2.74 | 0.00 |
| 1570 | 2.85 | 0.00 | 2.79 | 0.00 | 2.72 | 0.00 | 2.74 | 0.00 |
| 1580 | 2.85 | 0.00 | 2.79 | 0.00 | 2.72 | 0.00 | 2.74 | 0.00 |
| 1590 | 2.85 | 0.00 | 2.79 | 0.00 | 2.71 | 0.00 | 2.74 | 0.00 |
| 1600 | 2.85 | 0.00 | 2.79 | 0.00 | 2.71 | 0.00 | 2.74 | 0.00 |
| 1610 | 2.85 | 0.00 | 2.79 | 0.01 | 2.70 | 0.00 | 2.74 | 0.00 |
| 1620 | 2.85 | 0.00 | 2.78 | 0.01 | 2.70 | 0.00 | 2.74 | 0.00 |
| 1630 | 2.85 | 0.00 | 2.78 | 0.00 | 2.70 | 0.00 | 2.74 | 0.00 |
| 1640 | 2.84 | 0.00 | 2.78 | 0.00 | 2.70 | 0.00 | 2.74 | 0.00 |
| 1650 | 2.84 | 0.00 | 2.78 | 0.00 | 2.70 | 0.00 | 2.74 | 0.00 |

| λ / nm | *x* = 0 | | *x* = 0.17 | | *x* = 0.33 | | *x* = 0.48 | |
|---|---|---|---|---|---|---|---|---|
| | *n* | *k* | *n* | *k* | *n* | *k* | *n* | *k* |
| 1660 | 2.84 | 0.00 | 2.78 | 0.00 | 2.70 | 0.00 | 2.73 | 0.00 |
| 1670 | 2.83 | 0.00 | 2.78 | 0.00 | 2.70 | 0.00 | 2.73 | 0.00 |
| 1680 | 2.83 | 0.00 | 2.78 | 0.00 | 2.70 | 0.00 | 2.73 | 0.00 |
| 1690 | 2.83 | 0.00 | 2.77 | 0.00 | 2.70 | 0.00 | 2.73 | 0.00 |
| 1700 | 2.83 | 0.00 | 2.77 | 0.00 | 2.70 | 0.00 | 2.73 | 0.00 |
| 1710 | 2.83 | 0.00 | 2.77 | 0.00 | 2.70 | 0.00 | 2.73 | 0.00 |
| 1720 | 2.83 | 0.00 | 2.77 | 0.00 | 2.70 | 0.00 | 2.73 | 0.00 |
| 1730 | 2.83 | 0.01 | 2.77 | 0.00 | 2.69 | 0.00 | 2.73 | 0.00 |
| 1740 | 2.83 | 0.01 | 2.77 | 0.00 | 2.69 | 0.00 | 2.73 | 0.00 |
| 1750 | 2.83 | 0.01 | 2.77 | 0.00 | 2.69 | 0.00 | 2.73 | 0.00 |
| 1760 | 2.83 | 0.01 | 2.77 | 0.00 | 2.69 | 0.00 | 2.73 | 0.00 |
| 1770 | 2.82 | 0.01 | 2.77 | 0.00 | 2.69 | 0.00 | 2.73 | 0.00 |
| 1780 | 2.82 | 0.01 | 2.77 | 0.00 | 2.69 | 0.00 | 2.73 | 0.00 |
| 1790 | 2.82 | 0.01 | 2.77 | 0.00 | 2.69 | 0.00 | 2.73 | 0.00 |
| 1800 | 2.82 | 0.01 | 2.76 | 0.00 | 2.69 | 0.00 | 2.72 | 0.00 |
| 1810 | 2.82 | 0.01 | 2.76 | 0.00 | 2.69 | 0.00 | 2.72 | 0.00 |
| 1820 | 2.81 | 0.01 | 2.76 | 0.00 | 2.68 | 0.00 | 2.72 | 0.00 |
| 1830 | 2.81 | 0.01 | 2.76 | 0.00 | 2.68 | 0.01 | 2.72 | 0.00 |
| 1840 | 2.81 | 0.01 | 2.76 | 0.00 | 2.68 | 0.01 | 2.72 | 0.00 |
| 1850 | 2.81 | 0.01 | 2.76 | 0.00 | 2.68 | 0.01 | 2.72 | 0.00 |
| 1860 | 2.81 | 0.01 | 2.76 | 0.00 | 2.68 | 0.01 | 2.72 | 0.00 |
| 1870 | 2.80 | 0.01 | 2.75 | 0.00 | 2.68 | 0.01 | 2.72 | 0.00 |
| 1880 | 2.80 | 0.01 | 2.75 | 0.00 | 2.68 | 0.00 | 2.72 | 0.00 |
| 1890 | 2.80 | 0.01 | 2.75 | 0.00 | 2.68 | 0.00 | 2.72 | 0.00 |
| 1900 | 2.80 | 0.01 | 2.75 | 0.00 | 2.68 | 0.00 | 2.71 | 0.00 |
| 1910 | 2.80 | 0.01 | 2.75 | 0.00 | 2.68 | 0.00 | 2.71 | 0.00 |
| 1920 | 2.80 | 0.01 | 2.75 | 0.00 | 2.67 | 0.00 | 2.71 | 0.00 |
| 1930 | 2.80 | 0.02 | 2.75 | 0.00 | 2.67 | 0.00 | 2.71 | 0.00 |
| 1940 | 2.79 | 0.02 | 2.75 | 0.00 | 2.67 | 0.00 | 2.71 | 0.00 |
| 1950 | 2.79 | 0.02 | 2.74 | 0.00 | 2.67 | 0.00 | 2.71 | 0.00 |
| 1960 | 2.79 | 0.02 | 2.74 | 0.00 | 2.67 | 0.00 | 2.71 | 0.00 |
| 1970 | 2.79 | 0.02 | 2.74 | 0.00 | 2.67 | 0.00 | 2.71 | 0.00 |
| 1980 | 2.79 | 0.02 | 2.74 | 0.00 | 2.67 | 0.00 | 2.71 | 0.00 |

Table B.2: Optical constants of $CuIn_{1-x}Ga_xSe_2$ (x = 0.53, 0.77, 0.92, 1.00) shown in Fig.3.9.

| λ / nm | *x* = 0.53 | | *x* = 0.77 | | *x* = 0.92 | | *x* = 1.0 | |
|---|---|---|---|---|---|---|---|---|
| | *n* | *k* | *n* | *k* | *n* | *k* | *n* | *k* |
| 400 | 2.83 | 0.77 | 2.75 | 0.81 | 2.97 | 0.60 | 3.19 | 0.76 |
| 410 | 2.80 | 0.75 | 2.77 | 0.81 | 2.97 | 0.63 | 3.16 | 0.67 |
| 420 | 2.78 | 0.73 | 2.80 | 0.79 | 2.97 | 0.63 | 3.13 | 0.58 |
| 430 | 2.78 | 0.69 | 2.83 | 0.73 | 2.97 | 0.60 | 3.12 | 0.50 |
| 440 | 2.79 | 0.65 | 2.84 | 0.65 | 2.97 | 0.55 | 3.11 | 0.45 |
| 450 | 2.80 | 0.61 | 2.86 | 0.57 | 2.97 | 0.49 | 3.11 | 0.41 |
| 460 | 2.81 | 0.56 | 2.86 | 0.51 | 2.97 | 0.43 | 3.11 | 0.38 |
| 470 | 2.82 | 0.52 | 2.86 | 0.46 | 2.97 | 0.39 | 3.10 | 0.35 |
| 480 | 2.81 | 0.49 | 2.86 | 0.43 | 2.97 | 0.36 | 3.09 | 0.33 |
| 490 | 2.80 | 0.46 | 2.85 | 0.41 | 2.96 | 0.35 | 3.08 | 0.31 |
| 500 | 2.80 | 0.44 | 2.85 | 0.40 | 2.96 | 0.34 | 3.07 | 0.30 |
| 510 | 2.79 | 0.42 | 2.85 | 0.38 | 2.96 | 0.33 | 3.06 | 0.28 |
| 520 | 2.79 | 0.41 | 2.85 | 0.37 | 2.96 | 0.31 | 3.04 | 0.27 |
| 530 | 2.80 | 0.39 | 2.86 | 0.35 | 2.96 | 0.30 | 3.03 | 0.26 |
| 540 | 2.80 | 0.38 | 2.87 | 0.34 | 2.96 | 0.29 | 3.02 | 0.24 |
| 550 | 2.80 | 0.37 | 2.87 | 0.33 | 2.96 | 0.28 | 3.01 | 0.23 |
| 560 | 2.81 | 0.36 | 2.88 | 0.32 | 2.95 | 0.27 | 3.00 | 0.22 |
| 570 | 2.81 | 0.35 | 2.88 | 0.31 | 2.95 | 0.26 | 2.99 | 0.21 |
| 580 | 2.81 | 0.34 | 2.88 | 0.30 | 2.95 | 0.25 | 2.99 | 0.20 |
| 590 | 2.82 | 0.33 | 2.89 | 0.29 | 2.95 | 0.24 | 2.98 | 0.20 |
| 600 | 2.82 | 0.32 | 2.89 | 0.28 | 2.95 | 0.23 | 2.97 | 0.19 |
| 610 | 2.82 | 0.31 | 2.90 | 0.27 | 2.95 | 0.22 | 2.97 | 0.19 |
| 620 | 2.83 | 0.31 | 2.90 | 0.26 | 2.96 | 0.22 | 2.96 | 0.18 |
| 630 | 2.83 | 0.30 | 2.90 | 0.26 | 2.96 | 0.21 | 2.96 | 0.17 |
| 640 | 2.83 | 0.30 | 2.91 | 0.25 | 2.95 | 0.20 | 2.95 | 0.15 |
| 650 | 2.83 | 0.29 | 2.91 | 0.25 | 2.95 | 0.19 | 2.95 | 0.14 |
| 660 | 2.84 | 0.29 | 2.91 | 0.24 | 2.95 | 0.18 | 2.94 | 0.12 |
| 670 | 2.84 | 0.28 | 2.91 | 0.23 | 2.94 | 0.17 | 2.94 | 0.11 |
| 680 | 2.84 | 0.27 | 2.91 | 0.22 | 2.94 | 0.16 | 2.93 | 0.11 |
| 690 | 2.84 | 0.26 | 2.91 | 0.21 | 2.93 | 0.14 | 2.93 | 0.10 |
| 700 | 2.84 | 0.26 | 2.91 | 0.20 | 2.93 | 0.13 | 2.92 | 0.09 |
| 710 | 2.85 | 0.25 | 2.91 | 0.19 | 2.93 | 0.12 | 2.92 | 0.07 |
| 720 | 2.86 | 0.24 | 2.91 | 0.18 | 2.92 | 0.11 | 2.92 | 0.05 |
| 730 | 2.86 | 0.23 | 2.92 | 0.17 | 2.92 | 0.10 | 2.91 | 0.04 |
| 740 | 2.87 | 0.22 | 2.92 | 0.16 | 2.92 | 0.09 | 2.91 | 0.02 |
| 750 | 2.87 | 0.21 | 2.92 | 0.15 | 2.92 | 0.08 | 2.90 | 0.01 |
| 760 | 2.88 | 0.21 | 2.92 | 0.14 | 2.92 | 0.06 | 2.89 | 0.00 |
| 770 | 2.88 | 0.20 | 2.93 | 0.13 | 2.92 | 0.05 | 2.88 | 0.00 |
| 780 | 2.88 | 0.19 | 2.93 | 0.12 | 2.92 | 0.04 | 2.88 | 0.00 |
| 790 | 2.88 | 0.18 | 2.93 | 0.10 | 2.91 | 0.03 | 2.87 | 0.00 |
| 800 | 2.88 | 0.17 | 2.94 | 0.09 | 2.91 | 0.02 | 2.86 | 0.00 |
| 810 | 2.88 | 0.16 | 2.94 | 0.08 | 2.90 | 0.02 | 2.86 | 0.00 |
| 820 | 2.89 | 0.15 | 2.94 | 0.07 | 2.90 | 0.01 | 2.85 | 0.00 |
| 830 | 2.88 | 0.14 | 2.94 | 0.06 | 2.90 | 0.01 | 2.85 | 0.00 |
| 840 | 2.88 | 0.13 | 2.93 | 0.05 | 2.89 | 0.01 | 2.85 | 0.00 |
| 850 | 2.88 | 0.12 | 2.93 | 0.05 | 2.89 | 0.00 | 2.84 | 0.00 |
| 860 | 2.87 | 0.11 | 2.92 | 0.05 | 2.88 | 0.00 | 2.84 | 0.00 |
| 870 | 2.87 | 0.10 | 2.92 | 0.04 | 2.87 | 0.00 | 2.84 | 0.00 |
| 880 | 2.86 | 0.09 | 2.92 | 0.03 | 2.86 | 0.00 | 2.83 | 0.00 |
| 890 | 2.86 | 0.08 | 2.91 | 0.03 | 2.85 | 0.00 | 2.83 | 0.00 |
| 900 | 2.85 | 0.07 | 2.91 | 0.02 | 2.84 | 0.00 | 2.83 | 0.00 |
| 910 | 2.85 | 0.07 | 2.90 | 0.02 | 2.83 | 0.00 | 2.82 | 0.00 |
| 920 | 2.85 | 0.06 | 2.89 | 0.01 | 2.82 | 0.00 | 2.82 | 0.00 |
| 930 | 2.84 | 0.05 | 2.88 | 0.01 | 2.82 | 0.00 | 2.81 | 0.00 |
| 940 | 2.84 | 0.05 | 2.87 | 0.01 | 2.82 | 0.00 | 2.81 | 0.00 |
| 950 | 2.84 | 0.04 | 2.87 | 0.00 | 2.81 | 0.00 | 2.81 | 0.00 |
| 960 | 2.83 | 0.03 | 2.86 | 0.00 | 2.80 | 0.00 | 2.80 | 0.00 |
| 970 | 2.83 | 0.03 | 2.86 | 0.00 | 2.80 | 0.00 | 2.80 | 0.00 |
| 980 | 2.83 | 0.02 | 2.85 | 0.00 | 2.79 | 0.00 | 2.80 | 0.00 |
| 990 | 2.82 | 0.02 | 2.84 | 0.00 | 2.79 | 0.00 | 2.79 | 0.00 |
| 1000 | 2.82 | 0.01 | 2.84 | 0.00 | 2.79 | 0.00 | 2.78 | 0.00 |
| 1010 | 2.82 | 0.01 | 2.83 | 0.00 | 2.80 | 0.00 | 2.78 | 0.00 |
| 1020 | 2.81 | 0.00 | 2.82 | 0.00 | 2.80 | 0.00 | 2.77 | 0.00 |
| 1030 | 2.81 | 0.00 | 2.82 | 0.00 | 2.80 | 0.00 | 2.77 | 0.00 |

| λ / nm | *x* = 0.53 | | *x* = 0.77 | | *x* = 0.92 | | *x* = 1.0 | |
|---|---|---|---|---|---|---|---|---|
| | *n* | *k* | *n* | *k* | *n* | *k* | *n* | *k* |
| 1040 | 2.81 | 0.00 | 2.82 | 0.00 | 2.79 | 0.00 | 2.76 | 0.00 |
| 1050 | 2.81 | 0.01 | 2.81 | 0.00 | 2.78 | 0.00 | 2.76 | 0.00 |
| 1060 | 2.81 | 0.01 | 2.81 | 0.00 | 2.78 | 0.00 | 2.76 | 0.00 |
| 1070 | 2.81 | 0.01 | 2.81 | 0.00 | 2.77 | 0.00 | 2.75 | 0.01 |
| 1080 | 2.81 | 0.01 | 2.81 | 0.00 | 2.77 | 0.00 | 2.75 | 0.01 |
| 1090 | 2.81 | 0.01 | 2.81 | 0.00 | 2.77 | 0.00 | 2.75 | 0.01 |
| 1100 | 2.80 | 0.00 | 2.80 | 0.00 | 2.76 | 0.00 | 2.74 | 0.01 |
| 1110 | 2.80 | 0.00 | 2.80 | 0.00 | 2.76 | 0.00 | 2.74 | 0.01 |
| 1120 | 2.80 | 0.00 | 2.80 | 0.00 | 2.76 | 0.00 | 2.74 | 0.01 |
| 1130 | 2.79 | 0.00 | 2.80 | 0.00 | 2.76 | 0.00 | 2.74 | 0.01 |
| 1140 | 2.79 | 0.00 | 2.80 | 0.00 | 2.75 | 0.00 | 2.74 | 0.01 |
| 1150 | 2.79 | 0.00 | 2.79 | 0.00 | 2.75 | 0.00 | 2.74 | 0.01 |
| 1160 | 2.79 | 0.00 | 2.79 | 0.00 | 2.75 | 0.00 | 2.74 | 0.01 |
| 1170 | 2.78 | 0.00 | 2.79 | 0.00 | 2.75 | 0.00 | 2.74 | 0.01 |
| 1180 | 2.78 | 0.00 | 2.78 | 0.00 | 2.75 | 0.00 | 2.74 | 0.01 |
| 1190 | 2.77 | 0.00 | 2.78 | 0.00 | 2.74 | 0.00 | 2.73 | 0.01 |
| 1200 | 2.77 | 0.00 | 2.78 | 0.00 | 2.74 | 0.00 | 2.73 | 0.01 |
| 1210 | 2.76 | 0.00 | 2.78 | 0.00 | 2.74 | 0.00 | 2.73 | 0.01 |
| 1220 | 2.76 | 0.00 | 2.78 | 0.00 | 2.74 | 0.00 | 2.73 | 0.01 |
| 1230 | 2.76 | 0.00 | 2.78 | 0.00 | 2.74 | 0.00 | 2.73 | 0.01 |
| 1240 | 2.76 | 0.00 | 2.78 | 0.00 | 2.74 | 0.00 | 2.73 | 0.01 |
| 1250 | 2.76 | 0.00 | 2.78 | 0.00 | 2.74 | 0.00 | 2.73 | 0.01 |
| 1260 | 2.76 | 0.00 | 2.78 | 0.00 | 2.74 | 0.00 | 2.72 | 0.01 |
| 1270 | 2.76 | 0.00 | 2.77 | 0.00 | 2.74 | 0.00 | 2.72 | 0.01 |
| 1280 | 2.76 | 0.00 | 2.77 | 0.00 | 2.74 | 0.00 | 2.72 | 0.01 |
| 1290 | 2.76 | 0.00 | 2.77 | 0.00 | 2.74 | 0.00 | 2.72 | 0.01 |
| 1300 | 2.76 | 0.00 | 2.77 | 0.00 | 2.74 | 0.00 | 2.72 | 0.01 |
| 1310 | 2.75 | 0.00 | 2.77 | 0.00 | 2.74 | 0.00 | 2.72 | 0.01 |
| 1320 | 2.75 | 0.00 | 2.77 | 0.00 | 2.74 | 0.00 | 2.72 | 0.01 |
| 1330 | 2.75 | 0.00 | 2.77 | 0.00 | 2.73 | 0.00 | 2.72 | 0.01 |
| 1340 | 2.75 | 0.00 | 2.77 | 0.00 | 2.73 | 0.00 | 2.72 | 0.01 |
| 1350 | 2.75 | 0.00 | 2.76 | 0.00 | 2.73 | 0.00 | 2.71 | 0.01 |
| 1360 | 2.75 | 0.00 | 2.76 | 0.00 | 2.73 | 0.00 | 2.71 | 0.01 |
| 1370 | 2.75 | 0.00 | 2.76 | 0.00 | 2.73 | 0.00 | 2.71 | 0.01 |
| 1380 | 2.75 | 0.00 | 2.76 | 0.00 | 2.73 | 0.00 | 2.71 | 0.01 |
| 1390 | 2.75 | 0.00 | 2.76 | 0.00 | 2.73 | 0.00 | 2.71 | 0.01 |
| 1400 | 2.75 | 0.00 | 2.76 | 0.00 | 2.73 | 0.00 | 2.71 | 0.01 |
| 1410 | 2.75 | 0.00 | 2.76 | 0.00 | 2.73 | 0.00 | 2.71 | 0.01 |
| 1420 | 2.75 | 0.00 | 2.76 | 0.00 | 2.73 | 0.00 | 2.71 | 0.01 |
| 1430 | 2.75 | 0.00 | 2.76 | 0.00 | 2.72 | 0.00 | 2.70 | 0.01 |
| 1440 | 2.75 | 0.00 | 2.76 | 0.00 | 2.72 | 0.00 | 2.70 | 0.01 |
| 1450 | 2.75 | 0.00 | 2.76 | 0.00 | 2.71 | 0.00 | 2.70 | 0.01 |
| 1460 | 2.75 | 0.00 | 2.76 | 0.00 | 2.71 | 0.00 | 2.70 | 0.01 |
| 1470 | 2.74 | 0.00 | 2.76 | 0.00 | 2.71 | 0.00 | 2.70 | 0.01 |
| 1480 | 2.74 | 0.00 | 2.75 | 0.00 | 2.71 | 0.00 | 2.70 | 0.01 |
| 1490 | 2.74 | 0.00 | 2.75 | 0.00 | 2.71 | 0.00 | 2.70 | 0.01 |
| 1500 | 2.74 | 0.00 | 2.75 | 0.00 | 2.71 | 0.00 | 2.70 | 0.01 |
| 1510 | 2.73 | 0.00 | 2.74 | 0.00 | 2.71 | 0.00 | 2.70 | 0.01 |
| 1520 | 2.73 | 0.00 | 2.74 | 0.00 | 2.71 | 0.00 | 2.70 | 0.01 |
| 1530 | 2.73 | 0.00 | 2.74 | 0.00 | 2.70 | 0.00 | 2.70 | 0.01 |
| 1540 | 2.73 | 0.00 | 2.74 | 0.00 | 2.70 | 0.00 | 2.70 | 0.01 |
| 1550 | 2.73 | 0.00 | 2.73 | 0.00 | 2.70 | 0.00 | 2.70 | 0.01 |
| 1560 | 2.73 | 0.00 | 2.73 | 0.00 | 2.70 | 0.00 | 2.69 | 0.01 |
| 1570 | 2.73 | 0.00 | 2.73 | 0.00 | 2.70 | 0.00 | 2.69 | 0.01 |
| 1580 | 2.73 | 0.00 | 2.73 | 0.00 | 2.70 | 0.00 | 2.69 | 0.01 |
| 1590 | 2.73 | 0.00 | 2.73 | 0.00 | 2.70 | 0.00 | 2.69 | 0.01 |
| 1600 | 2.73 | 0.00 | 2.73 | 0.00 | 2.70 | 0.00 | 2.69 | 0.01 |
| 1610 | 2.72 | 0.00 | 2.73 | 0.00 | 2.70 | 0.00 | 2.69 | 0.01 |
| 1620 | 2.72 | 0.00 | 2.73 | 0.00 | 2.70 | 0.00 | 2.69 | 0.01 |
| 1630 | 2.72 | 0.00 | 2.73 | 0.00 | 2.70 | 0.00 | 2.69 | 0.01 |
| 1640 | 2.72 | 0.00 | 2.73 | 0.00 | 2.70 | 0.00 | 2.69 | 0.01 |
| 1650 | 2.72 | 0.00 | 2.73 | 0.00 | 2.70 | 0.00 | 2.69 | 0.01 |
| 1660 | 2.71 | 0.00 | 2.73 | 0.00 | 2.69 | 0.00 | 2.69 | 0.01 |
| 1670 | 2.71 | 0.00 | 2.73 | 0.00 | 2.69 | 0.00 | 2.69 | 0.01 |
| 1680 | 2.71 | 0.00 | 2.73 | 0.00 | 2.69 | 0.00 | 2.70 | 0.01 |
| 1690 | 2.71 | 0.00 | 2.73 | 0.00 | 2.69 | 0.01 | 2.70 | 0.01 |
| 1700 | 2.71 | 0.00 | 2.73 | 0.00 | 2.69 | 0.01 | 2.70 | 0.01 |
| 1710 | 2.71 | 0.00 | 2.72 | 0.00 | 2.69 | 0.01 | 2.71 | 0.01 |

| λ / nm | *x* = 0.53 | | *x* = 0.77 | | *x* = 0.92 | | *x* = 1.0 | |
|---|---|---|---|---|---|---|---|---|
| | *n* | *k* | *n* | *k* | *n* | *k* | *n* | *k* |
| 1720 | 2.71 | 0.00 | 2.72 | 0.00 | 2.69 | 0.01 | 2.71 | 0.01 |
| 1730 | 2.71 | 0.00 | 2.72 | 0.00 | 2.69 | 0.01 | 2.71 | 0.01 |
| 1740 | 2.71 | 0.00 | 2.72 | 0.00 | 2.69 | 0.01 | 2.71 | 0.01 |
| 1750 | 2.71 | 0.00 | 2.72 | 0.00 | 2.69 | 0.01 | 2.71 | 0.01 |
| 1760 | 2.71 | 0.00 | 2.72 | 0.00 | 2.69 | 0.01 | 2.71 | 0.01 |
| 1770 | 2.71 | 0.00 | 2.72 | 0.00 | 2.69 | 0.01 | 2.71 | 0.01 |
| 1780 | 2.71 | 0.01 | 2.72 | 0.00 | 2.69 | 0.01 | 2.71 | 0.01 |
| 1790 | 2.71 | 0.01 | 2.72 | 0.01 | 2.69 | 0.01 | 2.71 | 0.01 |
| 1800 | 2.71 | 0.01 | 2.72 | 0.01 | 2.69 | 0.01 | 2.71 | 0.01 |
| 1810 | 2.71 | 0.01 | 2.72 | 0.01 | 2.69 | 0.01 | 2.71 | 0.01 |
| 1820 | 2.71 | 0.01 | 2.72 | 0.01 | 2.69 | 0.01 | 2.71 | 0.01 |
| 1830 | 2.71 | 0.01 | 2.72 | 0.01 | 2.68 | 0.01 | 2.71 | 0.01 |
| 1840 | 2.70 | 0.01 | 2.72 | 0.01 | 2.68 | 0.01 | 2.71 | 0.01 |
| 1850 | 2.70 | 0.01 | 2.72 | 0.01 | 2.68 | 0.01 | 2.71 | 0.01 |
| 1860 | 2.70 | 0.01 | 2.71 | 0.01 | 2.68 | 0.01 | 2.70 | 0.01 |
| 1870 | 2.70 | 0.01 | 2.71 | 0.01 | 2.68 | 0.01 | 2.70 | 0.01 |
| 1880 | 2.70 | 0.01 | 2.71 | 0.01 | 2.68 | 0.01 | 2.70 | 0.01 |
| 1890 | 2.70 | 0.01 | 2.71 | 0.01 | 2.68 | 0.01 | 2.70 | 0.01 |
| 1900 | 2.70 | 0.01 | 2.71 | 0.01 | 2.68 | 0.01 | 2.70 | 0.01 |
| 1910 | 2.70 | 0.01 | 2.71 | 0.01 | 2.68 | 0.01 | 2.70 | 0.01 |
| 1920 | 2.70 | 0.01 | 2.71 | 0.01 | 2.68 | 0.01 | 2.70 | 0.01 |
| 1930 | 2.70 | 0.01 | 2.71 | 0.01 | 2.68 | 0.01 | 2.70 | 0.01 |
| 1940 | 2.70 | 0.01 | 2.71 | 0.01 | 2.68 | 0.01 | 2.70 | 0.02 |
| 1950 | 2.70 | 0.01 | 2.71 | 0.01 | 2.68 | 0.01 | 2.70 | 0.02 |
| 1960 | 2.69 | 0.01 | 2.71 | 0.01 | 2.68 | 0.01 | 2.70 | 0.02 |
| 1970 | 2.69 | 0.01 | 2.71 | 0.01 | 2.68 | 0.01 | 2.71 | 0.02 |
| 1980 | 2.69 | 0.01 | 2.71 | 0.01 | 2.67 | 0.01 | 2.71 | 0.02 |

Table B.3: Optical constants of CdS, ZnO, AZO, Mo shown in Fig.3.12.

| λ / nm | CdS | | ZnO | | AZO | | λ / nm | Mo | |
|---|---|---|---|---|---|---|---|---|---|
| | *n* | *k* | *n* | *k* | *n* | *k* | | *n* | *k* |
| 350 | 2.31 | 0.47 | 2.09 | 0.37 | 2.27 | 0.10 | 350 | 2.26 | 2.78 |
| 360 | 2.31 | 0.46 | 2.18 | 0.30 | 2.21 | 0.07 | 355 | 2.26 | 2.78 |
| 370 | 2.33 | 0.44 | 2.26 | 0.22 | 2.16 | 0.04 | 360 | 2.27 | 2.78 |
| 380 | 2.34 | 0.43 | 2.30 | 0.15 | 2.11 | 0.02 | 365 | 2.29 | 2.79 |
| 390 | 2.36 | 0.42 | 2.30 | 0.09 | 2.08 | 0.01 | 370 | 2.29 | 2.79 |
| 400 | 2.37 | 0.40 | 2.26 | 0.05 | 2.06 | 0.01 | 375 | 2.30 | 2.79 |
| 410 | 2.37 | 0.39 | 2.21 | 0.03 | 2.05 | 0.01 | 380 | 2.30 | 2.80 |
| 420 | 2.38 | 0.38 | 2.16 | 0.01 | 2.04 | 0.01 | 386 | 2.32 | 2.80 |
| 430 | 2.38 | 0.37 | 2.13 | 0.00 | 2.04 | 0.01 | 391 | 2.32 | 2.82 |
| 440 | 2.38 | 0.36 | 2.11 | 0.00 | 2.03 | 0.01 | 396 | 2.32 | 2.83 |
| 450 | 2.38 | 0.35 | 2.09 | 0.00 | 2.02 | 0.01 | 401 | 2.33 | 2.85 |
| 460 | 2.37 | 0.33 | 2.08 | 0.01 | 2.01 | 0.00 | 406 | 2.33 | 2.86 |
| 470 | 2.37 | 0.31 | 2.06 | 0.01 | 2.00 | 0.00 | 412 | 2.34 | 2.89 |
| 480 | 2.37 | 0.28 | 2.04 | 0.01 | 1.99 | 0.00 | 417 | 2.35 | 2.90 |
| 490 | 2.38 | 0.24 | 2.03 | 0.01 | 1.98 | 0.00 | 422 | 2.36 | 2.92 |
| 500 | 2.38 | 0.20 | 2.01 | 0.00 | 1.97 | 0.00 | 427 | 2.37 | 2.94 |
| 510 | 2.37 | 0.15 | 2.00 | 0.00 | 1.96 | 0.00 | 432 | 2.38 | 2.97 |
| 520 | 2.37 | 0.10 | 1.99 | 0.00 | 1.94 | 0.00 | 437 | 2.38 | 2.98 |
| 530 | 2.37 | 0.06 | 1.99 | 0.00 | 1.93 | 0.00 | 442 | 2.40 | 3.01 |
| 540 | 2.36 | 0.03 | 1.99 | 0.00 | 1.92 | 0.00 | 443 | 2.41 | 3.02 |
| 550 | 2.36 | 0.01 | 1.98 | 0.00 | 1.91 | 0.00 | 448 | 2.42 | 3.03 |
| 560 | 2.35 | 0.00 | 1.98 | 0.00 | 1.90 | 0.00 | 453 | 2.44 | 3.06 |
| 570 | 2.35 | 0.00 | 1.98 | 0.00 | 1.89 | 0.00 | 458 | 2.46 | 3.08 |
| 580 | 2.34 | 0.01 | 1.97 | 0.00 | 1.89 | 0.00 | 463 | 2.47 | 3.10 |
| 590 | 2.34 | 0.01 | 1.97 | 0.00 | 1.88 | 0.00 | 468 | 2.50 | 3.13 |
| 600 | 2.33 | 0.01 | 1.97 | 0.00 | 1.87 | 0.00 | 473 | 2.51 | 3.15 |
| 610 | 2.33 | 0.00 | 1.97 | 0.00 | 1.87 | 0.00 | 474 | 2.52 | 3.15 |
| 620 | 2.32 | 0.00 | 1.97 | 0.00 | 1.86 | 0.00 | 479 | 2.54 | 3.18 |
| 630 | 2.32 | 0.00 | 1.96 | 0.00 | 1.86 | 0.00 | 484 | 2.56 | 3.19 |
| 640 | 2.32 | 0.00 | 1.96 | 0.00 | 1.86 | 0.00 | 489 | 2.58 | 3.21 |
| 650 | 2.31 | 0.00 | 1.95 | 0.00 | 1.86 | 0.00 | 494 | 2.61 | 3.22 |
| 660 | 2.31 | 0.00 | 1.95 | 0.00 | 1.86 | 0.00 | 499 | 2.64 | 3.24 |
| 670 | 2.31 | 0.00 | 1.95 | 0.00 | 1.85 | 0.00 | 504 | 2.67 | 3.25 |
| 680 | 2.31 | 0.00 | 1.94 | 0.00 | 1.85 | 0.00 | 505 | 2.68 | 3.26 |
| 690 | 2.31 | 0.00 | 1.94 | 0.00 | 1.84 | 0.00 | 510 | 2.70 | 3.27 |
| 700 | 2.31 | 0.00 | 1.94 | 0.00 | 1.84 | 0.00 | 515 | 2.73 | 3.28 |
| 710 | 2.31 | 0.00 | 1.94 | 0.00 | 1.84 | 0.00 | 520 | 2.76 | 3.28 |
| 720 | 2.31 | 0.00 | 1.94 | 0.00 | 1.83 | 0.00 | 525 | 2.79 | 3.29 |
| 730 | 2.31 | 0.00 | 1.94 | 0.00 | 1.83 | 0.00 | 530 | 2.82 | 3.29 |
| 740 | 2.31 | 0.00 | 1.94 | 0.00 | 1.82 | 0.00 | 536 | 2.85 | 3.28 |
| 750 | 2.30 | 0.00 | 1.94 | 0.00 | 1.82 | 0.00 | 541 | 2.88 | 3.27 |
| 760 | 2.30 | 0.00 | 1.94 | 0.00 | 1.81 | 0.00 | 546 | 2.89 | 3.27 |
| 770 | 2.30 | 0.00 | 1.94 | 0.00 | 1.81 | 0.01 | 551 | 2.90 | 3.26 |
| 780 | 2.30 | 0.00 | 1.94 | 0.00 | 1.80 | 0.01 | 556 | 2.92 | 3.25 |
| 790 | 2.29 | 0.00 | 1.93 | 0.00 | 1.79 | 0.01 | 561 | 2.93 | 3.25 |
| 800 | 2.29 | 0.00 | 1.93 | 0.00 | 1.78 | 0.01 | 566 | 2.94 | 3.25 |
| 810 | 2.28 | 0.00 | 1.93 | 0.00 | 1.78 | 0.01 | 572 | 2.94 | 3.24 |
| 820 | 2.28 | 0.00 | 1.93 | 0.00 | 1.77 | 0.01 | 577 | 2.95 | 3.24 |
| 830 | 2.27 | 0.00 | 1.94 | 0.00 | 1.76 | 0.01 | 582 | 2.95 | 3.24 |
| 840 | 2.26 | 0.00 | 1.94 | 0.00 | 1.75 | 0.01 | 587 | 2.95 | 3.24 |
| 850 | 2.25 | 0.00 | 1.95 | 0.00 | 1.74 | 0.01 | 592 | 2.95 | 3.24 |
| 860 | 2.24 | 0.00 | 1.95 | 0.00 | 1.73 | 0.01 | 597 | 2.96 | 3.26 |
| 870 | 2.24 | 0.00 | 1.95 | 0.00 | 1.72 | 0.01 | 598 | 2.95 | 3.25 |
| 880 | 2.23 | 0.00 | 1.95 | 0.00 | 1.72 | 0.01 | 603 | 2.97 | 3.26 |
| 890 | 2.23 | 0.00 | 1.95 | 0.00 | 1.71 | 0.01 | 608 | 2.97 | 3.27 |
| 900 | 2.22 | 0.00 | 1.94 | 0.00 | 1.71 | 0.01 | 613 | 2.97 | 3.28 |
| 910 | 2.22 | 0.00 | 1.94 | 0.00 | 1.70 | 0.01 | 618 | 2.98 | 3.28 |
| 920 | 2.22 | 0.00 | 1.94 | 0.00 | 1.69 | 0.01 | 623 | 2.98 | 3.29 |
| 930 | 2.21 | 0.00 | 1.94 | 0.00 | 1.69 | 0.01 | 629 | 3.00 | 3.30 |
| 940 | 2.21 | 0.00 | 1.94 | 0.00 | 1.68 | 0.01 | 634 | 3.00 | 3.30 |
| 950 | 2.20 | 0.00 | 1.94 | 0.00 | 1.67 | 0.01 | 639 | 3.01 | 3.31 |
| 960 | 2.20 | 0.00 | 1.94 | 0.00 | 1.66 | 0.02 | 644 | 3.01 | 3.32 |
| 970 | 2.20 | 0.00 | 1.94 | 0.00 | 1.65 | 0.02 | 649 | 3.02 | 3.32 |
| 980 | 2.19 | 0.01 | 1.94 | 0.00 | 1.64 | 0.02 | 654 | 3.03 | 3.33 |
| 990 | 2.19 | 0.01 | 1.94 | 0.00 | 1.63 | 0.02 | 659 | 3.04 | 3.34 |

Appendix B: Optical constants of layers in the CIGSe solar cells

| λ / nm | CdS | | ZnO | | AZO | | λ / nm | Mo | |
|---|---|---|---|---|---|---|---|---|---|
| | *n* | *k* | *n* | *k* | *n* | *k* | | *n* | *k* |
| 1000 | 2.19 | 0.01 | 1.94 | 0.00 | 1.62 | 0.02 | 665 | 3.05 | 3.34 |
| 1010 | 2.19 | 0.00 | 1.94 | 0.00 | 1.61 | 0.02 | 670 | 3.06 | 3.35 |
| 1020 | 2.19 | 0.00 | 1.94 | 0.00 | 1.60 | 0.02 | 675 | 3.06 | 3.36 |
| 1030 | 2.19 | 0.01 | 1.94 | 0.00 | 1.59 | 0.02 | 680 | 3.07 | 3.36 |
| 1040 | 2.19 | 0.01 | 1.93 | 0.00 | 1.59 | 0.02 | 685 | 3.08 | 3.36 |
| 1050 | 2.18 | 0.01 | 1.93 | 0.00 | 1.59 | 0.02 | 690 | 3.09 | 3.36 |
| 1060 | 2.18 | 0.01 | 1.93 | 0.00 | 1.58 | 0.02 | 691 | 3.09 | 3.36 |
| 1070 | 2.18 | 0.01 | 1.93 | 0.00 | 1.58 | 0.03 | 696 | 3.09 | 3.37 |
| 1080 | 2.18 | 0.01 | 1.93 | 0.00 | 1.58 | 0.03 | 701 | 3.10 | 3.37 |
| 1090 | 2.18 | 0.00 | 1.93 | 0.00 | 1.57 | 0.03 | 706 | 3.11 | 3.37 |
| 1100 | 2.18 | 0.00 | 1.93 | 0.00 | 1.57 | 0.03 | 711 | 3.11 | 3.36 |
| 1110 | 2.18 | 0.00 | 1.93 | 0.00 | 1.56 | 0.03 | 716 | 3.11 | 3.36 |
| 1120 | 2.17 | 0.00 | 1.93 | 0.00 | 1.56 | 0.04 | 721 | 3.11 | 3.37 |
| 1140 | 2.17 | 0.01 | 1.93 | 0.00 | 1.54 | 0.04 | 727 | 3.12 | 3.37 |
| 1150 | 2.17 | 0.01 | 1.93 | 0.00 | 1.54 | 0.04 | 732 | 3.12 | 3.37 |
| 1160 | 2.17 | 0.01 | 1.93 | 0.00 | 1.53 | 0.04 | 737 | 3.13 | 3.37 |
| 1170 | 2.16 | 0.01 | 1.93 | 0.00 | 1.53 | 0.04 | 742 | 3.12 | 3.36 |
| 1180 | 2.16 | 0.01 | 1.93 | 0.00 | 1.52 | 0.05 | 747 | 3.12 | 3.36 |
| 1190 | 2.16 | 0.01 | 1.93 | 0.00 | 1.51 | 0.05 | 752 | 3.13 | 3.35 |
| 1200 | 2.16 | 0.01 | 1.93 | 0.00 | 1.50 | 0.05 | 753 | 3.13 | 3.36 |
| 1210 | 2.16 | 0.01 | 1.93 | 0.00 | 1.50 | 0.05 | 758 | 3.12 | 3.35 |
| 1220 | 2.16 | 0.01 | 1.93 | 0.00 | 1.49 | 0.06 | 763 | 3.12 | 3.36 |
| 1230 | 2.16 | 0.01 | 1.93 | 0.00 | 1.48 | 0.06 | 768 | 3.12 | 3.35 |
| 1240 | 2.16 | 0.01 | 1.93 | 0.00 | 1.47 | 0.06 | 773 | 3.12 | 3.35 |
| 1250 | 2.16 | 0.01 | 1.93 | 0.00 | 1.47 | 0.06 | 778 | 3.11 | 3.36 |
| 1260 | 2.16 | 0.01 | 1.93 | 0.00 | 1.46 | 0.07 | 783 | 3.10 | 3.35 |
| 1270 | 2.16 | 0.01 | 1.92 | 0.00 | 1.45 | 0.07 | 784 | 3.10 | 3.35 |
| 1280 | 2.16 | 0.01 | 1.92 | 0.00 | 1.44 | 0.07 | 789 | 3.10 | 3.35 |
| 1290 | 2.17 | 0.01 | 1.93 | 0.00 | 1.43 | 0.08 | 794 | 3.09 | 3.35 |
| 1300 | 2.17 | 0.00 | 1.93 | 0.00 | 1.43 | 0.08 | 799 | 3.08 | 3.34 |
| 1310 | 2.17 | 0.00 | 1.93 | 0.00 | 1.42 | 0.08 | 804 | 3.08 | 3.35 |
| 1320 | 2.17 | 0.00 | 1.93 | 0.00 | 1.41 | 0.09 | 809 | 3.06 | 3.34 |
| 1330 | 2.17 | 0.00 | 1.93 | 0.00 | 1.40 | 0.09 | 814 | 3.06 | 3.35 |
| 1340 | 2.17 | 0.00 | 1.93 | 0.00 | 1.39 | 0.09 | 820 | 3.05 | 3.35 |
| 1350 | 2.17 | 0.00 | 1.93 | 0.00 | 1.39 | 0.10 | 825 | 3.03 | 3.35 |
| 1360 | 2.17 | 0.00 | 1.92 | 0.00 | 1.38 | 0.10 | 830 | 3.02 | 3.35 |
| 1370 | 2.16 | 0.00 | 1.92 | 0.00 | 1.38 | 0.11 | 835 | 3.01 | 3.35 |
| 1380 | 2.16 | 0.00 | 1.92 | 0.00 | 1.37 | 0.11 | 840 | 3.00 | 3.35 |
| 1390 | 2.17 | 0.00 | 1.92 | 0.00 | 1.36 | 0.11 | 845 | 2.98 | 3.35 |
| 1400 | 2.17 | 0.00 | 1.92 | 0.00 | 1.34 | 0.12 | 846 | 2.98 | 3.36 |
| 1410 | 2.17 | 0.00 | 1.92 | 0.00 | 1.33 | 0.12 | 851 | 2.97 | 3.35 |
| 1420 | 2.17 | 0.00 | 1.92 | 0.00 | 1.32 | 0.13 | 856 | 2.95 | 3.36 |
| 1430 | 2.17 | 0.00 | 1.92 | 0.00 | 1.31 | 0.13 | 861 | 2.93 | 3.37 |
| 1440 | 2.17 | 0.00 | 1.92 | 0.00 | 1.30 | 0.14 | 866 | 2.92 | 3.37 |
| 1450 | 2.17 | 0.00 | 1.92 | 0.00 | 1.29 | 0.14 | 871 | 2.90 | 3.38 |
| 1460 | 2.17 | 0.00 | 1.92 | 0.00 | 1.28 | 0.15 | 876 | 2.88 | 3.39 |
| 1470 | 2.17 | 0.00 | 1.92 | 0.00 | 1.27 | 0.15 | 882 | 2.85 | 3.40 |
| 1480 | 2.17 | 0.00 | 1.92 | 0.00 | 1.26 | 0.15 | 887 | 2.84 | 3.41 |
| 1490 | 2.17 | 0.00 | 1.92 | 0.00 | 1.24 | 0.16 | 892 | 2.83 | 3.41 |
| 1500 | 2.17 | 0.00 | 1.92 | 0.00 | 1.23 | 0.16 | 897 | 2.81 | 3.43 |
| 1510 | 2.17 | 0.00 | 1.92 | 0.00 | 1.21 | 0.17 | 902 | 2.79 | 3.43 |
| 1520 | 2.17 | 0.00 | 1.92 | 0.00 | 1.20 | 0.18 | 907 | 2.77 | 3.45 |
| 1530 | 2.17 | 0.00 | 1.92 | 0.00 | 1.19 | 0.19 | 908 | 2.77 | 3.45 |
| 1540 | 2.17 | 0.00 | 1.92 | 0.00 | 1.17 | 0.20 | 913 | 2.74 | 3.47 |
| 1550 | 2.17 | 0.00 | 1.92 | 0.00 | 1.15 | 0.21 | 918 | 2.73 | 3.48 |
| 1560 | 2.17 | 0.00 | 1.92 | 0.00 | 1.14 | 0.21 | 923 | 2.71 | 3.49 |
| 1570 | 2.17 | 0.00 | 1.92 | 0.00 | 1.12 | 0.22 | 928 | 2.69 | 3.51 |
| 1580 | 2.17 | 0.00 | 1.92 | 0.00 | 1.11 | 0.23 | 933 | 2.67 | 3.52 |
| 1590 | 2.17 | 0.00 | 1.92 | 0.00 | 1.09 | 0.23 | 938 | 2.65 | 3.54 |
| 1600 | 2.17 | 0.00 | 1.92 | 0.00 | 1.09 | 0.24 | 944 | 2.63 | 3.57 |
| 1610 | 2.17 | 0.00 | 1.92 | 0.00 | 1.08 | 0.25 | 949 | 2.61 | 3.58 |
| 1620 | 2.17 | 0.00 | 1.92 | 0.00 | 1.07 | 0.26 | 954 | 2.60 | 3.60 |
| 1630 | 2.17 | 0.00 | 1.92 | 0.00 | 1.06 | 0.27 | 959 | 2.58 | 3.62 |
| 1640 | 2.17 | 0.00 | 1.92 | 0.00 | 1.05 | 0.28 | 964 | 2.56 | 3.63 |
| 1650 | 2.17 | 0.00 | 1.92 | 0.00 | 1.04 | 0.29 | 969 | 2.55 | 3.66 |
| 1660 | 2.17 | 0.00 | 1.92 | 0.00 | 1.03 | 0.30 | 975 | 2.52 | 3.69 |
| 1670 | 2.17 | 0.00 | 1.92 | 0.00 | 1.02 | 0.31 | 980 | 2.50 | 3.70 |
| 1680 | 2.17 | 0.00 | 1.92 | 0.00 | 1.01 | 0.32 | 985 | 2.49 | 3.72 |

| λ / nm | CdS | | ZnO | | AZO | | λ / nm | Mo | |
|---|---|---|---|---|---|---|---|---|---|
| | *n* | *k* | *n* | *k* | *n* | *k* | | *n* | *k* |
| 1690 | 2.17 | 0.00 | 1.91 | 0.00 | 1.00 | 0.33 | 990 | 2.47 | 3.75 |
| 1700 | 2.17 | 0.00 | 1.91 | 0.00 | 0.99 | 0.34 | 995 | 2.46 | 3.77 |
| 1710 | 2.17 | 0.00 | 1.91 | 0.00 | 0.98 | 0.35 | 1000 | 2.44 | 3.79 |
| 1720 | 2.17 | 0.00 | 1.91 | 0.00 | 0.97 | 0.36 | 1006 | 2.43 | 3.82 |
| 1730 | 2.17 | 0.00 | 1.91 | 0.00 | 0.96 | 0.37 | 1011 | 2.41 | 3.85 |
| 1740 | 2.17 | 0.00 | 1.91 | 0.00 | 0.95 | 0.38 | 1016 | 2.39 | 3.87 |
| 1750 | 2.17 | 0.00 | 1.91 | 0.00 | 0.94 | 0.39 | 1021 | 2.37 | 3.89 |
| 1760 | 2.17 | 0.00 | 1.91 | 0.00 | 0.93 | 0.40 | 1026 | 2.36 | 3.92 |
| 1770 | 2.17 | 0.00 | 1.91 | 0.00 | 0.91 | 0.42 | 1031 | 2.35 | 3.94 |
| 1780 | 2.17 | 0.00 | 1.91 | 0.00 | 0.90 | 0.43 | 1037 | 2.33 | 3.98 |
| 1790 | 2.17 | 0.00 | 1.91 | 0.00 | 0.90 | 0.44 | 1042 | 2.32 | 4.01 |
| 1800 | 2.17 | 0.00 | 1.91 | 0.00 | 0.89 | 0.45 | 1047 | 2.31 | 4.03 |
| 1810 | 2.17 | 0.00 | 1.91 | 0.00 | 0.88 | 0.47 | 1052 | 2.30 | 4.05 |
| 1820 | 2.17 | 0.00 | 1.90 | 0.00 | 0.87 | 0.48 | 1057 | 2.29 | 4.08 |
| 1830 | 2.17 | 0.00 | 1.90 | 0.00 | 0.87 | 0.49 | 1062 | 2.27 | 4.11 |
| 1840 | 2.17 | 0.00 | 1.90 | 0.00 | 0.86 | 0.51 | 1063 | 2.27 | 4.11 |
| 1850 | 2.17 | 0.00 | 1.90 | 0.00 | 0.85 | 0.52 | 1068 | 2.26 | 4.14 |
| 1860 | 2.17 | 0.00 | 1.90 | 0.00 | 0.84 | 0.54 | 1073 | 2.25 | 4.17 |
| 1870 | 2.17 | 0.00 | 1.90 | 0.00 | 0.83 | 0.55 | 1078 | 2.23 | 4.19 |
| 1880 | 2.17 | 0.00 | 1.90 | 0.00 | 0.82 | 0.57 | 1083 | 2.23 | 4.22 |
| 1890 | 2.17 | 0.00 | 1.90 | 0.00 | 0.81 | 0.58 | 1088 | 2.21 | 4.25 |
| 1900 | 2.16 | 0.00 | 1.90 | 0.00 | 0.80 | 0.60 | 1093 | 2.20 | 4.26 |
| 1910 | 2.16 | 0.00 | 1.90 | 0.00 | 0.79 | 0.61 | 1094 | 2.21 | 4.28 |
| 1920 | 2.16 | 0.00 | 1.90 | 0.00 | 0.79 | 0.63 | 1099 | 2.19 | 4.30 |
| 1930 | 2.16 | 0.00 | 1.90 | 0.00 | 0.78 | 0.64 | 1104 | 2.19 | 4.33 |
| 1940 | 2.16 | 0.00 | 1.90 | 0.00 | 0.78 | 0.66 | 1109 | 2.18 | 4.37 |
| 1950 | 2.16 | 0.00 | 1.90 | 0.00 | 0.78 | 0.67 | 1114 | 2.17 | 4.39 |
| 1960 | 2.16 | 0.00 | 1.90 | 0.00 | 0.77 | 0.69 | 1119 | 2.16 | 4.42 |
| 1970 | 2.16 | 0.00 | 1.90 | 0.00 | 0.77 | 0.71 | 1124 | 2.15 | 4.44 |
| 1980 | 2.16 | 0.00 | 1.90 | 0.00 | 0.76 | 0.72 | 1125 | 2.15 | 4.45 |
| | | | | | | | 1130 | 2.14 | 4.48 |
| | | | | | | | 1135 | 2.13 | 4.50 |
| | | | | | | | 1140 | 2.12 | 4.53 |
| | | | | | | | 1145 | 2.13 | 4.55 |
| | | | | | | | 1150 | 2.12 | 4.59 |
| | | | | | | | 1155 | 2.12 | 4.62 |
| | | | | | | | 1161 | 2.12 | 4.65 |
| | | | | | | | 1166 | 2.13 | 4.68 |
| | | | | | | | 1171 | 2.14 | 4.68 |
| | | | | | | | 1176 | 2.15 | 4.71 |
| | | | | | | | 1181 | 2.12 | 4.74 |
| | | | | | | | 1186 | 2.01 | 4.73 |
| | | | | | | | 1187 | 2.02 | 4.78 |
| | | | | | | | 1192 | 1.79 | 4.78 |
| | | | | | | | 1197 | 1.90 | 4.82 |

# List of publications

*Published:*

- **G. Yin**, C. Merschjann, M. Schmid "The effect of surface roughness on the determination of optical constants of $CuInSe_2$ and $CuGaSe_2$ thin films" *Journal of Applied Physics* **113**, 213510 2013 (related to chapter 3)
- **G. Yin**, P. Manley, M. Schmid "Influence of substrate and its temperature on the optical constants of $CuIn_{1-x}Ga_xSe_2$ thin films" *Journal of Physics D: Applied Physics* **47**, 135101 2014 (related to chapter 3)
- **G. Yin**, V. Brackmann, V. Hoffmann, M. Schmid "Enhanced performance of ultra-thin $Cu(In,Ga)Se_2$ solar cells deposited at low process temperature" Solar Energy Materials & Solar Cells **132,** 142–147 2015 (related to chapter 2)
- P. Manley, **G. Yin**, M. Schmid "A method for calculating the complex refractive index of inhomogeneous thin films" *Journal of Physics D: Applied Physics* **47**, 205301 2014
- Y. Augarten, W. Sprenger, B. Pieters, R. Varache, O. Bakaeva, G. Janssen, **Y. Guanchao**, F. Friedrich, M. Schmid, M. Celino, J. Hüpkes "Modeling Infrastructure Along the Value Chain: from Materials to System Performance" *Proceedings of the 28th European Photovoltaic Solar Energy Conference*, Paris 2013
- A.Ott, S.Ring, **G. Yin**, W. Calvet, B. Stannowski, Y. Lu, R. Schlatmann M Ballauff "Efficient plasmonic scattering of colloidal silver particles through annealing-induced changes" *Nanotechnology* **25**, 455706 2014

*Submitted:*

- **G. Yin**, P. Manley, M. Schmid, "Light absorption enhancement for ultra-thin CuIn1-xGaxSe2 (CIGSe) solar cells using 2-D SiO2 nanosphere array" *submitted* 2014 (related to chapter 6)
- M.-C. van Lare, **G. Yin**, A. Polman, M. Schmid, "Light coupling and trapping in ultra-thin $Cu(In,Ga)Se_2$ solar cells using dielectric scattering patterns" *submitted* (2014), **co-first author** (related to chapter 7)

# Curriculum Vitae

**Name:** Guanchao Yin
**Sex:** Male
**Date of Birth:** 25th November 1985
**Place of birth:** Hubei, P.R.China
**Nationality:** Chinese

**EDUCATION:**

**2011.08—— present** Ph.D student, Helmholtz Berlin Centre for Materials and Energy

**2008.09——2011.06** Master of Material Physics and Chemistry, Wuhan University of Technology, China

**2004.09——2008.06** Bachelor of Material Chemistry, Wuhan University of Technology, China

# Declaration

Ich erkläre an Eides Statt, dass die vorliegende Dissertation in allen Teilen von mir selbständig angefertigt wurde und die benutzten Hilfsmittel vollständig angegeben worden sind.

# Acknowledgments

Finally, I would cordially like to express my gratitude to the people helping me through all the difficulties during my Ph.D period.

First and foremost, I would sincerely thank my supervisor in HZB Prof. Martina Schmid for guiding me to the Ph.D topic. Without her patience, strictness, encourage and great dedications, I couldn't image I can go through my Ph.D work. Also, specially thank Prof. Walter Reimers for accepting me as his student in TU Berlin and his suggestions on my thesis.

I would like to thank Reiner Klenk for his support on the experiment instruments and his deep explanations to the electrical properties of CIGSe solar cells.

I would like to thank Christoph Merschjann and Phillip Manley for the help in the simulation programs.

I would like to thank Manuela Goebelt and Michael Latzel for the deposition of $Al_2O_3$ films, Patrick Andrä for preparing the Ag nanoparticles and Alexander Steigert for XPS measurements.

I would like to thank Andreas Ott, Fangfang Chu, Yan Lu for preparing nanoparticles and closely-packed $SiO_2$ nanosphere arrays.

I would like to thank Claire van Lare and Prof. Albert Polman for the cooperation of $SiO_2$ nanostructures at the interface of CIGSe/Mo.

I would like to thank Indu Dhiman and Yael Augarten for reading the whole thesis.

I would like to thank Carola Kelch and Michael Kirsch for the CdS, ZnO, AZO, grids and ITO deposition, Christian Kauffman, Joachim Klaer and Bianka Bunn for the preparation of the Mo substrates, Jürgen Albert and Jörg Beckmann for the technical help.

Again, I would like to thank all colleagues and others who helped me during Ph.D work but the names are not mentioned above.

Special thanks to my family for the spiritual support on my life in Germany and my newly born niece for bringing me so much fun.

Finally, I would like to thank China Scholarship Council and Helmholtz-Association for Young Investigator groups within the Initiative and Networking fund (VH-NG-928) for the financial support during my Ph.D studies.

# References


[1] P. Jackson, D. Hariskos, E. Lotter, S. Paetel, R. Wuerz, R. Menner, W. Wischmann, and M. Powalla, "New world record efficiency for Cu(In,Ga)$Se_2$ thin-film solar cells beyond 20 %," *Prog. Photovolt: Res. Appl.,* 19(2011) 894–897

[2] "New best mark in thin-film solar performance with 21.7 percent efficiency," *http://www.zsw-bw.de/en/support/press-releases/press-detail/zsw-brings-world-record-back-to-stuttgart.html.*

[3] Table of "Best researh-cell efficiencies," *http://www.nrel.gov/ncpv/images/efficiency_chart.jpg.*

[4] B. A. Andersson, C. Azar, J. Holmberg, and S. Karlsson, "Material constants for thin-film solar cells," *Energy*, 23(1998) 407–411.

[5] C. S. Tao, J. Jiang, and M. Tao, "Natural resource limitations to terawatt-scale solar cells," *Sol. Energy Mater. Sol. Cells*, 95(2011) 3176–3180.

[6] V. Fthenakis, "Sustainability of photovoltaics: The case for thin-Film solar cells," Renew. Sust. Energy Rev., 13(2009) 2746-2750.

[7] N. Naghavi, Z. Jehl, F. Donsanti, J. F. Guillemoles, I. Gérard, M. Bouttemy, A. Etcheberry, J. L. Pelouard, S. Collin, C. Colin, N. Péré-Laperne, N. Dahan, J. J. Greffet, B. Morel, Z. Djebbour, A. Darga, D. Mencaraglia, G. Voorwinden, B. Dimmler, M. Powalla, and D. Lincot, "Toward high efficiency ultra-thin CIGSe based solar cells using light management techniques," *Proc. of SPIE*, 8256(2012) 825617.

[8] O. Lundberg, M. Bodegärd, J. Malmström, and L. Stolt, "Influence of the Cu(In,Ga)$Se_2$ thickness and Ga grading on solar cell performance," *Prog. Photovoltaics Res. Appl.*, 11(2003) 77–88.

[9] Z. Jehl, F. Erfurth, N. Naghavi, L. Lombez, I. Gerard, M. Bouttemy, P. Tran-Van, A. Etcheberry, G. Voorwinden, B. Dimmler, W. Wischmann, M. Powalla, J. F. Guillemoles, and D. Lincot, "Thinning of CIGS solar cells: Part II: Cell characterizations," *Thin Solid Films*, 519(2011) 7212–7215.

[10] M. Gloeckler and J. R. Sites, "Potential of submicrometer thickness Cu(In,Ga)Se2 solar cells," *J. Appl. Phys.*, 98(2005) 103703.

[11] J. K. Larsen, H. Simchi, P. Xin, K. Kim, and W. N. Shafarman, "Backwall superstrate configuration for ultrathin Cu(In,Ga)$Se_2$ solar cells," *App. Phys. Lett.* 104(2014) 033901.

[12] J. Krč, F. Smole, and M. Topič, "Potential of light trapping in microcrystalline silicon solar cells with textured substrates," *Prog. Photovoltaics Res. Appl.*, 11(2003) 429–436.

[13] M. Zeman, R. A. C. M. M. Swaaij, J. W. Metselaar, and R. E. I. Schropp, "Optical modeling of a-Si:H solar cells with rough interfaces: Effect of back contact and interface roughness," *J. Appl. Phys.*, 88(2000) 6436.

[14] B. Lipovšek, J. Krč, O. Isabella, M. Zeman, and M. Topič, "Analysis of thin-film silicon solar cells with white paint back reflectors," *Phys. Status Solidi*, 1044(2010) 1041– 1044.

[15] R. Kaplan, "Effects of the back reflector on the optical enhancement factor and quantum efficiency of a-Si : H p-i-n solar cells," *Turk J. Phys.*, 26(2002) 363–368.

[16] H. Tan, L. Sivec, B. Yan, R. Santbergen, M. Zeman, and A. H. M. Smets, "Improved light trapping in microcrystalline silicon solar cells by plasmonic back reflector with broad angular scattering and low parasitic absorption," *Appl. Phys. Lett.*, 102(2013) 153902.

[17] K. R. Catchpole and A. Polman, "Plasmonic solar cells," *Opt. Express,* 16(2008) 21793–21800.

[18] V. E. Ferry, M. A. Verschuuren, H. B. T. Li, E. Verhagen, R. J. Walters, R. E. I. Schropp, H. A. Atwater, and A. Polman, "Light trapping in ultrathin plasmonic solar cells," *Opt. Express,*18(2010) 237–245.

[19] H. A. Atwater and A. Polman, "Plasmonics for improved photovoltaic devices," *Nat. Mater.*, 9(2010) 205–213.

[20] A. Chutinan, N. P. Kherani, and S. Zukotynski, "High-efficiency photonic crystal solar cell architecture," *Opt. Express,*17(2009) 4494–4500.

[21] A. Polman and H. Atwater, "Photonic design principles for ultrahigh-efficiency photovoltaics.," *Nat. Mater.*, 11(2012) 174–177.

[22] M. Peters, M. Rüdiger, H. Hauser, M. Hermle, and B. Bläsi, "Diffractive gratings for crystalline silicon solar cells - optimum parameters and loss mechanisms," *Prog. Photovolt: Res. Appl.,* 20(2012) 862–873.

[23] E. Wang, S. Mokkapati, T. P. White, T. Soderstrom, S. Varlamov, and K. R. Catchpole, "Light trapping with titanium dioxide diffraction gratings fabricated by nanoimprinting," *Prog. Photovolt: Res. Appl.*, 22(2014) 587–592.

[24] C. Colin, I. Massiot, A. Cattoni, N. Vandamme, C. Dupuis, N. Bardou, I. Gerard, N. Naghavi, J. F. Guillemoles, J. L. Pelouard, and S. Collin, "Broadband light-trapping in ultra-thin nano-structured solar cells," *Proc. of SPIE*, 8620(2013) 86200C.

[25] W. Wang, S. Wu, R. J. Knize, K. Reinhardt, Y. Lu, and S. Chen, "Enhanced photon absorption and carrier generation in nanowire solar cells.," *Opt. Express*, 20(2012) 3733–3743.

[26] J. L. Gray, "*The Physics of the Solar Cell*," Chapter 3, John Wiley & Sons, Ltd (2003), Second Edition.

[27] W. Peter, "Physics of solar cells," Wiley-VCH Verlag GmbH, (2005).

[28] D. Rudmann, "Effects of sodium on growth and properties of Cu(In,Ga)$Se_2$ thin films and solar cells," Dissertation, Swiss Federal Institute of Technology, 2004

[29] K. Orgassa, "Coherent optical analysis of the ZnO/CdS/CdS/Cu(In,Ga)$Se_2$ thin film solar cell," Dissertation, University of Stuttgart, 2004.

[30] D. L. Young, J. Abushama, R. Noufi, X. Li, J. Keane, T. A. Gessert, J. S. Ward, M. Contreras, and T. J. Coutts, "A new Thin-film $CuGaSe_2$/Cu(In,Ga)$Se_2$ Bifacial, tandem solar cell with both junctions formed simultaneously preprint," *29th IEEE PV Specialists Conference*, 2002.

[31] S. H. Wei, S. B. Zhang, and A. Zunger, "Effects of Ga addition to $CuInSe_2$ on its electronic, structural, and defect properties," *Appl. Phys. Lett.*, 72(1998) 3199.

[32] D. Kuo, Y. Tu and M. Monsefi, "Effects of selenization parameters on growth characteristics of the Cu(In,Ga)$Se_2$ films deposited by sputtering with a Cu-In-Ga, Cu-In-$Ga_2Se_3$, or Cu-Ga-$In_2Se_3$ target and a subsequent selenization procedure at 550-700°C," *Appl. Surf. Sci.*, 268(2013) 22-27.

[33] H. Rodriguez-Alvarez, R. Mainz, B. Marsen, D. Abou-Ras, and H. W. Schock, "Recrystallization of Cu–In–S thin films studied in situ by energy-dispersive X-ray diffraction," *J. Appl. Crystallogr.*, 43(2010) 1053–1061.

[34] A. M. Gabor, J. R. Tuttle, D. S. Albin, M. A. Contreras, R. Noufi, and A. M. Hermann, "High-efficiency $CuIn_xGa_{1-x}Se_2$ solar cells made from $(In_x,Ga_{1-x})_2Se_3$ precursor films," *Appl. Phys. Lett.*, 65(1994) 198.

[35] R. Caballero, S. Siebentritt, K. Sakurai, C. A. Kaufmann, H. W. Schock, and M. C. Lux-Steiner, "Effect of Cu excess on three-stage $CuGaSe_2$ thin films using in-situ process controls," *Thin Solid Films*, 515(2007) 5862–5866.

[36] W. Witte, S. Spiering, and D. Hariskos, "Substitution of the CdS buffer layer in CIGS thin-film solar cells," *www.vip-journal.de,* 26(2014) 23–27.

[37] R. Caballero, C. Fischer, C. A. Kaufmann, I. Lauermann, R. Mainz, H. Mönig, A. Schöpke, C. Stephan, C. Streeck, S. Schorr, A. Eicke, M. Döbeli, B. Gade, J. Hinrichs, T. Nunney, H. Dijkstra, V. Hoffmann, D. Klemm, V. Efimova, and A. Bergmaier, "Microscopy Microanalysis Comprehensive Comparison of Various Techniques for the Analysis of Elemental Distributions in Thin Films," *Microscopy and Microanalysis*, 2011 1-24.

[38] C. A. Kaufmann, R. Caballero, T. Unold, R. Hesse, R. Klenk, S. Schorr, M. Nichterwitz, and H. W. Schock, "Depth profiling of Cu(In,Ga)$Se_2$ thin films grown at low temperatures," *Sol. Energy Mater. Sol. Cells*, 93(2009) 859–863.

[39] A. Chirilă, S. Buecheler, F. Pianezzi, P. Bloesch, C. Gretener, A. R. Uhl, C. Fella, L. Kranz, J. Perrenoud, S. Seyrling, R. Verma, S. Nishiwaki, Y. E. Romanyuk, G. Bilger, and A. N. Tiwari, "Highly efficient Cu(In,Ga)$Se_2$ solar cells grown on flexible polymer films.," *Nat. Mater.*, 10(2011) 857–61.

[40] S. S. Hegedus and W. N. Shafarman, "Thin-film solar cells: device measurements and analysis," *Prog. Photovoltaics Res. Appl.*, 12(2004) 155–176.

[41] A. Niemegeers, M. Burgelman, R. Herberholz, U. Rau, and D. Hariskos, "Model for electronic in Cu(In,Ga)$Se_2$ solar cells," *Prog. Photovoltaics Res. Appl.*, 6(1998) 407–421.

[42] S. Theodoropoulou, D. Papadimitriou, K. Anestou, C. Cobet, and N. Esser, "Optical properties of $CuIn_{1-x}Ga_xSe_2$ quaternary alloys for solar-energy conversion," *Semicond. Sci. Technol.*, 24(2009) 015014.

[43] T. Fritz and K. Leo, "Determination of optical constants of thin absorbing films from normal incidence reflectance and transmittance measurements," *Opt. Communications*, 166(1999) 35–42.

[44] M. I. Alonso, M. Garriga, C. A. D. Rinc, and E. Hern, "Optical functions of chalcopyrite $CuGa_xIn_{1-x}Se_2$ alloys," *Appl. Phys. A,* 74(2002) 659–664.

[45] M. I. Alonso, K. Wakita, J. Pascual, M. Garriga, and N. Yamamoto, "Optical functions and electronic structure of $CuInSe_2$, $CuGaSe_2$, $CuInS_2$, and $CuGaS_2$," *Phys. Rev. B*, 63(2001) 075203.

[46] L. Zhang, Q. He, W. L. Jiang, F. F. Liu, C. J. Li, and Y. Sun, "Effects of substrate temperature on the structural and electrical properties of Cu(In,Ga)$Se_2$ thin films," *Sol. Energy Mater. Sol. Cells*, 93(2009) 114–118.

[47] O. S. Heavens, "Optical properties of thin solid films," Butterworths, 1955.

[48] M. Schmid, "Optik der $CuGaSe_2$-Solarzelle für hoche ziente Tandemkonzepte," Dissertation, Free University of Berlin, 2009.

[49] B. Harbecke, "Coherent and incoherent reflection and transmission of multilayer structures," *Appl. Phys. B,* 39(1986) 165-170.

[50] E. Centurioni, "Generalized matrix method for calculation of internal light energy flux in mixed coherent and incoherent multilayers," *Appl. Opti.,* 44(2005) 7532-7539.

[51] C. L. Mitsas and D. I. Siapkas, "Generalized matrix method for analysis of coherent and incoherent reflectance and surfaces, interfaces, and finite substrates," *Appl. Opti.,* 34(1995) 1678–1683.

[52] C. C. Katsidis and D. I. Siapkas, “General transfer-matrix method for optical multilayer systems with coherent, partially coherent, and incoherent interference,” *Appl. Opti.,* 41(2002) 3978–3987.

[53] M. C. Troparevsky, A. S. Sabau, and A. R. Lupini, “Transfer-matrix formalism for the calculation of optical response in multilayer systems : from coherent to incoherent interference,” *Opt. Express*, 18(2010) 24715–24721.

[54] R. E. Denton, R. D. Campbell, S. G. Tomlin," The determination of theoptical constants of thin films from measurements of reflectance and transmittance at normal incidence "*J. Phys. D: Appl. Phys*., 5(1972) 852-863.

[55] "RefDex" *http://www.helmholtzberlin.de/forschung/oe/ee/nanooptix/refdex/index_en.html.*

[56] P. Nilsson, “Determination of optical constants from intensity measurements at normal incidence,” *Appl. Opti.,* 7(1968) 435–442.

[57] J. Szczyrbowski, “Determination of optical constants of real thin films,” *J. Phys. D: Appl. Phys.*, 11(1978) 583-593.

[58] I. Filinski, “The effects of sample imperfections on optical spectra,” *Phys. Stat. Sol. (b)* 49(1972), 577-588.

[59] H. E. Bennett, J. O. Porteus, “Relation Between Surface Roughness and Specular Reflectance," *Journal of the optical of society of America,* 51(1961) 123-129.

[60] M. Bouttemy, P. Tran-Van, I. Gerard, T. Hildebrandt, A. Causier, J. L. Pelouard, G. Dagher, Z. Jehl, N. Naghavi, G. Voorwinden, B. Dimmler, M. Powalla, J. F. Guillemoles, D. Lincot, and A. Etcheberry, “Thinning of CIGS solar cells: Part I: Chemical processing in acidic bromine solutions,” *Thin Solid Films*, 519(2011) 7207–7211.

[61] T. Nakada, Y. Hirabayashi, T. Tokado, D. Ohmori, and T. Mise, “Novel device structure for Cu(In,Ga)$Se_2$ thin film solar cells using transparent conducting oxide back and front contacts,” *Sol. Energy*, 77(2004) 739–747.

[62] R. Klenk, “Characterisation and modelling of chalcopyrite solar cells,” *Thin Solid Films*, 387(2001) 135–140.

[63] F. Erfurth, Z. Jehl, M. Bouttemy, N. Dahan, P. Tran-Van, I. Gerard, A. Etcheberry, J. J. Greffet, M. Powalla, G. Voorwinden, D. Lincot, J. F. Guillemoles, and N. Naghavi, “Mo/Cu(In,Ga)$Se_2$ back interface chemical and optical properties for ultrathin CIGSe solar cells,” *Appl. Surf. Sci.*, 258(2012) 3058–3061.

[64] P. Spinelli, M. A. Verschuuren, and A. Polman, “Broadband omnidirectional antireflection coating based on subwavelength surface Mie resonators.,” *Nat. Commun.*, 3(2012) 692.

[65] H. Tan, R. Santbergen, A. H. M. Smets, and M. Zeman, "Plasmonic light trapping in thin- film silicon solar cells with improved self-assembled silver nanoparticles," *Nano Lett.*, 12 (2012) 4070–4076.

[66] J. Grandidier, "Simulations of solar cell absorption enhancement using resonant modes of a nanosphere array," *J. Photonics Energy*, 2(2012), 024502.

[67] A. Heifetz, S. C. Kong, A. V. Sahakian, A. Taflove, and V. Backman, "Photonic Nanojets.," *J. Comput. Theor. Nanosci.*, 9(2009) 1979–1992.

[68] N. Dahan, Z. Jehl, T. Hildebrandt, J. J. Greffet, J. F. Guillemoles, D. Lincot, and N. Naghavi, "Optical approaches to improve the photocurrent generation in Cu(In,Ga)$Se_2$ solar cells with absorber thicknesses down to 0.5 μm," *J. Appl. Phys.*, 112(2012) 094902.

[69] H. Tan, E. Psomadaki, O. Isabella, M. Fischer, P. Babal, R. Vasudevan, M. Zeman, and A. H. M. Smets, "Micro-textures for efficient light trapping and improved electrical performance in thin-film nanocrystalline silicon solar cells," *Appl. Phys. Lett.*, 173905(2013) 1–5.

[70] M. Schmid, J. Krč, R. Klenk, M. Topič, and M. C. Lux-Steiner, "Optical modeling of chalcopyrite-based tandems considering realistic layer properties," *Appl. Phys. Lett.*, 94(2009) 053507.

[71] O. Berger, D. Inns, and A. G. Aberle, "Commercial white paint as back surface reflector for thin-film solar cells," *Sol. Energy Mater. Sol. Cells*, 91(2007) 1215–1221.

[72] R. Santbergen, J. Blanker, A. Dhathathreyan, H. Tan, A. H. M. Smets, and M. Zeman, "Towards lambertian internal light scattering in solar cells using coupled plasmonic and dielectric nanoparticles as back reflector." *Photovoltaic Specialists Conference (PVSC) IEEE 39th*, 2013

[73] Z. J. Li-kao, N. Naghavi, F. Erfurth, J. F. Guillemoles, I. Gérard, A. Etcheberry, J. L. Pelouard, S. Collin, G. Voorwinden, and D. Lincot, "Towards ultrathin copper indium gallium diselenide solar cells : proof of concept study by chemical etching and gold back contact engineering," *Prog. Photovolt: Res. Appl.* 20(2012) 582–587.

[74] R. Santbergen, T. L. Temple, R. Liang, A. H. M. Smets, R. C. M. M. Swaaij, and M. Zeman, "Application of plasmonic silver island films in thin-film silicon solar cells," *J. Opt.*, 14(2012) 024010.

[75] A. Polman, "Plasmonics Applied," *Science,* 322(2008) 868–869.

[76] Z. Yu, A. Raman, and S. Fan, "Fundamental limit of nanophotonic light trapping in solar cells.," *Proc. Natl. Acad. Sci. U.S. A.*, 107(2010) 17491.

[77] M. Schmid, R. Klenk, M. C. Lux-steiner, and M. Topiˇ, "Modeling plasmonic scattering combined with thin-film optics," *Nanotechnology* , 22 (2011) 025204.

[78] J. Mertz, "Radiative absorption, fluorescence, and scattering of a classical dipole near a lossless interface: a unifieddescription," *J. Opt. Soc. Am. B,* 17(2000) 1906–13.

[79] P. Spinelli and A. Polman, "Prospects of near-field plasmonic absorption enhancement in semiconductor materials using embedded Ag nanoparticles," *Opt. Express,* 20(2012) 205–213.

[80] C. F. Bohren, D. R. Huffman "Absorption and scattering of light by small particles," John Wiley and Sons, 1983.

[81] K. R. Catchpole and A. Polman, "Design principles for particle plasmon enhanced solar cells," *Appl. Phys. Lett.*, 93(2008) 191113.

[82] N. P. Hylton, X. F. Li, V. Giannini, K. H. Lee, N. J. Ekins-Daukes, J. Loo, D. Vercruysse, P. Van Dorpe, H. Sodabanlu, M. Sugiyama, and S. a Maier, "Loss mitigation in plasmonic solar cells: aluminium nanoparticles for broadband photocurrent enhancements in GaAs photodiodes.," *Sci. Rep.*, 3(2013) 2874.

[83] M. J. Beliatis, S. J. Henley, S. Han, K. Gandhi, D. T. Adikaari, E. Stratakis, E. Kymakis, and S. R. P. Silva, "Organic solar cells with plasmonic layers formed by laser nanofabrication.," *Phys. Chem. Chem. Phys.*, 15(2013) 8237–8244.

[84] S. W. Baek, J. Noh, C. H. Lee, B. Kim, M. K. Seo, and J. Y. Lee, "Plasmonic forward scattering effect in organic solar cells: A powerful optical engineering method," *Sci. Rep.*, 3(2013) 1726.

[85] U. Kreibig and M. Vollmer, "Optical Properties of Metal Clusters," Springer, 1995

[86] C. Burrows, "Plasmonic resonances of metallic nanoparticles in arrays and in isolation," Dissertation, University of Exeter, 2010.

[87] Http://www.jcmwave.com/.

[88] M. van Lare, F. Lenzmann, M. A. Verschuuren, and A. Polman, "Mode coupling by plasmonic surface scatterers in thin-film silicon solar cells," *Appl. Phys. Lett.*, 101(2012) 221110.

[89] M. Schmid, P. Andrae, and P. Manley, "Plasmonic and photonic scattering and near fields of nanoparticles.," *Nanoscale Res. Lett.*, 9(2014), 50.

[90] M. L. Brongersma, Y. Cui, and S. Fan, "Light management for photovoltaics using high-index nanostructures.," *Nat. Mater.*, 13(2014) 451–60.

[91] M. R. Ljubljana, "Whispering gallery modes," presentation, 2011.

[92] D. M. Callahan and H. A. Atwater, "Configuration Optimization of a nanosphere array on top of a thin film solar cell 1.," *IEEE*, 2011 3325–3327.

[93] J. Grandidier, D. M. Callahan, J. N. Munday, and H. Atwater, “Light absorption enhancement in thin-film solar cells using whispering gallery modes in dielectric nanospheres.,” *Adv. Mater.*, 23(2011) 1272–1276.

[94] Y. Yao, J. Yao, V. K. Narasimhan, Z. Ruan, C. Xie, S. Fan, and Y. Cui, “Broadband light management using low-Q whispering gallery modes in spherical nanoshells.,” *Nat. Commun.*, 3(2012) 664.

[95] G. Moon, T. Lee, B. Kim, G. Chae, J. Kim, S. Kim, J. M. Myoung, and U. Jeong, “Assembled monolayers of hydrophilic particles on water surfaces.,” *ACS Nano*, 5(2011) 8600–8612.

[96] S. A. Mann, R. R. Grote, R. M. Osgood, and J. Schuller, “Dielectric particle and void resonators for thin film solar cell textures.,” *Opt. Express*, 19(2011) 25729.

[97] M. A. Verschuuren, "Substrate conformal imprint lithography for nanophotonics," Dissertaion, University of Utrecht, 2010.

[98] Personal communication with Claire van Lare.

[99] B. Vermang, V. Fjällström, J. Pettersson, P. Salomé, and M. Edoff, “Development of rear surface passivated Cu(In,Ga)$Se_2$ thin film solar cells with nano-sized local rear point contacts,” *Sol. Energy Mater. Sol. Cells*, 117(2013) 505–511.

[100] *http://en.wikipedia.org/wiki/Finite-difference_time-domain_method*

[101] C. van Lare, "Light trapping in thin-film solar cells using dielectric and metallic nanostructures," Dissertaion, University of Amsterdam, 2014.

[102] *http://en.wikipedia.org/wiki/Finite_element_method*